The Role of Mtss1 in Cortical Development

Dissertation

zur

Erlangung des Doktorgrades (Dr. rer. nat.)

der Mathematisch-Naturwissenschaftlichen Fakultät der

Rheinischen Friedrich-Wilhelms-Universität Bonn

vorgelegt von

Clemens Wagner

aus Duisburg

Bonn, 2025

Angefertigt mit Genehmigung der Mathematisch-Naturwissenschaftlichen Fakultät der

Rheinischen Friedrich-Wilhelms-Universität Bonn

Gutachter/Betreuer:	Prof. Dr Karl Schilling
Gutachter:	PD Dr. Gregor Kirfel
Tag der Promotion:	12.01.2026
Erscheinungsjahr:	2026

Abstract

The role of the membrane-shaping and actin-scaffolding protein Mtss1 in the central nervous system (CNS) is being unravelled more and more. Previous publications investigating malformations that arise under deficiency of Mtss1 put great emphasis on the cerebellum and hippocampus. However, a salient consequence of Mtss1 knock-out (KO), namely reduced thickness of the cerebral cortex, has to my knowledge gone unexplained so far. As a novel feature of the Mtss1-KO phenotype, I report alterations to the pools of neural progenitor cells, which give rise to the cerebral cortex: Numbers of Tbr2-expressing neurogenic intermediate progenitor cells are increased in the brains of mice in late embryonic and perinatal development. At the same time, expression of glial markers and genes associated with apoptosis are reduced, and in the neurogenic germinal zones, more cells are in a proliferative state. Furthermore, expression of Egfr, which is a player in neuro- and gliogenesis, and is known to be controlled by Mtss1 in other contexts, is also affected. In adult Mtss1 KO mice, reduced cortical thickness goes along with reduced cell numbers and increased expression of glial marker Gfap, which both are features of Egfr deficiency. Taken together, these findings seem to suggest an Egfr-related disruption of neocortical development as a result of Mtss1 deficiency.

Acknowledgements

I am indebted to Dr. Britta Eiberger, Prof. Dr. Karl Schilling, PD Dr. Gregor Kirfel and Prof. Dr. Tim Clarner for the opportunity to conduct this project, their patient support, and many fruitful discussions. I also wish to extend my gratitude to the further members of my examination committee, PD Dr. Gerhild van Echten-Deckert and Prof. Dr. Nicolas Gompel. Andrea Christ has my deep appreciation for counsel, technical assistance, and all the things that go unnoticed by PhD students. The current and former staff of the Anatomical Institute have my gratitude for making me feel welcome and always lending a hand. I would especially like to acknowledge Fabienne Lülsberg, Sabine Molly-Klumbies, Carina Winkler, Barbara Kalthoff, Iboika Haias, Stefanie Ramrath, Prof. Dr. Stephan Baader, Heike Mukilakoy, Manuela Bolz, Narziss Haias, Daniela Krauß, Dr. Rittika Chunder, Birgit Blanck, Marion Michels, Tobias Lindenberg, Öznur Yilmaz, Dr. Nina Ishorst, Dr. Uğur Bora, Prof. Dr. Benjamin Odermatt and Dr. Jessica Lambertz. The members of IBI-2 Mechanobiologie around Prof. Dr. Rudolf Merkel I would like to thank for fruitful and fun cooperation. I am also indebted to many wonderful persons in my life outside working hours. I would especially like to mention Leonie Scherges, Dominik Gosal, Michael Schmidtke, Gudrun, Ralf and Carla Wagner, Mirta Ferrone, Emil Kvist, Hannah Metzger, Jens Evers and Jonna Warnecke.

Table of Contents

1 List of Abbreviations....5
2 Introduction....6
2.1 Cellular Development of the Telencephalon....6
2.1.1 Neural Progenitor Cells in Development....8
2.1.2 Glial Progenitor Cells in Development....11
2.1.3 The Ventricular System and the Adult VZ-SVZ....13
2.1.4 Defects of Neural Development....15
2.2 Membrane and Cytoskeleton Dynamics....15
2.2.1 Planar Cell Polarity....18
2.2.2 Neural Cell Migration....19
2.3 Mtss1....20
2.3.1 Mtss1 Expression Pattern and Related Diseases....21
2.3.2 Mtss1 in the CNS....22
2.3.3 Domains and Molecular Functions....23
2.4 Purpose of the Project....28
3 Materials and Methods....29
3.1 List of Materials....29
3.2 Animal Husbandry....33
3.3 Genotyping of Experimental Animals....34
3.4 RT-qPCR....36
3.4.1 RNA Isolation and Generation of cDNA....36
3.4.2 RT-qPCR....38
3.5 Histological Methods....39
3.5.1 Sample Preparation....39
3.5.2 Immunofluorescence of Ventricle Wholemounts....41
3.5.3 Immunofluorescence of Paraffin Sections....43
3.5.4 Nissl Staining of Cryosections....44
3.5.5 Immunostaining of Cryosections and Mtss1 Promoter Activity....44
3.6 Image Acquisition and Evaluation....46
3.6.1 Determining Number of B1 Cells in Ependyma....46
3.6.2 Determining Rotational Polarity of Motile Cilia....46
3.6.3 Determining Translational Polarity of Ependymal Cells....47
3.6.4 Determining Tbr2 and Pax6 Expression Profile....48
3.6.5 Evaluating Composition of Ventricular Zone and Subventricular Zone of Newborn Mice....49
3.7 Determining the Composition of the Caudal Telencephalon....50
3.7.1 Mechanical Properties of Caudal Telencephalon and Distance from Ependyma to Meninges....50
3.7.2 Cell Number and DNA Content of Caudal Telencephalon....51
3.8 Data Evaluation....52

4 Results....54
4.1 Distance from Ependyma to Meninges and Cell Numbers are Reduced in Caudal Telencephalon of Mtss1 Deficient Mice....54
4.1.1 Distance from Ependyma to Meninges and Mechanical Properties....54
4.1.2 Cell Numbers and DNA Content....56
4.2 The Gene Expression in Posterior Telencephalon of Mtss1 KO Mice is Altered....57
4.2.1 Developmental Course of mRNA Expression in Posterior Telencephalon....57
4.2.2 Expression of mRNAs Specific for Neural Progenitor Cells and Glia in Perinatal Mice. 62
4.2.3 Expression of mRNAs Marking Proliferation- and Apoptosis in Perinatal Mice....64
4.2.4 mRNA-Expression in P7 Mice....67
4.2.5 Expression of mRNAs Specific for Neural Progenitor Cells, Neurons and Glia in Adult Mice 68
4.2.6 Expression of mRNAs Marking Apoptosis and Proliferation in Adult Mice....70
4.2.7 Egfr Expression....71
4.3 Altered Cell Distribution in VZ and SVZ of Newborn Mtss1 KO Mice....72
4.3.1 Increased Numbers of Proliferating Cells in Ventricle Roof VZ/SVZ at P0....72
4.3.2 Increased Numbers and Widened Distribution of $Tbr2^+$ Cells as well as Shifted Distribution of $Sox2^+$ and $Pax6^+$ Cells in the VZ/SVZ of the Ventricular Roof of P0 Mtss1-deficient Mice 74
4.4 The Cell Type Composition of Ependyma is Altered in Mtss1 Deficient Mice....77
4.5 The Polarity of E1 Cells in Adult Mtss1 KO Mice is Marginally Altered....78
4.5.1 Rotational Polarity of E1 Cells in Adult Mice....78
4.5.2 Translational Polarity of Ependymal E1 Cells in in Adult Mice....81
5 Discussion....84
5.1 Interpretation....84
5.1.1 The Composition of the Telencephalon in Adult Mtss1 KO Mice is Altered....84
5.1.2 Proliferation and Apoptosis in the Brains of Perinatal Mtss1 KO Mice is Altered....87
5.1.3 Altered Cell Type Populations in the Posterior Telencephalon of P0 Mtss1 KO Mice…88
5.1.4 How Could Mtss1 Control Cortical Cell Numbers?....92
5.1.5 Egfr-Mtss1-Interaction Could Explain the Decreased Telencephalic Cell Count in Adult Mtss1 KO Mice....96
5.1.6 The Involvement of Mtss1 in The PCP Pathway is Unclear....99
5.2 Conclusion....102
6 References....103
7 List of Figures....114
8 List of Tables....116
9 Appendix....117
9.1 Example Indentation Graph....117
9.2 Example Set of Angular Data for Evaluation of Translational Polarity....118
9.3 R-Scripts....118

1 List of Abbreviations

aRG	apical Radial Glia
AUC	Area Under The Curve
BL/6	C57 Black/6
bp	Basepair(s)
bRG	basal Radial Glia
c-	Centi-
CNS	Central Nervous System
CSF	Cerebrospinal fluid
d	Day(s)
DAB	3,3′-Diaminobenzidine
DAPI	4′,6-Diamidino-2-Phenylindole
DEPC	Diethyl Pyrocarbonate
dk	Donkey
DLHP	Dorsolateral Hinge Point(S)
DNA	Deoxyribonucleic Acid
dNTP	Deoxyribonucleoside triphosphate
E	Embryonic Day (as in E1 - Embryonic Day 1)
EDTA	Ethylenediaminetetraacetic acid
Egfr	Epidermal Growth Factor Receptor
EGTA	Egtazic Acid
FCS	Foetal Calf Serum
g	Gram(s)
GABA	γ-Aminobutyric Acid
gt	Goat
h	Hour(s)
H_2O	Demineralised Water
I-BAR domain	Inverted Bin-Amphiphysin-Rvs Domain
IPC	Intermediate Progenitor Cell
k-	Kilo-
KO	Knock out
L	Litre(s)
lacZ	Component Z of Lactose Operon
m	Meter(s)
M	Mol/l
m-	Milli-
MHP	Midline Hinge Point(S)
MIM	Missing In Metastasis
min	Minute(s)
ms	Mouse
Mtss1	Metastasis-Suppressor 1
NEC	Neuroepithelial Cell
NES	Nuclear Export Sequence
NGS	Normal Goat Serum
NLS	Nuclear Localisation Sequence
P	Postnatal Days (as in P2 - Postnatal Day 2)
PBS	Phosphate-Buffered Saline
PCP	Planar Cell Polarity
PCR	Polymerase Chain Reaction
PFA	Paraformaldehyde
pH	Potentia Hydrogenii
$PI(4,5)P_2$	Phosphatidylinositol 4,5-Bisphosphate
rb	Rabbit
RGC	Radial Glia Cell
RNA	Ribonucleic Acid
RT	Room Temperature
RT-qPCR	Real Time Quantitative PCR
s	Second(s)
SD	Standard Deviation
SVZ	Subventricular Zone
TBS	Tris Buffered Saline
v/v	Volume/Volume
VZ	Ventricular zone
w	Week(s)
w/v	Weight/Volume
WT	Wild Type
xg	Times Gravity of Earth Equivalent
α-	Anti-
µ-	Micro-
$^+$	-positive (as in $Ki67^+$ = Ki67-positive)

2 Introduction

2.1 Cellular Development of the Telencephalon

The development of the brain is an interplay of several overlapping processes. These include proliferation of progenitor cells, differentiation of those cells into neurons and glia via intermediate cell types, cell migration and apoptosis (Kandel, Schwartz, Jessell, Siegelbaum, Hudspeth, 2013). Cues coming from both the apical (ventricular) and basal (meningeal) surface of the developing brain as well as each cell's surroundings are required for these processes to function (Penisson *et al,* 2019), (Budday *et al,* 2015), (Boucherie *et al,* 2018).

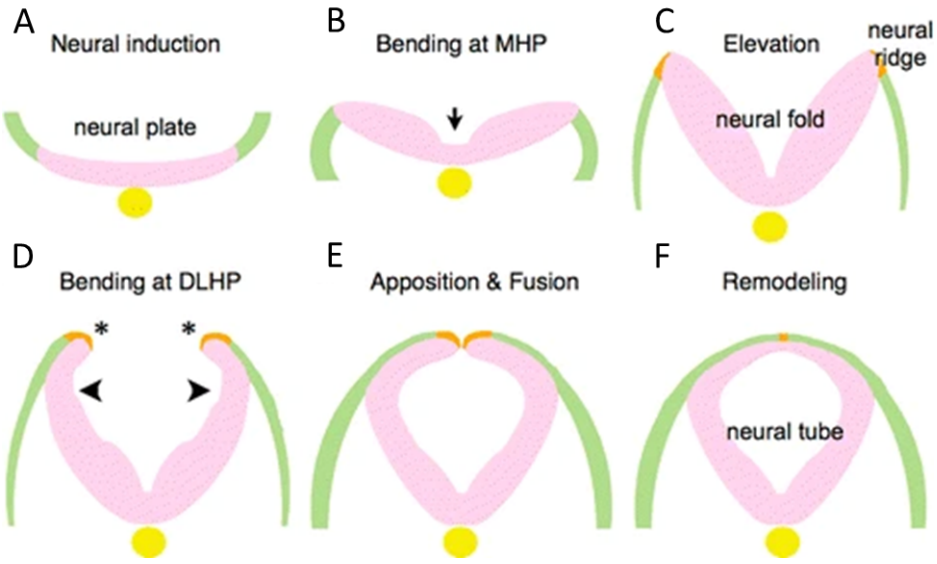

Figure 1: Cranial Neurulation

A: *The cranial portion of the neural tube forms by primary neurulation. In proximity of the dorsal cord (yellow), ectoderm differentiates into neuroectoderm (pink), forming the neural plate. More distant portions differentiate into surface ectoderm (green).* ***B-D****: At the medial hinge point (MHP), the neuroectoderm starts folding up into the neural fold.* ***E:*** *Dorsolateral hinge points (DLHP) meet dorsal of the nascent neural tube, initiating its closure.* ***F:*** *Finally, the neural tube is closed and covered by both neuroectoderm and surface ectoderm. Figure from Yamaguchi & Miura (2013) .*

The CNS arises from the neural plate, originally a region of ectoderm, which is induced to not commit to ectodermal, but neural fate. As a result of various mechanisms, including constriction of the apical actin cytoskeleton, convergent extension, shifting of neighbour cells, and apoptosis, the neural plate folds up to form the neural tube (van der Spuy *et al,* 2023). This process is called primary neurulation and is schematically depicted in Figure 1. The rostral part of the neural tube in turn bulges into three interconnected vesicles, which then further subdivide, as shown in Figure 2. The anteriormost of these five resulting vesicles forms the telencephalon, and ultimately the tissues this project is focused on: The neocortex and the ependyma of the lateral ventricles. The lumen of the neural tube forms the ventricular system (Kandel, Schwartz, Jessell, Siegelbaum, Hudspeth, 2013). While some variations do exist between different species of vertebrates, the mechanism described here hold true for both human and mouse (Nikolopoulou *et al,* 2017).

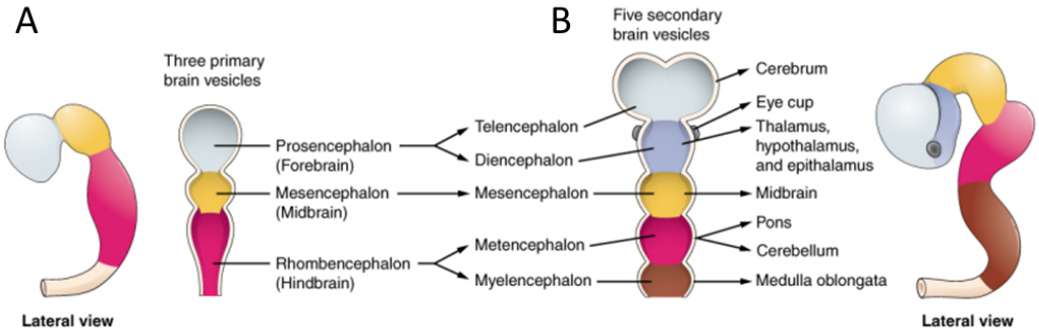

Figure 2: Brain Vesicles In Development

A: *The rostral neural tube bulges into three primary brain vesicles. At the same time, it folds up in ventral direction.* ***B:*** *The three primary vesicles subdivide into five secondary vesicles, which together form the brain and eyes. The caudal portions of the neural tube form the spinal cord. Figure modified, from Betts et al (2022).*

2.1.1 Neural Progenitor Cells in Development

At embryonic day 10.5 (E10.5) in mice (or gestational week 5-6 in humans), the neural tube consists of neuroepithelial cells (NEC), which express Nestin, Sox2 and Notch. These cells are capable of self-renewal, and both directly and via various types of progenitor cells give rise to almost all types of neurons and glia found in the CNS. Firstly, apical radial glia cells (RGC) are produced. These are marked by their processes spanning from the ventricular to the pial surface and expression of Sox2, Pax6, Nestin and Vimentin. Like NECs, they can divide to renew their own numbers, or give rise to other cells. This includes neurons and further progenitor cell types. One of these are basal RGCs, which continue their expression of Sox2 and Pax6, but change their position within the germinal zone (Penisson *et al,* 2019). A prominent population of transient amplifying cells are neurogenic intermediate progenitor cells (IPC), also known as “intermediate neuronal progenitors” or “basal progenitors”, which divide about 1-3 times before neuronal differentiation (Kowalczyk *et al,* 2009). Neurogenic IPCs downregulate their Sox2- and Pax6-expression in favour of Tbr2, prior to undergoing radial migration. This introduces different layers to the developing CNS: The ventricular zone (VZ), containing apical RGCs, and the SVZ, containing IPCs and basal RGCs. Both of these progenitor cell types can produce neurons as well. Before they can take up function as a mature neuron, the cells need to migrate out of the VZ and subventricular zone (SVZ) to specific target locations, and finish differentiation there (Penisson *et al,* 2019). While many modes of migration that employ different sets of proteins and processes exist, it is common to distinguish two modes in the developing neocortex: Radially (along the fibres of RGCs), and tangentially (orthogonally to RGC fibres). In mice, interneurons are chiefly born in the VZ and SVZ of the ganglionic eminences of the ventral telencephalon, and migrate

tangentially and radially, while projections neurons mostly originate in the VZ and SVZ of their respective region of cerebral cortex and mostly migrate radially (Molyneaux *et al,* 2007), (Stouffer *et al,* 2016), (Kandel, Schwartz, Jessell, Siegelbaum, Hudspeth, 2013). This happens in an “inside-out” fashion of growth, with the youngest neurons going past the older ones towards the meningeal surface of the developing cortex (Rakic, 2009), which leads to forming of additional layers. During development, the region containing cells that completed migration is called the cortical plate, the regions which contain cells still migrating is called intermediate zone. A final, outermost layer called marginal zone contains Cajal-Retzius-cells organising this process. The layers of the mature neocortex amount to six (Molyneaux *et al,* 2007), (Penisson *et al,* 2019). However, in addition, remains of the VZ and SVZ persist into adulthood as a germinal niche within and beneath the ependyma, as shall be discussed later (Ihrie & Alvarez-Buylla, 2011). Notably, Both RGCs and IPCs are able to divide symmetrically or asymmetrically. This is crucial to balancing production of the different cell types they can give rise to, and requires control of mitotic spindle orientation and spindle size symmetry (Pilaz et al, 2016), (Sun et al, 2005), (Penisson et al, 2019). A schematic representation of the differentiation process of neural progenitors to mature neurons and glia is displayed in Figure 3.

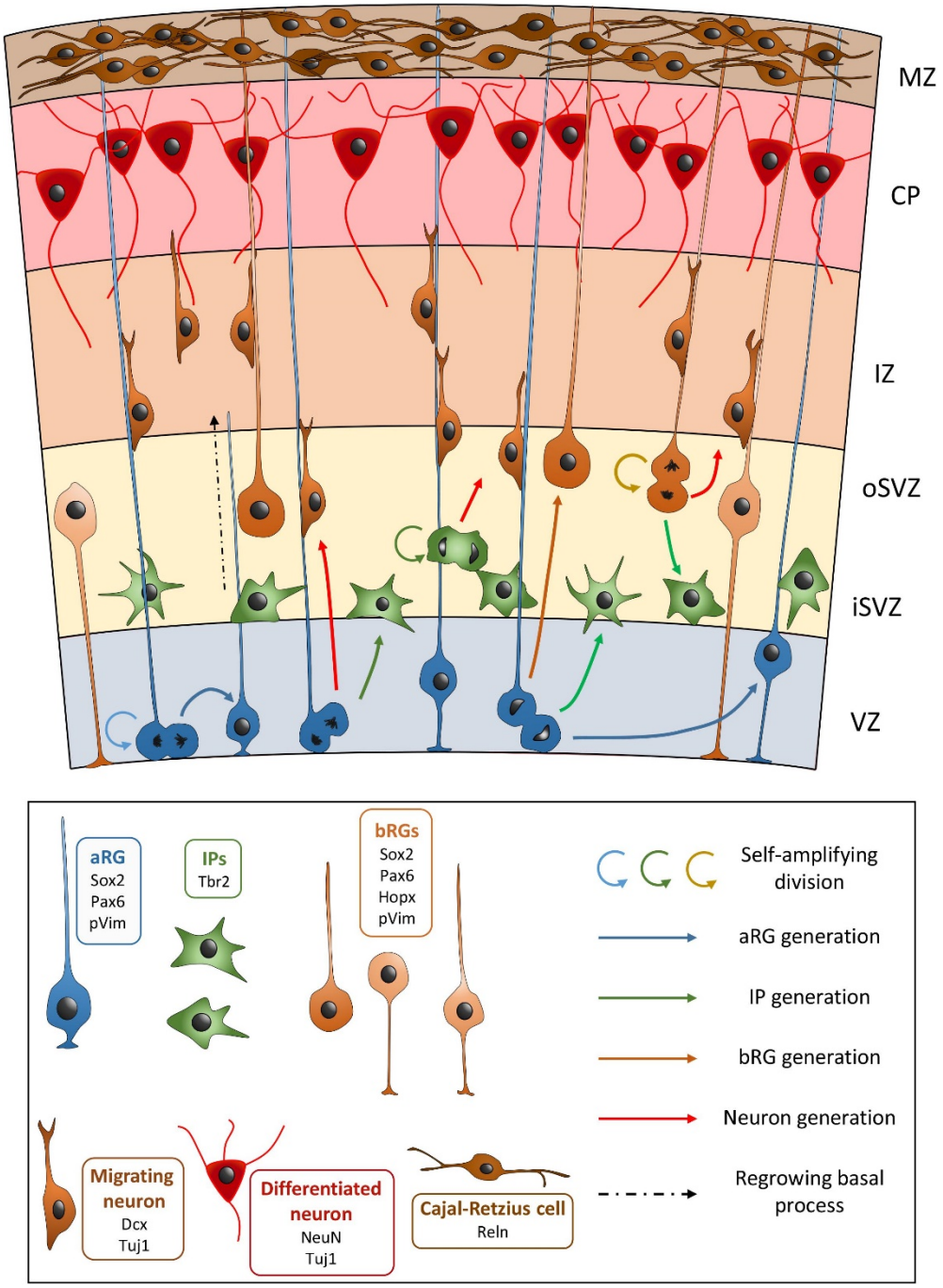

Figure 3: Differentiation of Neural Progenitors to Mature Neocortical Projection Neurons

Self-amplifying, Pax6^{+} apical radial glia (aRG) are able to differentiate into postmitotic neurons directly or via other kinds of self-amplifying neural progenitor cells: Intermediate progenitors (IPs or basal radial glia (bRG). Newborn postmitotic neurons migrate radially and differentiate into functional projection neurons at their point of destination, guided by surrounding factors such as radial glia or Cajal-Retzius cells. Figure modified, from Penisson et al (2019).

Finally, as a part of regular neural development, a great number of neurons (50% in some cell types) die by programmed cell death (Kandel, Schwartz, Jessell, Siegelbaum, Hudspeth, 2013). While mature neurons enjoy ample protection against apoptosis (Kole *et al,* 2013), this process has been shown to be heavily controlled by input from the individual neuron's targets and thus still takes place in relatively advanced stages of differentiation. For instance, excessive cell death of motor neurons and neurons of the anteroventral cochlear nucleus has been shown if their innervation targets are experimentally removed within the first, but not the third postnatal week in mice (Kandel, Schwartz, Jessell, Siegelbaum, Hudspeth, 2013). However, this is not the only developmental time point, at which apoptosis plays a crucial role in normal neural development. In chick embryos, it was discovered that death of select cells during neurulation exerts mechanical influence, bending the neural plate (van der Spuy *et al,* 2023). Later in development, a significant number of progenitor cells are lost without ever differentiating into mature neurons or glia, as has been found for $Tbr2^+$ IPCs (Hevner, 2019), (Vaid & Huttner, 2020).

2.1.2 Glial Progenitor Cells in Development

Generation of astrocytes and oligodendrocytes begins well into the neurogenic period, with the temporary overlap varying depending on species and brain region (Stepien *et al,* 2021). In the cerebral cortex of mice, astrocytes emerge after about E10, oligodendrocytes after E18 (Burns *et al,* 2009). Different models propose different time points, at which progenitor cells commit to glial fate. They all accept a common pool of progenitor cells to sequentially produce neurons, then astrocytes, and then oligodendrocytes. Some authors however additionally assume a portion of progenitor cells to be set aside early in development in order to later produce glia, but

no neurons (Burns *et al,* 2009), (Magavi *et al,* 2012), or only a subset of the previously neurogenic progenitor cells to switch to gliogenesis (Zhang *et al,* 2020). Regardless, macroglia ultimately arise from apical RGCs both directly and via their own types of intermediate precursor cells, somewhat like the neurons previously discussed (Burns *et al,* 2009). These transient multipotent intermediate progenitor cells are not marked by expression of Tbr2, but instead Olig2, Ascl1 and Egfr, and generate astrocytes, oligodendrocytes, and olfactory bulb interneurons (Liang *et al,* 2024). Especially Egfr seems to be an important, but not entirely indispensable factor in the switch to gliogenesis (Zhang *et al,* 2020). The first mature astrocytes appear around postnatal day 4 (P4), the first oligodendrocytes around P7 (Burns *et al,* 2009). As it is for neurons, migration is essential for the development of most glial cell in the CNS. Astrocyte precursors migrate radially and populate the cortex in an “inside-out”-pattern, much like projection neurons, but still proliferate within their target layer of cerebral cortex (Magavi *et al,* 2012), (Zhang *et al,* 2020). Notably, the previously mentioned transcription factor Sox2 continues to be expressed during this phase, unlike in neurogenesis, where a rapid decrease of Sox2-expression happens latest when the developing cell leaves the SVZ. In astrocytes, Sox2 is only downregulated when the cell enters a quiescent state, but can be upregulated, should the cell become proliferative again (Bani-Yaghoub *et al,* 2006). Pax6, another transcription factor relevant to RGCs, prevents the gliogenic switch (Liang *et al,* 2024). Oligodendrocyte precursors originate at various different points within the brain (Stouffer *et al,* 2016). Interestingly, recalling the route interneurons take, some oligodendrocytes stem from the medial ganglionic eminence and migrate along blood vessels to their point of destination (Tsai *et al,* 2016).

Lastly, forming much of the ependyma, postmitotic, multiciliated E1 cells and B1 adult neural stem cells are generated directly from apical RGCs (Ortiz-Álvarez *et al,* 2019), (Redmond *et al,* 2019). This process takes place between E12 and P4 (Spassky *et al,* 2005) (or 25th to 27th gestational week in humans (Budday *et al,* 2015)). By conversion from B1 cells, B2 cells arise, mostly during the first postnatal months. B2 cells are similar in their gene expression to B1 cells, but do not contact the ventricular surface (Cebrian-Silla *et al,* 2025). The ventricular surface increases by expansion of E1 cells, with their apical surface increasing up to 11-fold over the course of days in mice (Redmond *et al,* 2019). This allows further growth of the brain. As microglia are derived from cells residing in the yolk sac (Stouffer *et al,* 2016), and not from NECs (Penisson *et al,* 2019), they shall not be discussed here.

2.1.3 The Ventricular System and the Adult VZ-SVZ

In the adult mouse, the cerebral ventricles are lined with ependymal cells of different subtypes, the origins of which were mentioned in section 2.1.2, and filled with cerebrospinal fluid (CSF). The ependyma acts as a barrier between the CSF and the tissues of the CNS. However, it performs many functions beyond that. E1 cells propel CSF through the ventricular system using their numerous motile cilia (Redmond *et al,* 2019), (Spassky *et al,* 2005), while B1 cells contribute to the generation of olfactory bulb interneurons and oligodendrocytes in the adult (Ihrie & Alvarez-Buylla, 2011). Both cell types are arranged in a specific fashion: Only small apical processes of B1 cells contact the ventricular surface, with large-surfaced E1 cells forming a “pinwheel” around those processes, but covering most of the ventricular surface (Redmond *et al,* 2019), (Spassky *et al,* 2005). The importance of CSF transport by E1 cells is an actively researched topic, as failure of cilia (by reduced beat frequency, complete

absence, or altered polarity) is associated with hydrocephaly (Lee, 2013), (Boutin *et al,* 2014). Furthermore, CSF has been shown to be a transport medium not only for nutrients, but for neurotransmitters, hormones, growth factors and microRNAs, which contribute to various processes including adult neurogenesis, inflammation, and possibly the circadian rhythm and fear learning. The choroid plexus, producing the bulk of CSF volume in the adult, also releases many of these factors into the ventricular cavity. However, the ependyma of both the brain and spinal cord contribute to CSF production as well (Kaiser & Bryja, 2020), (Eichele *et al,* 2020). CSF can enter the blood via arachnoid villi granulations, and the brain parenchyma via the glymphatic system (Iliff *et al,* 2012), (Rasmussen *et al,* 2022). In addition, another type of ependymal cells called tanycytes (E3 and E2 cells), which possess long processes in order to contact blood vessels or neurons, facilitate exchange of substances with the CSF. Interestingly, tanycytes themselves have been shown to be another type of adult neural progenitor cell (Eichele *et al,* 2020).

In embryonic development, the ventricular system and CSF flow are established before the choroid plexus, differentiated ependyma and adult CSF egress routes such as glymphatic system and subarachnoid space are present. Nonetheless, its components are tightly controlled. Embryonic CSF composition not only differs from that of adult CSF, but is also subject to constant change, containing appropriate signal molecules at specific time points. It also holds proteins at higher concentrations overall than in the adult. Apart from molecular signals, CSF pressure exerts a mechanical influence on the developing brain, which is indispensable for its normal growth (Rasmussen *et al,* 2022).

2.1.4 Defects of Neural Development

Perhaps unsurprisingly, the complexity of neural development is prone to disturbance. A wide array of disorders can be traced to each of the mechanisms mentioned above: Altered proliferation or differentiation of neural progenitors could be linked to microcephaly, exencephaly, megalencephaly, ataxia, intellectual disability, depression and schizophrenia (Budday *et al,* 2015), (Arai & Taverna, 2017), (Duy *et al,* 2022). Defects in cell migration have been associated with lissencephaly, periventricular heterotopia, intellectual disability, autistic spectrum disorder and epilepsy (Kawauchi, 2015), (Stouffer *et al,* 2016), (Budday *et al,* 2015). Loss of neurons after completion of migration can lead to polymicrogyria (Budday *et al,* 2015). A disorder associated with the ventricular system is congenital hydrocephaly, with causes ranging from overproduction of CSF, dysfunction of motile cilia (Lee, 2013), or by premature differentiation of neural progenitor cells, in which case reduced stiffness of the cerebral wall precedes enlargement of the ventricles (Duy *et al,* 2022).

2.2 Membrane and Cytoskeleton Dynamics

Cell migration, proliferation, PCP and ciliogenesis all share their strong dependence on the cytoskeleton. The cytoskeleton is a complex apparatus that fulfils a wide array of often highly cell-type-specific functions. Fundamentally, it consists of several somewhat separate, but interacting networks of actin-, Tubulin-, septin- and various types of intermediate filaments. These are assembled from protein monomers, and can be dynamically shaped into different forms. Although spontaneous assembly from these monomers occurs, this requires precise control by other actors, both proteins and membrane lipids (Svitkina, 2018), (Merino *et al,* 2020), (Bezanilla *et al,*

2015). These may promote or inhibit filament nucleation from monomers, elongation of existing structures, disassembly, bundling, branching or linking of cytoskeletal components to other proteins, like adhesion molecules, which are fixed to the plasma membrane (Lee & Streuli, 2014), (Svitkina, 2018), (Merino *et al,* 2020). Such effects can be as nuanced as inducing one mechanisms for actin filament assembly while inhibiting another mechanism which also promotes actin polymerisation (Bezanilla *et al,* 2015). Some cytoskeleton-interacting proteins are motor proteins, which do not only link a protein to a filament, but actively move it along that filament to a specific direction or adaptor proteins, which serve to link two other proteins. The relationship between the different cytoskeletal networks is one of mutual influence: For instance, changes in the microtubule network act on formation of actin-based cell protrusions. On the other hand, correct orientation of the mitotic spindle as well as of motile cilia, both Tubulin-based structures, requires an intact cortical and subcortical net of actin (Bezanilla *et al,* 2015), (Herawati *et al,* 2016). Likewise, intermediate filaments Gfap and Vimentin have been implied in the control of cell polarity, assembly of actin-based protrusions and cell migration, as well as position and orientation of the nucleus (Hohmann & Dehghani, 2019).

Similarly, membranes and cytoskeletal elements connect at many points. At the interface of the plasmalemma and cytoskeleton, the involvement of the actin cytoskeleton is especially significant. Endocytosis, migration, cytokinesis, and formation of various types of cell protrusions and cell-cell contacts require coordination of membranes and actin cytoskeleton (Merino *et al,* 2020), (Svitkina, 2018). In the interaction of plasma membrane and Actin, phosphoinositides such as phosphatidylinositol 4,5-bisphosphate ($PI(4,5)P_2$) are a salient actor (Bezanilla *et al,* 2015). Besides its interaction with inverted Bin-Amphiphysin-Rvs (I-BAR) domain

proteins, which are drawn to $PI(4,5)P_2$-rich membrane portions and concentrate it further (Zhao *et al,* 2011), $PI(4,5)P_2$ also interacts with other actin-modulating proteins and cytoskeletal components, such as septins, cofilins and profilins (Bezanilla *et al,* 2015), (Zhao *et al,* 2011).

The significance of membranes and cytoskeleton proteins for proliferation and apoptosis should be noted also: Cell culture experiments have demonstrated how imposed changes in cellular geometry alter cell proliferation. They also unveiled mechanisms linking cell geometry to chromatin condensation state and thus gene expression (Jain *et al,* 2013). A mutual interaction between nuclear deformation and state of differentiation of E1 ependymal cells has also been reported, with nuclear deformation being an accompanying feature of normal differentiation, but also artificial cell compression being a factor that promotes differentiation. Here, the actin cytoskeleton acts as a mediator of this interaction. When disturbing the function of LINC, a protein complex linking nucleus and actin cytoskeleton, E1 cell differentiation and its accompanying nuclear deformation are disrupted (Basso *et al,* 2025). Actin within the nucleus itself has even been shown to be involved in DNA replication (Hohmann & Dehghani, 2019). In apoptosis, actin is not only executing downstream effects of apoptosis such as cell rounding and membrane blebbing, but also acts as an initiator of apoptosis pathways together with the actin-membrane linking protein Ezrin (Desouza *et al,* 2012). In conclusion, several mechanisms can be identified, by which membrane and cytoskeleton dynamics affect cell proliferation, migration, and apoptosis.

2.2.1 Planar Cell Polarity

For cell polarity, interaction of cytoskeleton and cell membrane is indispensable. As cell polarity is a key mechanism controlling neurodevelopment and function of the ependyma, it is given a brief introduction here. Emphasis will be placed on one aspect of polarity, which is called planar cell polarity (PCP). Cell polarity has more than one axis: Taking epithelial cells as an example, polarity along the apical-basolateral axis, and polarity parallel to the epithelial surface exist. The former deals with the differences between the parts of the cell facing towards the surface of the epithelium, and the parts facing towards its basal membrane, for instance the distribution of cell adhesion molecules to different domains on the plasma membrane. The latter is referred to as PCP, and deals with differences along the surface of the cell, such as the arrangement of outer hair cells in the cochlea (Lee & Streuli, 2014), (Carvajal-Gonzalez *et al,* 2016).

In PCP, cellular asymmetry is established through mechanisms such as heterophilic interaction of adhesion molecules, extracellular signalling via secreted proteins acting on surface receptors, or cues from the microtubule cytoskeleton. These actors then recruit effector proteins that remodel both the actin- and microtubule cytoskeleton, eventually controlling factors such as centriole positioning, generation of cell protrusions (Carvajal-Gonzalez *et al,* 2016), or cell shape, contributing to the morphology of whole tissues (van der Spuy *et al,* 2023). Noteworthy pathways associated with PCP are the Ft and Ds (Ft-PCP) pathway and the Fz-PCP or core PCP pathway (Carvajal-Gonzalez *et al,* 2016). PCP has been shown to affect a wide range of processes. In the context of neural development of mice, these include the already mentioned convergent extension in neural tube closure (Nikolopoulou *et al,* 2017), axon and dendrite morphogenesis, neuronal cell migration (Wang & Nathans,

2007), axon guidance (Tissir & Goffinet, 2013), (Kim *et al,* 2024), controlling neurogenesis via uptake of retinoic acid (Boucherie *et al,* 2018), and positioning and orientation of cilia (Boutin *et al,* 2014), as also depicted in Figure 4. Studies carried out in fruit fly and zebrafish furthermore have pointed towards a role of PCP genes in orienting the plane of mitosis and cell division (Segalen & Bellaïche, 2009), (Ségalen *et al,* 2010), which are of key importance in neuro- and gliogenesis as well (Penisson *et al,* 2019).

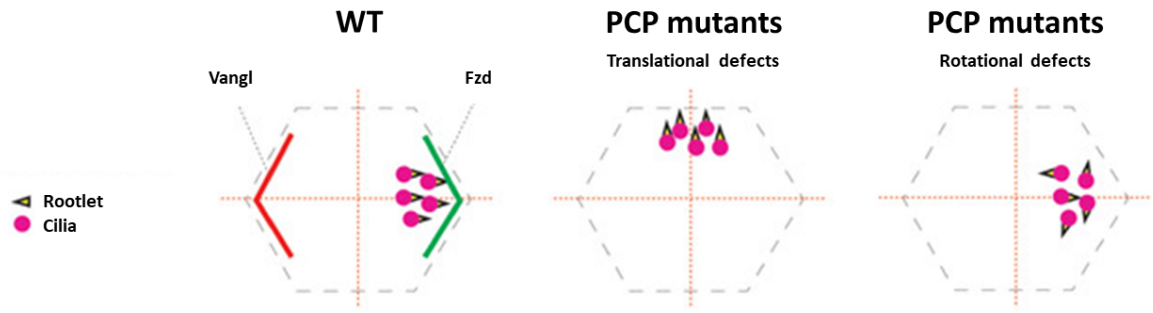

Figure 4: Effects of PCP-Related Mutations

Planar cell polarity in ependymal cells is established by asymmetrically localised membrane proteins such as Fzd and Vangl. PCP affects polarity with regard to both the positioning of cilia in relation to the centre of the cell surface (translational) and the orientation of individual cilia (rotational). Figure modified, by Carvajal-Gonzalez et al (2016).

2.2.2 Neural Cell Migration

As mentioned earlier, neurons as well as glia have to migrate from germinal zones to their specific final destination. Like PCP, migration is a cytoskeleton- and membrane-driven process, and shall briefly be explained here. Newborn neurons initially exhibit multipolar morphology, but, under extensive remodelling of the cytoskeleton, shift to a bipolar appearance: They retract most of their protrusions, but specialise the remaining two into a leading process and an axon. The leading process indicates the direction of migration in response to guidance cues, such as secreted factors and cell

adhesion molecules present on the adequate substrate. The cell shifts forward the contents of its soma using specialised microtubules and dynein. First, it elongates its nucleus, and develops a proximal compartment of the leading process called cytoplasmic dilation. Both processes depend on the microtubule cytoskeleton. The cell then transfers its nucleus, Golgi apparatus and centrosome into this newly formed compartment, while contracting its posterior end in an actomyosin-mediated manner.

Migration also depends on adhesion of membrane proteins. For instance, radially migrating neurons follow the fibres of RGCs. In the leading process, the N-cadherin at the cell's surface allows it to adhere to RGCs. As the cell moves forward, N-cadherin at the cell's posterior end is taken up by endocytosis and recycled to the leading process again (Stouffer *et al,* 2016), (Kawauchi, 2015). Intriguingly, gap-junction forming proteins Cx43 and Cx26 have been demonstrated to enhance cell adhesion in neuronal migration, with knockdown of these connexins adversely affecting cell distribution in the neocortex. However, their function to form channels between neighbouring cells was dispensable for this process (Elias *et al,* 2007). Close to their target, migrating neurons change their migration mode to a "terminal translocation mode", in which a shift in participating adhesion molecules occurs. Consequently, this mode is again independent of RGC fibres (Kawauchi, 2015).

2.3 Mtss1

The protein-coding gene metastasis suppressor 1 (Mtss1), also referred to as missing-in-metastasis (MIM), is found on chromosome 8 in humans and on chromosome 15 in mice (Sayers *et al,* 2024), (Sayers *et al,* 2025a), (Sayers *et al,* 2025b). Its protein product belongs to the I-BAR domain family of proteins, which is

conserved in chordates, nematodes and arthropods (Yamagishi *et al,* 2004). Apart from Mtss1, mice express four more proteins of this family: IRSp53/Baiap2, IRTKS/Baiap2L1, Pinkbar/Baiap2l2 and Abba/Mtss1L (Chou *et al,* 2017).

2.3.1 Mtss1 Expression Pattern and Related Diseases

True to its name, Mtss1 has originally been standing out for its role in various types of tumours (Zhao *et al,* 2011). On one hand, high Mtss1 expression has been reported to be a bad prognosis in early cancer development, which might be explained by increased amounts of Egfr (epidermal growth factor-receptor) on cells highly expressing Mtss1 (Dawson *et al,* 2012b). On the other hand, via Rac1 interaction, Mtss1 recruits actin and E-cadherin to cell-cell contacts and thus strengthens them, a mechanism that has been proposed to prevent epithelial-mesenchymal transition and thus explain why loss of Mtss1 may promote metastasis (Dawson *et al,* 2012a).

In healthy adult mice, Mtss1 is present in skeletal muscle, skin, liver, heart, kidney (Bershteyn *et al,* 2010), (Zhao *et al,* 2011), spleen, especially splenic B-cells (Sarapulov *et al,* 2020), and hematopoietic stem- and progenitor cells (Zhan *et al,* 2016). It is also present in primary human endothelial cells (Podieh *et al,* 2024). In humans, genome-wide association studies imply Mtss1 to play a role in cardiac development and consequently also in the progress of heart failure (Aung *et al,* 2019). This finding could be confirmed in the mouse model, where deficiency of Mtss1 did indeed impact cardiac morphogenesis (Morley *et al,* 2019). In the fish species *Oryzias latipes*, Mtss1 KO leads to severe malformations of the cardiovascular system and even death in early development (Meyer *et al,* 2020). Heart defects are also associated with mutations in in another I-BAR-domain-protein, IRSP53 (Chou *et al,* 2017). Mtss1 deficient leukocytes exhibit increased homing to

the bone marrow, but also the spleen, resulting in more leukocytes in the respective organs, but fewer leukocytes in peripheral blood. Indeed, one consequence of Mtss1 deficiency in mice is splenomegaly. (Zhan *et al,* 2016). Another developmental disorder relating to Mtss1 deficiency in mice is renal cysts with hyperproliferation of epithelium in renal tubules. In this context, Mtss1 was discovered to be regulated by fluid flow, and was speculated to stabilise cell-cell contacts and cell polarity in the kidney (Xia *et al,* 2010). Mtss1 has also been reported to promote osteoblast differentiation in cell culture, with Mtss1 –knockout and -knockdown mice both having bone abnormalities (Chen *et al,* 2022), (Saarikangas *et al,* 2011). Mtss1 deficiency also causes several neurodevelopmental disorders, which will be discussed in the following section. Overall however, Mtss1 KO mice are viable and fertile.

2.3.2 Mtss1 in the CNS

Most important to this thesis is the role of MTTS1 in the CNS: During pre- and early postnatal development, neurons of the hippocampal formation, cerebellum and cerebral cortex show strong Mtss1 expression (Saarikangas *et al,* 2015). Notably, in some of these cells, it is only transiently present (such as cerebellar granule cells), while in others (such as Purkinje cells), Mtss1 expression is maintained in adulthood (Glassmann *et al,* 2007), (Zhao *et al,* 2011). Much of the data on Mtss1 distribution are based on in-situ hybridisation, and thus yields information on expression on mRNA level only. However, available data on protein expression also localise Mtss1 to Purkinje cells as well as to hippocampal pyramidal cells of CA1 and CA3 regions as well as granule cells of the dentate gyrus in the adult mouse. Mtss1 was not found in $Gfap^{+}$ glia, in contrast to its paralogue Abba/Mtss1L (Zhao *et al,* 2011), (Saarikangas *et al,* 2015). In contrast, a wealth of cancer research points towards

Mtss1 expression in human astrocytes, as it is a well-known factor in glioblastoma. There, Mtss1 expression is actually lower in poor-prognosis neoplasms than in primary cell culture controls of astrocytes (Zhang & Qi, 2015). Astrocytes derived from induced pluripotent stem cells also expressed Mtss1 (Luxen *et al,* 2017). Moreover, various partially conflicting reports exist on the exact subcellular localisation of Mtss1, summarised in (Kawabata, 2018). These reports point towards expression in soma and dendrites, but not axons of Purkinje cells (Saarikangas *et al,* 2015), axon, soma and dendrites of Purkinje cells (Hayn-Leichsenring *et al,* 2011), basal bodies of primary cilia in primary dermal cells and primary embryonic fibroblast (Bershteyn *et al,* 2010), and actin fibres and focal contacts in induced pluripotent stem cell-derived astrocytes (Luxen *et al,* 2017).

In mice, deficiency of Mtss1 leads to altered morphology and death of Purkinje cells, granule cell ectopy in the cerebellum (Sistig *et al,* 2017), increased ventricular volume at the cost of cortical volume and hippocampal malformations. This goes along with altered anxiety and defects of learning and motor functions (Minkeviciene *et al,* 2019). Other I-BAR domain proteins have been linked to CNS function and development as well (Chou *et al,* 2017), (Huang *et al,* 2022). In *Xenopus laevis*, knockdown of the Mtss1 homologue XMIM produced neural tube closure defects, which could not be rescued by expression of a XMIM fragment containing only its I-BAR domain (Liu *et al,* 2011). To my knowledge, there exists no indication of a comparable phenotype being linked to murine Mtss1.

2.3.3 Domains and Molecular Functions

In general, Mtss1 has been dubbed a scaffolding protein for its many interfaces with other proteins, especially in the context of cytoskeleton remodelling. Like other

proteins of its family, Mtss1 features an I-BAR domain at its N-terminus. As outlined in Figure 5, I-BAR domain proteins form homodimers that bind membrane portions rich in PI(4,5)P_2. There, they form convex protrusions both by electrostatic interaction between the membrane and curved I-BAR-domain and by promoting actin polymerisation at cell-cell contacts and filopodia. This happens by direct interaction with actin, but also by interplay with actin- and cell-cell contact-modulating proteins such as Rac1 (Dawson *et al,* 2012a), (Matskova *et al,* 2024), (Podieh *et al,* 2024). The I-BAR domain of Mtss1, like that of Pinkbar and Abba specifically carries an N-terminal α-helix that is inserted into membranes and thus strengthens membrane binding (Saarikangas *et al,* 2009), (Matskova *et al,* 2024). Additionally, I-BAR domain proteins have been shown to cluster the phospholipid PI(4,5)P_2 (Zhao *et al,* 2011), (Saarikangas *et al,* 2009).

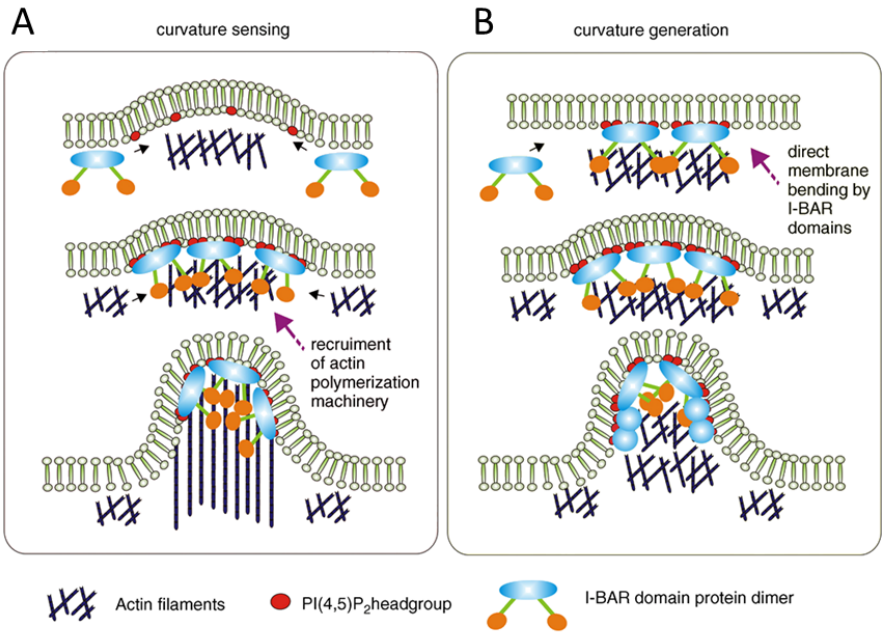

Figure 5: Protrusion-Related Mechanisms of Mtss1

A: *In the proposed mechanism of curvature sensing, homodimers of Mtss1 bind membrane portions rich in PI(4,5)P_2. There, they recruit actin-polymerising proteins to a site of membrane curvature.* ***B:*** *In the proposed mechanism of curvature generation, Mtss1 dimers induce curvature in membranes using their I-BAR domain. Both processes interact to establish cell protrusions. Figure modified, from Zhao et al (2011), reproduced with permission (License Number 6079280444584).*

At its C-terminus, Mtss1 possesses a WH2-domain, which slows down WASP mediated nucleation and polymerisation of actin by competition for G-actin (Lee *et al,* 2007), (Matskova *et al,* 2024), (Lin *et al,* 2005). Close to its C-terminal region, Mtss1 also contains a proline-rich sequence, which enhances the functions of the actin polymerising protein Cortactin (Zhao *et al,* 2011), (Lin *et al,* 2005). The same region interacts with yet another actin-modulating protein, Daam1. Daam1 has been revealed to control dendritic protrusion length in coordination with Mtss1 (Kawabata Galbraith *et al,* 2018), (Kawabata, 2018). Preceding this, Mtss1 also interacts with the protein EVL to promote formation of dendritic spines in the first place (Parker *et al,* 2023). An additional interface with the cytoskeleton is the centre region of Mtss1, which recruits α-actinin 4. By this function, Mtss1 participates in membrane ruffling (Matskova *et al,* 2024).

This proline-, threonine- and serine-rich centre of Mtss1 furthermore contains numerous phosphorylation sites. These have been shown to be targeted by various phosphorylating and dephosphorylating enzymes (Kawabata, 2018), (Zeleniak *et al,* 2018). Examples include the kinase Src and the phosphatases CKIδ and PTEN. Src controls the aforementioned membrane ruffling activity of Mtss1, likely in response to stimulation with platelet-derived growth factor (Wang *et al,* 2007). CKIδ marks Mtss1 for proteasome degradation (Zhong *et al,* 2013), while PTEN stabilises Mtss1 against degradation (Zeleniak *et al,* 2018).

Short motifs found on Mtss1 include evolutionary conserved nuclear localisation- and nuclear export signals, some of which are contained within the I-BAR domain of Mtss1. A number of these sequences are also found on Mtss1 paralogue IRSp53 but others are unique to Mtss1 and its homologues in other species (Glassmann *et al,* 2007), (Petrov *et al,* 2019). Different splice variants of Mtss1 do exist and their

expression varies according to cell type and time point in development (Glassmann *et al,* 2007), suggesting that not each of the listed domains need to play a role in every function of Mtss1.

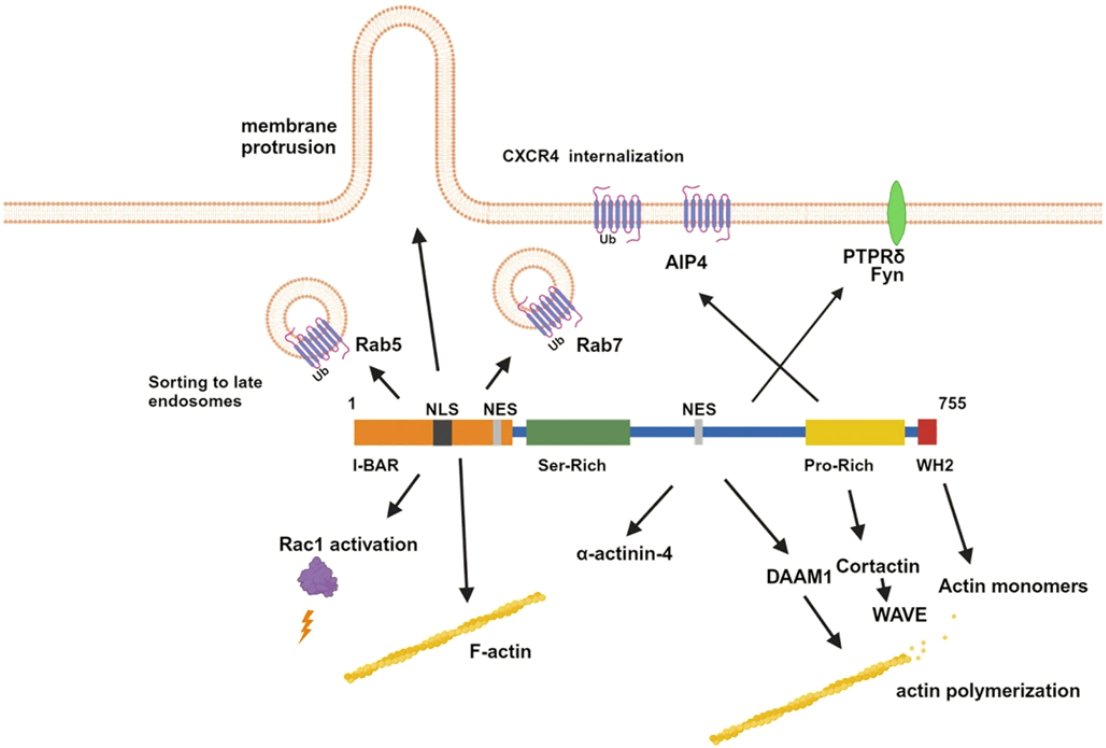

Figure 6: Protein Domains of Mtss1 and Their Functions

*Mtss1 participates in regulation of the actin cytoskeleton directly via its I-BAR and WH2-domain, and indirectly via its interaction with cytoskeleton-modulating proteins, notably including Cortactin, Daam1 and Rac1. It participates in sensing and generating membrane curvature by direct interaction with membrane lipids, and in endocytosis by interaction with Cxcr4, Aip4, Rab5 and Rab7. Mtss1 also contains nuclear localisation- (NLS) and export sequences (NES). Figure modified, from Matskova et al (2024), published under a creative commons attribution 4.0 license (*https://creativecommons.org/licenses/by/4.0/*).*

Mtss1 plays a role in downstream responses to B-cell receptor binding (Sarapulov *et al,* 2020), and in the internalisation of Cxcr4, a mechanism that is made responsible for the altered trafficking of leukocytes found in Mtss1 deficient mice (Zhan *et al,* 2016). Other reported data point towards a role of Mtss1 in endocytosis and autophagy (Bompard *et al,* 2005), (Matskova *et al,* 2024). Notable interaction

partners of Mtss1 in this context are, besides the just mentioned Cxcr4, the AP-2 adaptor protein complex, Rab5 and Rab7 (Li *et al,* 2017), (Petrov *et al,* 2019). Mtss1 has also been implied to in the context of Sonic Hedgehog signalling, albeit with conflicting outcomes (Bershteyn *et al,* 2010), (Saarikangas *et al,* 2011), (Liu *et al,* 2011). Lastly, Mtss1 seems to be controlled in a cell-cycle dependent manner by interaction with polo like kinases 1 and 4 as well as NEK2 (Petrov *et al,* 2019), (Sayers *et al,* 2011), (Sayers *et al,* 2015), (Sayers *et al,* 2025c).

Many documented functions of Mtss1 on a cellular level engage with cell protrusions. These include filopodia and lamellipodia (Matskova *et al,* 2024), dendritic spines (Saarikangas *et al,* 2015), (Kawabata Galbraith *et al,* 2018) and primary cilia (Bershteyn *et al,* 2010). Several other I-BAR domain proteins interact with cell protrusions as well (Zhao *et al,* 2011), (Pykäläinen *et al,* 2011). Mtss1 has been shown to be responsible for shedding of extracellular vesicles from filopodia, that contain signalling molecules, including its own interaction partner Rac1 (Matskova *et al,* 2024). It can also stabilise E-cadherin based cell-cell contacts, secondarily inhibiting collective cell migration without affecting motility of individual cells, as demonstrated in cell culture (Dawson *et al,* 2012a). On the other hand, investigation of cerebellar granule cells in development suggests Mtss1 to be of importance specifically during migration (Glassmann *et al,* 2007).

2.4 Purpose of the Project

Mtss1 deficiency leads to various malformation of the CNS. Previous research showed that Mtss1 influences neural cells by more than one mechanism, as illustrated by the cerebellar phenotype of Mtss1 KO mice. Preliminary experiments conducted by myself and our research group suggested planar cell polarity to be disturbed in Mtss1 KO mice. As cell polarity is a key factor to cell proliferation, and adult Mtss1 KO mice are characterised by a lack of telencephalic tissue, I hypothesised that Mtss1 impacts the neural cytoarchitecture of the mouse telencephalon by acting on cell proliferation, possibly via the PCP pathway.

This project thus aimed at investigating what significance the expression of Mtss1 has to proliferation in the telencephalon. Specifically, the following questions were to be answered:

1. Does Mtss1 impact proliferation in the telencephalon?
2. If so, which cell types and developmental time points are affected?
3. Does Mtss1 influence PCP, and does this play a role in neurodevelopment?

3 Materials and Methods

3.1 List of Materials

Table 1 is a list of general laboratory materials. Table 2 indicates the antibodies used in this project, while Table 3 indicates used polymerase chain reaction (PCR) primers.

Table 1: Table of General Materials Used

Consumables	
Material	**Source**
Cell Culture Flask, 25cm^2	TPP
Cell Culture Plastic Petri Dish	TPP
Centrifuge- and Reaction Tubes, various	Roth, Greiner, Eppendorf, TPP
Costar Stripette 5mL; 10mL; 25mL Serological Pipette	Corning
Coverslips, various sizes	Marienfeld
Gloves, various	Meditrade
Multiwell Plates	TPP, Nunclon
Pipettes and pipette tips, various	Biozym, Ratiolab, Labomedic, Corning, Sarstedt , Gilson
Superfrost Microscopy Slide	Thermo Fisher Scientific
Various Centrifuge and Reaction Tubes	Roth, Greiner, Eppendorf, TPP
Devices	
Material	**Source**
AcuJetPro	Brand
AF80 Flake Ice Machine	Scotsman
Axioscope 2	Zeiss
Bead Bath	Lab Armor
Biofuge Prime	Heraeus
Biofuge Primo R	Heraeus
CFX 96 C1000 Touch	Bio-Rad
DFC350FX Camera	Leica
DMIRE2 Laser Scanning Microscope	Leica
DS-Fi2 Camera	Nikon
DS-U3 Camera Controller	Nikon
EclipseNi	Nikon

FAZ3 Laminar Flow Hood	Waldner
Freezers	Liebherr
GelDoc 2000 Transilluminator	Biorad
Heracell 150 Incubator	Heraeus
Heracell 150i Incubator	Heraeus
Heraeus Pico 17 Centrifuge	Thermo Fisher Scientific
Histocore Arcadia H Embedding Station	Leica
HxP 120V Lamp	Jena
Improved Neubauer Counting Chamber	Brand
LifeTouch	Bioer
Mastercycler ep	Eppendorf
Microm HM 355S Microtome	Thermo Fisher Scientific
Microm HM 560 Cryostat	Thermo Fisher Scientific
MTM I Vacuum Tissue Processor	Slee
NIS-Elements Imaging Software	Nikon
Ovens	Heraeus
Photometrics Coolsnap EZ	Visitron
Pipetboy Comfort Pipetting Aid	Integra Biosciences
PowerPac 300 Power Supply	Biorad
PowerPac Basic Power Supply	Biorad
Precellys 24 Bead Homogeniser	Bertin Technologies
PTC200	MJ Research
Pump	Vacuubrand
Quantitiy OneAnalysis Software	Biorad
Qubit 2.0 Fluorometer	Thermo Fisher Scientific
Refrigerators	Liebherr
Scales, various	Mettler-Toledo, Sartorius
Seven Compact pH Meter	Mettler-Toledo
Stemi 2000C Stereomicroscope	Zeiss
Sub-Cell GT Cell Electrophoresis Chamber	Biorad
Thermomixer 5436	Eppendorf
Experimental Animal Lines	
Line	**Source**
C57BL/6J	Janvier Labs
Mtss1 d/d	Xia *et al.* (2010)
Miscellaneous Materials	
Material	**Source**
10x Trypsin-EDTA	Gibco
3,3′-diaminobenzidine tetrahydrochloride hydrate	Sigma
Acetone	Roth
Agarose	Biozym
Altromin LASQCdiet TRpd16Auto 10 mm Zero	Altromin

Mouse Feed	
Ampuwa Sterile Ultrapure Water	Fresenius Kabi
Cresyl Violet Acetate	Sigma
DEPC-Treated Water	Roth
DePeX mounting medium	Serva
DMEM Medium	Gibco
DMSO	Thermo Fisher Scientific
DNase I	Invitrogen
DreamTaq Buffer	Thermo Fisher Scientific
Ethanol 70%	Roth
Ethidium Bromide (10mg/mL)	Sigma
Fetal Calf Serum	Gibco
Fluorescence Mounting Medium	Dako
Gene Ruler 100bp Ladder	Thermo Fisher Scientific
H2O2 30%	Merck
Hepes	Gibco
Hoechst 33342	Sigma
iScript Kit	Bio-Rad
Kaisers Glycerin-Gelatine phenolfrei	Roth
L15 Medium	Gibco
Methanol	Roth
NaN_3	Serva
Paraformaldehyde	Serva
Penicillin/Streptomycin	Gibco
peqGOLD TriFast™ Extraction Reagent	VWR Chemicals
Porcine Type A Gelatin	Sigma
Potassiumhexacyanoferrate (II)	Merck
Potassiumhexacyanoferrate (III)	Merck
Proteinase K	Roth
Pursept AF	Schülke
ROTI Cell 10x PBS	Roth
Sodium Bicarbonate	Gibco
Trisodium citrate dihydrate	Applichem Panreac
TRITC-conjugated Phalloidin	Sigma
Triton X-100	Sigma
Trypan Blue	Chroma Gesellschaft Schmid & Co
Vectastain ABC Reaction Kit	Vector
X-Gal	Labomedic
Software	
Material	**Source**
Citavi	Swiss Academic Software GmbH
Office Professional Plus 2016	Microsoft

PyRAT System	Scionics
Fiji	Schindelin *et al.* (2012)
R	R Core Team
Rstudio	Posit Team

Table 2: Antibodies Used

Primary Antibodies					
AK	**Host**	**Clones**	**Provider**	**Catalogue No.**	**Dilution**
Acetylated Tubulin	ms	Monoclonal	Sigma-Aldrich	T7451	1:500 – 1:1000
beta-Catentin	rb	Polyclonal	Sigma-Aldrich	C2206	1:900
Centriolin	ms	Monoclonal	Santa Cruz	sc-365521	1:200 - 1:400
Ki67	rb	Polyclonal	Abcam	ab15580	1:600
Ki67	ms	Monoclonal	eBioscience	14-5699-82	1:500
ODF2	ms	Monoclonal	NovusBio	H00004957-M01	1:200
Pax6	rb	Polyclonal	Proteintech	12323-1-AP	1:400-1:600
Sox2	ms	Monoclonal	Santa Cruz	sc-365964	1:50
Tbr2	rb	Monoclonal	Abcam	ab183991	1:400
ZO1	rat	Monoclonal	Santa Cruz	sc-33725	1:200 - 1:500
γ-Tubulin	rb	Polyclonal	Sigma-Aldrich	T3539	1:500
Secondary Antibodies					
AK	**Host**	**Clones**	**Provider**	**Catalogue No.**	**Dilution**
Donkey α-mouse Cy5	dk	Polyclonal	JacksonImmunoResearch	715-175-150	1:1000
Goat α-mouse 488	gt	Polyclonal	Invitrogen	A11029	1:800 - 1:1000
Goat α-mouse 546	gt	Polyclonal	Invitrogen	A11030	1:800 - 1:1000
Goat α-mouse biotinylated	gt	Polyclonal	Vector	BA-1000	1:200
Goat α-rabbit 488	gt	Polyclonal	Invitrogen	A11034	1:800 - 1:1000
Goat α-rabbit 546	gt	Polyclonal	Invitrogen	A11035	1:800 - 1:1000
Goat α-rabbit biotinylated	gt	Polyclonal	Vector	BA-9200	1:200
Goat α-rabbit Cy5	gt	Polyclonal	JacksonImmunoResearch	111-175-144	1:1000
Goat α-rat 546	gt	Polyclonal	MolecularProbes	A-11081	1:1000

Table 3: Primers Used for RT-qPCR with Respective Catalogoue Number at Thermo Fisher Scientific

Target	Catalogue No.
Apaf1	Mm01223701_m1
Bak1	Mm00432045_m1
Bax	Mm00432051_m1
Casp3	Mm01195085_m1
Dcx	Mm00438400_m1
Foxj1	Mm01267279_m1
Gap	Mm99999915_g1
Gfap	Mm01253033_m1
Gja1	Mm01179639_s1
Kif2c	Mm00728630_m1
Ki67	Mm01278617_m1
Mtss1	Mm00460614_m1
Pax6	Mm01334068_m1
Pcna	Mm00448100_g1
Slc1a3	Mm4448892_m1
Sox2	Mm00436785_m1
S100b	Mm00436528_m1
Tbr1	Mm00493433_m1
Tbr2	Mm01351984_m1
Top2a	Mm01296339_m1
Top2b	Mm00493776_m1
Yap1	Mm 01143263_m1

3.2 Animal Husbandry

The model organism employed in this thesis are Mtss1Gt(RRI034)Byg - mice, a knock-out line of Mtss1 and simultaneous knock-in of the reporter gene lacZ on the background C57BL/6JRj of *Mus musculus*. This KO was achieved by insertion of a construct containing a splice acceptor site and ß-geo (coding for ß-galactosidase) between exons 1 and 2 of Mtss1. The according mice were first described in (Xia *et al,* 2010) and kindly provided by Dr. Rong Li of The Stowers Institute for Medical Research, Kansas City, MO (also see Baldarelli *et al* (2025), Baldarelli *et al* (2024)). The knockout construct contains a splice acceptor site upstream of the bacterial gene

lacZ, followed by a neomycin resistance gene. These knockout mice were crossed into the existing BL/6 line available in Anatomical Institute, Bonn University, which was established in 2001 based on C57BL/6JRj. The use of experimental animals for this project complied with the applicable animal welfare laws, and in accordance with the guidelines from Directive 2010/63/EU. Breeding of mice and use of their organs and tissue for scientific purposes was licensed by Veterinäramt Bonn according to Tierschutzgesetz §11 (1) no. 1 of German federal law. All mice were housed under 12h dark/light cycling, controlled air pressure, temperature and humidity, and received food and water from the same supply ad libitum. Mice were transferred to clean cages once to twice per week. Cages fulfilled established area requirements per mouse and contained retreat space.

3.3 Genotyping of Experimental Animals

Ear biopsies of juvenile mice or tail tips of sacrificed mice were subjected to proteinase K digestion in 100µL or 200µL of digestion solution (see Table 4) over night at 57°C. Proteinase was inactivated at 97°C for 20min, and the samples centrifuged for 5min at 12,000xg to separate undigested tissue from DNA-containing supernatant.

Table 4: Contents of Digestion Solution for DNA Isolation per Sample

Ingredient	Volume
H_2O	87.5µL
DreamTaq Buffer 10x	10µL
Proteinase K	2.5µL

Polymerase chain reaction was run on a thermal cycler (LifeTouch, Bioer), using the program shown in Table 6. For the reaction mix composition, see Table 5. The

forward primer used served in both amplification of the wild type (WT) allele and the KO allele, while the reverse primer binding the KO or the WT allele were different. For nucleotide sequences of primers used, see Table 7.

Table 5: Contents of PCR Reaction Mix per Sample

Ingredient	Volume
Sterile Ultrapure Water	10µL
MM 5x	4µL
DMSO	1µL
Primer 50 5µM	1µL
Primer 51 5µM	1µL
Primer 52 5µM	1µL
DNA Sample	2µL

Table 6: PCR Program used in Genotyping of Mtss1 Mice

Step	Temperature [°C]	Duration	Cycles
1	95	12min	1
2	95	10s	30
3	62	40s	
4	72	20s	
5	72	5min	1
6	4	10min	1
7	12	hold	1

Table 7: Primer Sequences used in Genotyping of Mtss1 Mice

Name	Sequence
50 MIM wt s	AAA GTG CAG TCG AGC GCA TCT GTG TCA TCA
51 MIM as	GGT GCT TAA CCA GGG ATG ATT TGG CCT
52 MIM trap s	CGC AGT GTT ATC ACT CAT GGT TAT GGC AGC ACT

The amplificate was loaded on an agarose gel (1% w/v agarose, 0.0025% v/v ethidium bromide) next to a DNA ladder (Thermo Fisher Scientific) and subjected to electrophoresis in Tris-Borate-EDTA buffer (see Table 8) using a PowerPac Basic

power supply and electrophoresis chamber (both Biorad), before visualisation using a GelDoc 2000 Transilluminator and the Quantity One analysis software (also Biorad). In result, if a fragment of ca 300 base pairs (bp) was amplified, a WT allele was detected. If a fragment of ca 500bp was amplified, a KO allele was present.

Table 8: Contents Tris-Borate-EDTA Buffer for Gel Electrophoresis

Solution was adjusted to pH 8.0

Ingredient	Concentration
Tris	89mM
H_3BO_3	89mM
Na_2-EDTA	2mM

3.4 RT-qPCR

For evaluation of gene expression on RNA level, real time- quantitative PCRs (RT-qPCR) were performed.

3.4.1 RNA Isolation and Generation of cDNA

Brain samples for RT-qPCR were prepared by extracting the brain and removing cerebellum and brain stem with forceps. Anterior brains of adult mice were separated into hemispheres before further processing. Diencephalon and hippocampus were removed, the posterior part of the telencephalon was transferred to extraction reagent (also see Figure 7). The samples were bead-homogenised (Precellys 24, Bertin) in phenol based nucleic acid/protein extraction reagent (Peqlab, 30-2010) and stored at -20°C. RNA was isolated by adding 200µL chloroform per mL of extraction reagent, mixing gently, and keeping for 3min at room temperature (RT). Next, samples were centrifuged at 4°C for 15min at 12,000xg. The RNA containing supernatant was transferred to a new vessel and 500µL of isopropanol were added

per mL of extraction reagent in order to precipitate nucleic acids. The samples were vortexed and then incubated for 15min at RT, before being centrifuged again at 4°C for 15min at 12,000xg. The supernatant was discarded and the pellet washed and centrifuged twice with 75% Ethanol at 4°C for 3min at 7500xg. Ethanol was carefully removed and the pellet dried for 10min, before being resuspended in 44µL of diethyl pyrocarbonate (DEPC)-treated water (Roth) and heated to 65°C for 10min to dissolve RNA. Samples were kept on ice between steps from now on. DNA was digested by adding DNaseI (Invitrogen) and incubating at 37°C for 15min. DNase was inactivated by adding 2.5µL of 0.1M ethylenediaminetetraacetic acid (EDTA) and heating to 75°C for 15min. The resulting solution was kept on ice or stored at -80°C. RNA content and purity was verified using by fluorometer (Qubit 2.0, Invitrogen). cDNA was generated by applying iscript cDNA synthesis kit (Biorad) according to package instructions (see Table 9 for reaction components). Per sample, 50ng of RNA and a total reaction volume of 20µL were used. The program used for reverse transcription is shown in Table 10. The resulting cDNA containing solution was diluted 1:20 and kept at -20°C.

Table 9: Components of Reverse Transcription Reaction Mix

Ingredient	Volume
5x iScript Reaction Mix	4µL
iScript Reverse Transcriptase	1µL
50ng RNA template	variable
Nuclease-free water	ad 20µL total, according to RNA solution volume

Table 10: Program used for Reverse Transcription

Step	Temperature [°C]	Duration
1	25	5min
2	42	30min
3	85	5min
4	4	hold

3.4.2 RT-qPCR

RT-qPCRs were prepared on 96-well plates on ice. Technical triplicates were prepared for each target-sample-combination. The components of RT-qPCR reaction mix are given in Table 11.

Table 11: Components of RT-qPCR Reaction Mix

Ingredient	Volume
TaqMan Primer Mix	0.5µL
2x Gene Expression MM	5µL
cDNA Template (1:20)	3µL
Nuclease Free Water	1.5µL

Complementary DNA (cDNA) was amplified and measured using a CFX 96 C1000 Touch cycler (Biorad) and the primers listed in Table 3. The PCR program is displayed in Table 12.

Table 12: PCR Program used in RT-qPCR

Step	Temperature [°C]	Duration	Cycles
1	50	2min	1
2	95	10min	1
3	95	15s	40
4	60	1min	
5	65	30s	1
6	65	31s	1
7	65-95; + 0.5/cycle	5s	61
8	12	30s	1

Expression of each target was adjusted to expression of Gapdh in the same sample. Evaluation of the outcomes was done as follows:

1. Triplicates with only one valid measurement were disregarded
2. The median of Cq values from each triplicate was calculated
3. Measurements were sorted out. They qualified for evaluation if:
    a) The difference between Cq and its median was < 0.5
    b) Only 2 Cq-values were available
4. Mean Cq-value for Gapdh of the same sample was calculated
5. ΔCq was calculated:

    $\Delta Cq = Cq - \text{mean } Cq(Gapdh)$
6. Relative expression was calculated:

    $\text{Relative Expression} = 2^{-\Delta Cq}$

3.5 Histological Methods

3.5.1 Sample Preparation

To yield frontal sections of P0 mice meant for paraffin embedding, brains were isolated using sharp forceps and transferred to ice-cold phosphate-buffered saline (PBS) by Roth. In the occipital third of the telencephalon, a frontal-plane cut was made to discard mesencephalon, cerebellum and occipital part of the telencephalon. Brains were then immersion-fixed in 2% paraformaldehyde (PFA) (see Table 13) over night, rinsed in daily exchanged tap water for one week, and transferred into 70% Ethanol. They were dehydrated further and embedded in paraffin using a vacuum tissue processor (Slee). They were then sectioned into 8µm specimens using a

Microm HM 355S Microtome and Baked at 60°C for 20h. Paraffin sections were stored at room temperature.

Table 13: Components of Fixation Solution

Solution was prepared by heating phosphate buffer to 60° before addition of PFA and some drops of 5M NaOH. The solution was covered and stirred for 1h before pH was adjusted to 7.2

Ingredient	Concentration
Na_2HPO_4	100mM
NaH_2PO_4	100mM
PFA	4% (w/v)

Telencephalon samples from adult mice meant for cryosections were obtained by inserting biopsy punches (pfm medical, 48501, diameter = 5mm) at the caudal lateral telencephalon, at the intersection of visual, auditory, and temporal association areas (see also Figure 9). Punches were immediately embedded in TissueTek mounting medium (Sakura), frozen over liquid nitrogen, and transferred to storage at -20°C. They were sectioned into 18µm specimens using a Microm HM 560 Cryostat and mounted on Superfrost microscopy glass slides (Thermo Fisher Scientific). Sections were also stored at -20°C.

3.5.2 Immunofluorescence of Ventricle Wholemounts

Dissection of mouse brains to yield lateral ventricle wholemounts was done in a similar procedure as described by Mirzadeh *et al* (2010), and is outlined in Figure 7. Briefly, employing a stereomicroscope, an agarose gel surface, ophthalmic scissors, ophthalmic scalpels, curved and straight forceps and insect pins, brains were immersed in PBS, the hemispheres separated and placed with the cut face downward. In the occipital third of the telencephalon, a frontal-plane cut was made to discard mesencephalon, cerebellum and occipital part of the telencephalon. The sample was then fixed on the gel using insect pins with the cut face upward. The diencephalon was removed using forceps and scalpel. The hippocampus was mobilised cutting diagonally from occipital toward the crest and peeled away from the lateral ventricle. After another cut near the frontal attachment point of the hippocampus, it could be removed completely. The sample was briefly treated in BRB80-buffer (see Table 14) with 0.1% Triton TX-100 for 1min, and then fixed in methanol at -20°C for 20min before further processing. Afterwards, using scissors and scalpel, the overhanging parts of the telencephalon were removed. The medial-facing ventricular surface was dislodged from the hemisphere, trying to obtain a slice as thin as possible, which was used for immunofluorescence staining the same day.

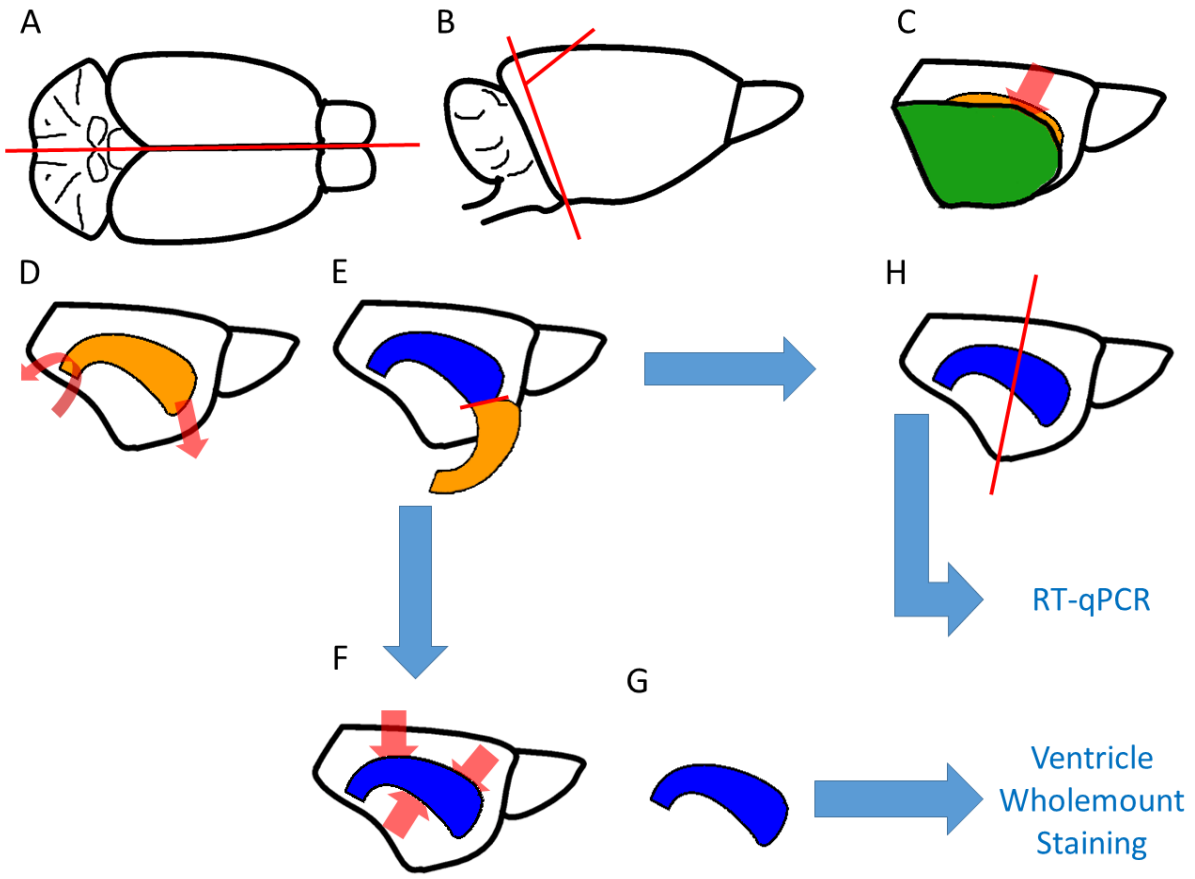

Figure 7: Dissection Procedure to Yield Lateral Ventricle Wholemounts and Samples for qPCRs

A: *Brains were separated into hemispheres.* ***B:*** *Caudalmost parts were removed.* ***C:*** *Diencephalon was removed.* ***D, E:*** *Hippocampus was removed.* ***F, G:*** *In order to yield ventricle wholemounts for staining, lateral wall of the lateral ventricle was dislodged from underlying tissue.* ***H:*** *In order to yield samples for qPCRs, remaining posterior part of the telencephalon was dislodged and transferred to extraction reagent. Illustration by Barbara Kalthoff and Clemens Wagner.*

Ventricle wholemounts for immunofluorescence were blocked in 10% foetal calf serum (FCS) or normal goat serum (NGS) and 0.05-0.1% Triton-100 in BRB-80 buffer for 1-2 h or over night. No antigen retrieval or further permeabilisation were performed. Primary antibodies were applied for 1-2h or over night, and samples washed at least 3x 5min in PBS. Secondary antibodies were applied for 1-2h, Samples were washed again 3x 5min, transferred to deionised water, and mounted using Fluoromount-G with 4′,6-Diamidino-2-Phenylindole (DAPI) (Invitrogen, 00-

4959-52). As the wholemounts were hundreds of µm thick, an enclosure made of nail polish was prepared on the microscope slide in which to place the wholemount as to preserve its structure rather than compressing it during mounting.

Table 14: Components of BRB80 Buffer

Solution was adjusted to pH 6.8

Ingredient	Concentration
K-Pipes	80mM
Na-EGTA (0.5M)	5mM
$MgCl_2$	5mM

3.5.3 Immunofluorescence of Paraffin Sections

Paraffin-embedded specimens were Baked again at 60°C for 30min. Next, they were deparaffinated using xylene (3x 100%, 10min), 3x ethanol (3x 100%, then 90%, 70% and 50%, 5min each), distilled water (1min) and finally PBS for 5min. Depending on the primary antibody used, they were boiled in citrate buffer adjusted to pH 6 or tris-EDTA-buffer at pH 9 (see Table 15 and Table 16) for 15-20min, both with 0.1 - 0.3 % Tween-20 to unmask epitopes and permeabilise cells. Blocking was performed using 0.2% gelatin or 10% NGS in PBS. Primary antibodies were usually applied overnight, at 4°C. See Table 2 for antibody dilutions used. The sections were washed with PBS, before secondary antibodies were applied for 1h at RT in the dark. The specimens were washed again in PBS and deionised water, and mounted using Fluorescence Mounting Medium Fluoromount-G with DAPI (Thermo Fisher Scientific).

Table 15: Components of Tris-EDTA Buffer for Immunofluorescence

pH was adjusted to 9.0.

Ingredient	Concentration
Tris	10mM
Na_2-EDTA	1mM

Table 16: Components of Citrate Buffer for Immunofluorescence

pH was adjusted to 6.0 with citric acid.

Ingredient	Concentration
$C_6H_5Na_3O_7$	12mM

3.5.4 Nissl Staining of Cryosections

Nissl staining was employed for envisioning neurons in cryosections of caudal telencephalon of adult mice. It stains nucleic acids, chiefly showing cell nuclei and ribosomes, including those on the rough endoplasmic reticulum (ER). This makes the staining strong in cells with very active protein production, such as neurons. Astrocytes are poorly stained using this method (Kádár *et al,* 2009). Sections were treated with 0.1 % Cresyl Violet acetate solution for 5min. Development took place in 95% ethanol for about 1-10min under constant inspection. Sections were dehydrated in 100% ethanol (3x 2min) and 100% xylene (3x 2min) before they were covered using DePeX mounting medium (Serva). Stained sections were stored at RT.

3.5.5 Immunostaining of Cryosections and Mtss1 Promoter Activity

In order to envision promoter activity linked to Mtss1 expression, activity of the beta-galactosidase encoded by the LacZ gene present in the Mtss1 KO construct was visualised using Xgal (“β-gal Staining”). Cryosections used for this procedure were fixated for 5min in 4% PFA, then washed in β-gal-staining wash solution for twice for 5min, before being incubated in staining solution at 37°C over night in the dark. Afterwards, they were again washed in β-gal-staining wash solution twice for 5min, in demineralised water for 5min, and mounted in Kaiser’s Glycerin-Gelatine (Roth). For details on used solutions, see Tables 17, 18 and 19.

Table 17: Components of β-gal Base Solution

Solution was prepared by dissolving Components in H2O and adjusting pH to 8.0.

Ingredient	Concentration
NaH_2PO_4	100mM
Na_2HPO_4	100mM
$MgCl_2$	2mM
EGTA	5mM

Table 18: Components of β-gal Wash Solution

Ingredient	Volume
Na-Deoxycholat (10%)	50µL
10% Nonidet P40 (10%)	100µL
β-gal Base Solution (Table 17)	50mL

Table 19: Components of β-gal Staining Solution

Ingredient	Volume
Xgal (4%, dissolved in DMSO)	2.5mL
β-gal Base Solution (Table 17)	95.5mL
Potassium Hexacyanoferrate(II) (0.5M)	1mL
Potassium Hexacyanoferrate(III) (0.5M)	1mL

Endogenous peroxidases of the tissue were blocked by applying 1% hydrogen peroxide + 10% Methanol in PBS for 10min. Blocking of unspecific protein binding was performed using 0.2% gelatin, 0.1% Tx-100 in PBS for at least 1h. Primary antibodies were applied overnight at 4°C (see Table 2 for dilutions). The sections were washed with PBS 3x 5min. Sections were again washed in PBS and biotinylated secondary antibodies were applied for 1h at RT. The specimens were again washed 3x in PBS for 5min, before being treated with ABC reagent (Vector Laboratories) at 1:100 dilution for 1h at RT. Enzymatic development of the stainings was started by adding 0,05% 3,3′-Diaminobenzidine (DAB) + hydrogen peroxide 1:500 in PBS under constant inspection. Development was stopped by

washing in PBS. Slices were then washed in deionised water and mounted with Kaiser's Glycerin-Gelatine (Roth).

3.6 Image Acquisition and Evaluation

Unless otherwise noted, a Nikon Eclipse TI2 confocal microscope operated in galvano mode was used for capturing images of immunofluorescence stainings.

3.6.1 Determining Number of B1 Cells in Ependyma

Ventricle wholemounts were generated as described in section 3.5.2. The basal body component Centriolin (1:200, Santa Cruz, sc-365521) and tight-junction component ZO1 (1:200, Santa Cruz, sc-33725) were stained using the indicated antibodies, and visualised using a 60x objective and scan size settings that resulted in images of size 295µm x 295µm. B1 cells, recognised by their small apical processes few cilial basal bodies were manually counted using Fiji 2.0.0-2.16.0 (Schindelin *et al,* 2012) and MTrackJ 1.5.2 (Meijering *et al,* 2012). Example evaluations are shown next to the corresponding results. In order to adjust the total number for comparison between images, the evaluated area was measured using the polygon selection in Fiji.

3.6.2 Determining Rotational Polarity of Motile Cilia

Ventricle wholemounts were prepared as described in section 3.5.2. Basal body components Centriolin (1:200-1:400, Santa Cruz, sc-365521) and γ-Tubulin (1:500, Sigma-Aldrich, T3539) were stained using the indicated antibodies and visualised using a 60x objective, and scan size settings that resulted in images of 291µm x 291µm. Gain, focal plane and intensity were set individually. Fiji (Schindelin *et al,* 2012) and MTrackJ (Meijering *et al,* 2012) were used for evaluating angles between

the top of the image and a line given by neighbouring point-like signals for Centriolin and γ-Tubulin. Signals that were distant, strongly overlapping, or obviously not belonging to multiciliated cells were neglected. 25 fields (58µm x 58µm) each for the anterior and posterior part of the lateral ventricle for each mouse and 3 - 4 animals were evaluated per genotype. Example evaluations are shown next to the corresponding results. Mean angles, angular deviations and angular variances were calculated using R and the packages listed in Table 20.

3.6.3 Determining Translational Polarity of Ependymal Cells

Ventricle wholemounts were prepared as described in section 3.5.2. As cilium orientation can be determined by the relative positions of basal body components (Herawati *et al,* 2016), Centriolin (1:200-1:400, Santa Cruz, sc-365521) or γ-Tubulin (1:500, Sigma-Aldrich, T3539) as well as tight-junction component ZO1 (1:500, Santa Cruz, sc-33725) were stained using the indicated antibodies, and visualised using a 40x objective, resulting in images of size 439µm x 439µm. Evaluation was performed using Fiji (Schindelin *et al,* 2012) and MTrackJ (Meijering *et al,* 2012), drawing tracks from the cell centre to the centre of the basal body patch, determined manually. The evaluated angles are the angles between a reference (the top of the image) and the line between these points. Cells were disregarded if such tracks could not be drawn confidently, such as in very small cells. 25 fields (87.8µm x 87.8µm) each for the anterior and posterior part of the lateral ventricle for each mouse and 3 - 4 animals were evaluated per genotype. Example evaluations are shown next to the corresponding results. Mean angles, angular deviations and angular variances were calculated using R and the packages listed in Table 20.

Two cells were classified as facing towards each other as described in Figure 8.

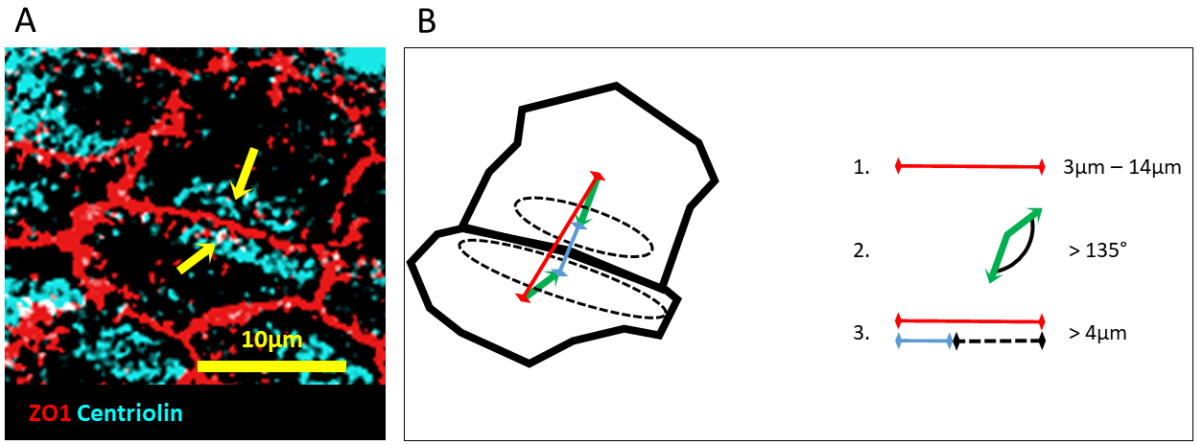

Figure 8: Example Classification of Two Cells Facing Each Other

A: *Micrograph of ependymal cells stained for ZO1 and Centriolin. Angles and distances between cell centres and centres of basal body patches marked in yellow.*

B: *Classification of the same cells as facing each other as follows:*

a) The cell fulfils criteria 1 - 3

1. *The distance between the cell centres of two neighbouring cells must be between 3µm and 14µm*
2. *The difference in angles from cell centre to basal body patch between those cells must be > 135°*
3. *The cell centre of the nearest cell must be further away than the basal body patch of the same cell and that difference must be > 4µm*

b) The cell is nearest neighbour of a cell fulfilling criteria 1 – 3 (determined by distance between cell centres)

3.6.4 Determining Tbr2 and Pax6 Expression Profile

Frontal paraffin sections of newborn mice were cut as described in section 3.5.1. Expression and cellular localisation of the IPC marker Tbr2 (1:400, Abcam, ab183991) or apical RGC marker Pax6 (1:500, Proteintech, 12323-1-AP) analysed using the indicated antibody, and visualised using a 20x objective, resulting in images of various size. Evaluation was performed using Fiji (Schindelin *et al,* 2012). By using the line selection tool, rectangular regions of interest (width = 117µm – 417µm) were

delineated, conforming to the shape of the ventricle roof. The plot profile function was then employed to record colour intensity along the axis of ventricular zone to the outer surface of the cerebral cortex. These profile plots were evaluated as shown and illustrated in the results section 4.3.2.

3.6.5 Evaluating Composition of Ventricular Zone and Subventricular Zone of Newborn Mice

For immunofluorescence stainings, frontal sections (paraffin, 8µm) of newborn mice were cut as described in section 3.5.1. In order to identify proliferating cells, proliferation marker Ki67 (1:600, Abcam, ab15580) was stained using the indicated antibody. The stainings were visualised using a 20x (for lateral VZ-SVZ) or 40x (for roof VZ-SVZ) objective and scan settings that yielded images of 444µm x 222µm, 444µm x 111µm or 158µm x 79µm, depending on the depth of the germinal zone. $Ki67^+$ cells, defined as cells with $Ki67^+$ nuclei, were manually counted using Fiji (Schindelin *et al,* 2012) and the Plugin MTrackJ (Meijering *et al,* 2012). The evaluated areas were recorded using polygon or freehand selections, the evaluated distances by freehand line tool. This allowed the ratio of cell number per area or distance of ventricular surface to be calculated.

For combined β-gal- and immunohistochemical DAB stainings, cryosections were cut as described in section 3.5.1, and stained as described in section 3.5.5. Images were taken using a Nikon EclipseNi Microscope and Nikon DS-Fi2 Camera.

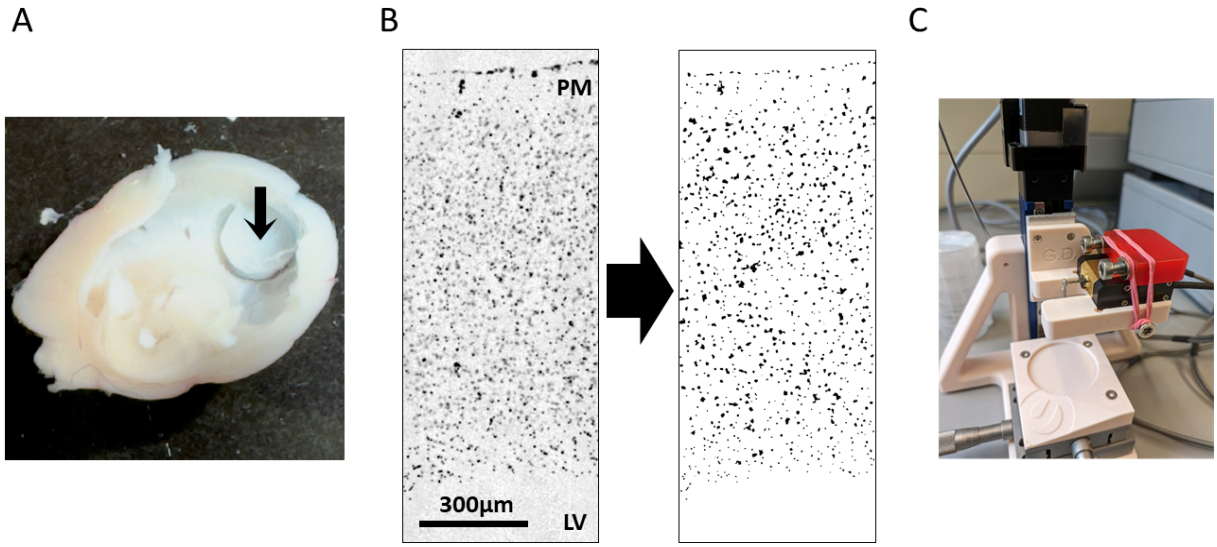

Figure 9: Evaluating Morphology of Caudal Telencephalon

A: *Point of biopsy punches was located in the caudal lateral telencephalon, at the intersection of visual, auditory, and temporal association areas (arrow) (Allen Institute for Brain Science, 2008). Indentations were made at the same position.* ***B:*** *Evaluation of example Nissl staining. Each dot visible in B is counted as one cell.* ***C:*** *Microindentor used for measuring distance from ependyma to meninges as outlined in section 3.7.1.*

3.7 Determining the Composition of the Caudal Telencephalon

3.7.1 Mechanical Properties of Caudal Telencephalon and Distance from Ependyma to Meninges

Ventricle wholemounts were prepared in a procedure similar to the one outlined in Figure 7, except it was performed in PBS and the occipital telencephalon was not discarded. Instead, rostral parts of the brain were removed in order to allow the occipital part to be laid flatly on a petri dish. Immediately before the measurement, PBS was carefully withdrawn from the dish, and a custom made microindentor was used to lower a probe of 2mm diameter onto the surface of the lateral ventricle at the position indicated in Figure 9. The microindentor was lowered stepwise to the tissue, reducing step size down to 10µm before contact. In order to account for plastic properties of the tissue and its possibly uneven surface, contact with the tissue was

defined as the point at which a force of at least 0.2 mN was maintained for 60s. This contact position was defined as 0µm. The probe was then lowered at a velocity of 0.2mm/s, indenting the tissue. The continuous force acting on the probe was measured at an interval of 0.1s. Indenting the tissue consisted of 10 steps of 30µm each, with a pause of 7.5s after each step. The probe was then withdrawn in the same manner. Afterwards, the sample was removed, and the probe lowered onto the surface of the petri dish, again taking care to decrease step size to 10µm before contact. The measured distance from position 0µm to the contact point with the dish surface was recorded as distance from ependyma to meninges of the caudal telencephalon. Contact with the dish surface was defined as the first point at which a force of 0.2 mN was measured again. An example indentation graph is provided in the appendix, Figure 29.

This series of experiments was done in close collaboration with a team of Institut für Biologische Informationsprozesse 2: Mechanobiologie at Forschungszentrum Jülich: Design of the test was led by Prof. Dr. Rudolf Merkel, Jens Konrad constructed the microindentor, Georg Dreissen and Sven Gerlach operated the indentor and evaluated data, Ronald Springer evaluated data.

3.7.2 Cell Number and DNA Content of Caudal Telencephalon

Ventricle wholemounts were obtained as described in section 3.7.1, and two punch biopsies (pfm medical, 48501, diameter = 5mm) were taken per brain, one from each cerebral hemisphere: One biopsy was subjected to proteinase K digestion in 100µL of digestion solution (see Table 4) and subsequent centrifugation at 12,000 xg for 5min. The DNA concentration in the supernatant was then measured. The other biopsy was immediately frozen and subjected to Nissl staining (as outlined in section

3.5.4). These stainings were visualised using a Nikon EclipseNi Microscope and Nikon DS-Fi2 Camera, yielding images of 2776µm x 1735µm. Stained cells were counted in fields (width 360µm - 577µm) by selecting rectangular regions of interest conforming to the shape of the ventricle roof similar as outlined in Figure 9, using the line selection tool of Fiji (Schindelin *et al,* 2012). Contrast was automatically increased as also exemplified in Figure 9, and the “Find Maxima” function was used to automatically select cells. Total number of counted cells was adjusted to width of the evaluated compartment.

3.8 Data Evaluation

Data was evaluated using R 3.5.0 - 4.4.1 (R Core Team, 2021) in RStudio (Posit Team, 2023). Circular mean was calculated using the R package “Directional” and the definition of circular mean provided in Mardia & Jupp (2000). Angular variance was calculated using the package “Circular” and the definition of angular variance provided in Mardia & Jupp (2000). Angular deviation was calculated using the package “Circular” and the definition of angular deviation provided in Batschelet (1981). For a list of R packages used, see Table 20.

Table 20: R Packages Employed for Data Evaluation

Package	Citation
here	Müller K (2020). here: A Simpler Way to Find Your Files. R package version 1.0.1
ggpubr	Kassambara A (2023). ggpubr: 'ggplot2' Based Publication Ready Plots. R package version 0.6.0
pwr	Champely S (2020). pwr: Basic Functions for Power Analysis. R package version 1.3-0
MultNonParam	Jankowski S (2023). MultNonParam: Multivariate Nonparametric Methods. R package version 1.3.9
readxl	Wickham H, Bryan J (2023). readxl: Read Excel Files. R package version 1.4.3
effsize	Torchiano M (2020). effsize: Efficient Effect Size Computation. R package version 0.8.1
tidyverse	Wickham H, Averick M, Bryan J, Chang W, McGowan LD, François R, Grolemund G, Hayes A, Henry L, Hester J, Kuhn M, Pedersen TL, Miller E, Bache SM, Müller K, Ooms J, Robinson D, Seidel DP, Spinu V, Takahashi K, Vaughan D, Wilke C, Woo K, Yutani H (2019). “Welcome to the tidyverse.” _Journal of Open Source Software, *4*(43), 1686. doi:10.21105/joss.01686 <https://doi.org/10.21105/joss.01686>.
spatstat	Baddeley A, RuBak E, Turner R (2015). Spatial Point Patterns: Methodology and Applications with R. Chapman and Hall/CRC Press, London. <https://www.routledge.com/Spatial-Point-Patterns-Methodology-and-Applications-with-R/Baddeley-RuBak-Turner/p/book/9781482210200/>.ISBN 9781482210200,
ggquiver	O'Hara-Wild M (2021). ggquiver: Quiver Plots for 'ggplot2'. R package version 0.3.2
multcomp	Hothorn T, Bretz F, Westfall P (2008). “Simultaneous Inference in General Parametric Models.” _Biometrical Journal, *50*(3), 346-363.
ggstatsplot	Patil, I. (2021). Visualizations with statistical details: The 'ggstatsplot' approach. Journal of Open Source Software, 6(61), 3167, doi:10.21105/joss.03167
Hmisc	Harrell Jr F (2023). Hmisc: Harrell Miscellaneous. R package version 5.1-1
Directional	Tsagris M, Athineou G, Adam C, Yu Z (2024). Directional: A Collection of Functions for Directional Data Analysis. R package version 6.9
DescTools	Signorell A (2023). DescTools: Tools for Descriptive Statistics. R package version 0.99.52
smatr	Warton, David I., Duursma, Remko A., Falster, Daniel S. and Taskinen, Sara (2012) smatr 3 - an R package for estimation and inference about allometric lines Methods in Ecology and Evolution, 3(2), 257-259
compiler	R Core Team (2023). R: A Language and Environment for Statistical Computing. R Foundation for Statistical Computing, Vienna, Austria. <https://www.R-project.org/>
tectonicr	Stephan et al. (2023). Analyzing the horizontal orientation of the crustal stress adjacent to plate boundaries. Sci Rep, 13(1), 15590. https://doi.org/10.1038/s41598-023-42433-2
circular	Agostinelli, C. and Lund, U. (2024). R package 'circular': Circular Statistics (version 0.5-1). https://CRAN.R-project.org/package=circular

4 Results

4.1 Distance from Ependyma to Meninges and Cell Numbers are Reduced in Caudal Telencephalon of Mtss1 Deficient Mice

Visual observations of gross brain morphology in Mtss1 deficient mice and the existing literature suggest an effect of Mtss1 on development of the telencephalon (Minkeviciene *et al,* 2019), (Saarikangas *et al,* 2015). However, different models of Mtss1 deficiency in mice exist (Kawabata, 2018). In order to confirm this finding in our model, brains of adult Mtss1 KO and WT mice were compared with regard to the macroscopic morphology of the telencephalon as well as abundance of cells and DNA therein.

4.1.1 Distance from Ependyma to Meninges and Mechanical Properties

Mechanical properties of adult murine telencephalon and distance from ependyma to meninges, (which includes white and grey matter, ependyma and pia mater, but is colloquially referred to as “cortical thickness”), were assessed.

This was done using a custom build microindentor kindly provided by the Institut für Biologische Informationsprozesse 2: Mechanobiologie at Forschungszentrum Jülich, as described in section 3.7.1. As Figure 10 shows for the caudal telencephalon, resisting force at an indentation to 90µm and 300µm is significantly higher in Mtss1 KO mice. However, distance from ependyma to meninges is also significantly reduced in Mtss1 KO mice. In order to unveil possible interaction between the resisting force and the distance from ependyma to meninges, standardised major axis estimation (Warton *et al,* 2012) was employed. The analysis did not reveal

significant differences in slope or elevation of the function of force vs distance from ependyma to meninges between the two genotypes, although a shift along the common main axis is present, with measurements displaying both significantly higher distance and lower force tending to be observed in WT mice. Hence, differences in measured force could be attributed to differences in distance from ependyma to meninges.

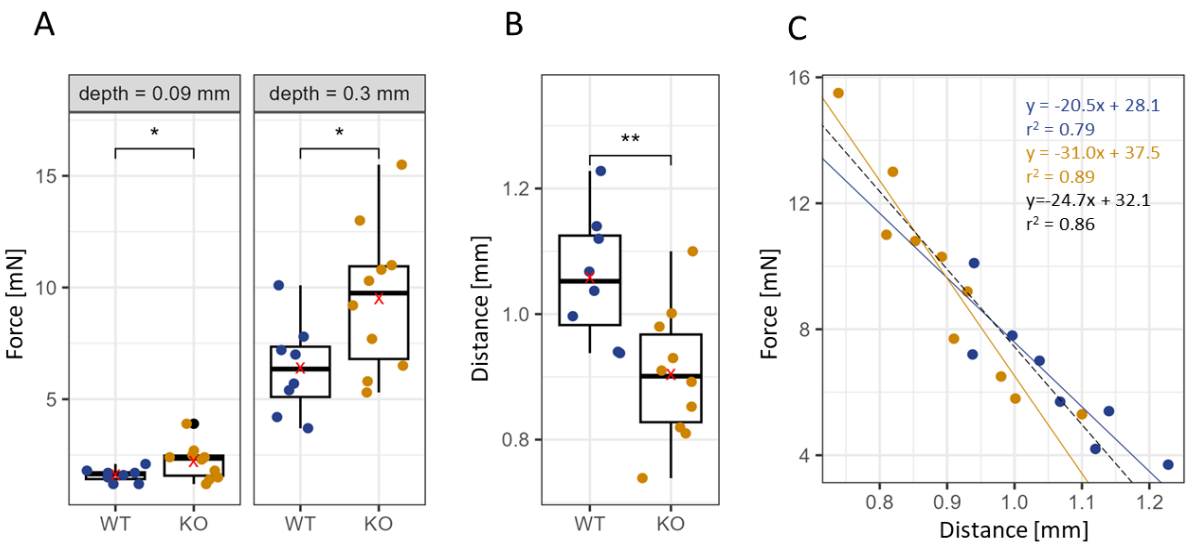

Figure 10: Distance from Ependyma to Meninges and Measured Force upon Indentation of Caudal Telencephalon of Adult Mice

A: *Force measured by microindentor as described in sections 3.7.1 and 4.1.1. n = 4-5 mice/genotype, 2 hemispheres/mouse.* ***B:*** *Distance from ependyma to meninges measured as also laid out in section 3.7.1. n = 4-5 mice/genotype, 2 hemispheres/mouse.* ***C:*** *Linear Relationship of Distance and Force. Dashed line: All values. Blue: WT. Yellow: KO. Difference in elevation between WT and KO: p=0.13. Difference in Slope: p=0.91. Difference in Shift: p=0.01. Regression and statistical significance determined by standardised major axis estimation (Warton et al, 2012). Red X marks the average value. Statistical significance for A and B determined by Welch's t-test: ns: p>0.05 ; *: p≤0.05 ; **: p≤0.01 ; ***: p≤0.001.*

4.1.2 Cell Numbers and DNA Content

In order to clarify whether the observed differences in distance from ependyma to meninges correlated with an altered numbers of cells, punch biopsies were isolated from adult murine telencephalon. These were used for measuring DNA content and evaluating cell numbers by Nissl staining. The position of the punch biopsies was chosen to be the same as was used for measuring distance and mechanical properties. As Figure 11 shows, both DNA content and numbers of cells visualised by Nissl staining are significantly lower in Mtss1 KO mice.

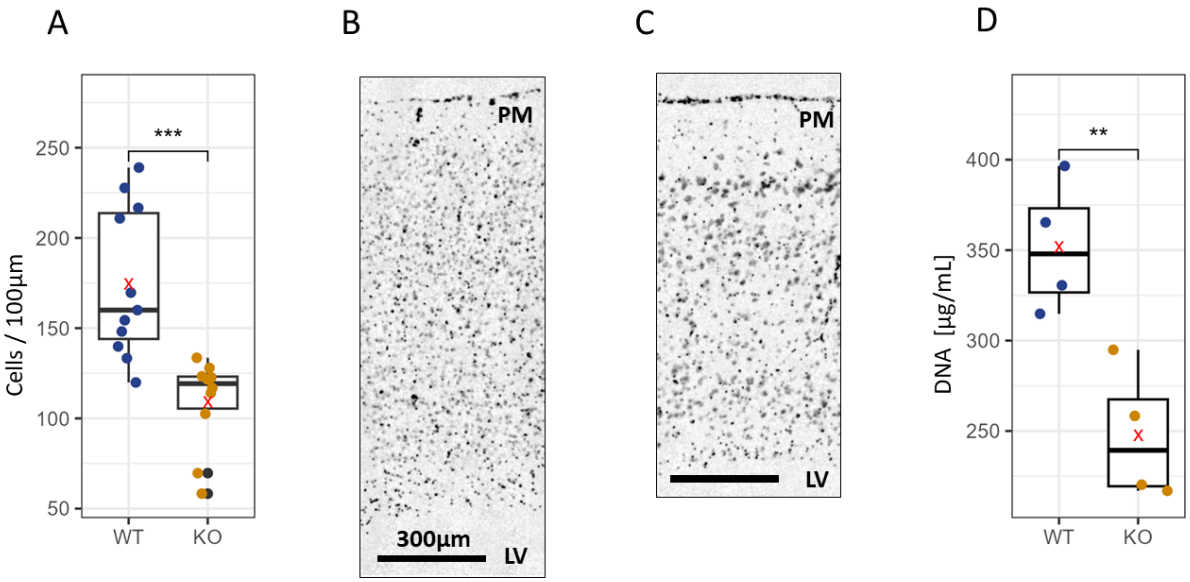

Figure 11: Number of Cells and DNA Content of Caudal Telencephalon Samples of Adult Mice

A: *Relative number of cells marked by Nissl staining per 100µm width of the evaluation field. n= 4 mice/genotype, 1-4 sections/mouse.* ***B:*** *Example Nissl staining of WT Telencephalon* ***C:*** *Example Nissl staining of KO Telencephalon. Thickness of sections = 18µm.* ***D:*** *DNA concentrations in the lysates of punch biopsies after proteinase K digestion and centrifugation. n = 4 mice/genotype. Red X marks the average value. Statistical significance determined by Welch's t-test: ns: p>0.05 ; *: p≤0.05 ; **: p≤0.01 ; ***: p≤0.001.*

4.2 The Gene Expression in Posterior Telencephalon of Mtss1 KO Mice is Altered

The reduced distance from ependyma to meninges and cell numbers in Mtss1 deficient mice raised the question which population of cells is reduced and whether this is to be attributed to a developmental process, or a later loss of cells. These questions were investigated using RT-qPCR on RNA samples from posterior telencephalon (prepared as stated in section 3.4.1). Samples were taken from mice at different developmental stages (E18, P0, P7 and Adult mice). The expression of cell type markers as well as the expression of genes associated with apoptosis and proliferation were measured. The expression was compared to expression of ubiquitously present Gapdh in the same sample, resulting in relative expression values. Considered markers have been sorted according to their function (as markers for cell types, such as neural precursors, or processes, such as apoptosis) for convenience of interpretation, and will be presented separately in this chapter. This is also true for genes, which could be attributed to more than one group.

4.2.1 Developmental Course of mRNA Expression in Posterior Telencephalon

Table 21 shows the genes investigated by RT-qPCR, a list of their biological roles relevant in the context of CNS development, and according references.

Table 21: Marker Genes Measured in RT-qPCRs and their Roles

Gene	Role	References
Pax6	RGC marker, but in the adult expressed by both VZ-SVZ adult neural progenitor cells and a subset of neurons	Li *et al* (2021a), Li *et al* (2021b), Boucherie *et al* (2018), Penisson *et al* (2019), Duan *et al (*2013)
Sox2	Marker of RGCs, glial precursors, adult neural stem cells, proliferating astrocytes, ependymal cells	Li *et al (*2021a), Li *et al* (2021b), Boucherie *et al* (2018), Penisson *et al* (2019), Bani-Yaghoub *et al* (2006)
Tbr2	Marker of neurogenic IPCs	Penisson *et al* (2019), Hevner (2019)
Dcx	Marker of migrating neurons	Kawauchi (2015)
Rbfox/ NeuN	Marker of mature neurons	Magavi *et al* (2012)
Tbr1	Marker of developing, but postmitotic projection neurons, especially of layer V to VI	Molyneaux *et al* (2007*)*, Englund *et al* (2005)
Foxj1	Marker of E1 ependymal cells and their precursors	Redmond *et al* (2019)
Gfap	Marker of white matter astrocytes, reactive astrocytes and ependymal B1 cells	Ortiz-Álvarez *et al* (2019), Huang *et al* (2023)
Slc1a3/ Glast	Marker of astrocytes and RGCs	Huang *et al* (2023), Zhang *et al* (2023)
Yap1	Expressed in RGCs, E1 cells and astrocytes	Terry & Kim (2022), Huang *et al* (2016)
S100b	Marker of grey matter astrocytes and differentiating oligodendrocytes as well as E1 cells	Huang *et al* (2023), Redmond *et al* (2019)
Ki67	DNA replication and transcription	Bologna-Molina *et al* (2013), Stamatiou *et al* (2024)
Pcna	Replication, cell-cycle control, DNA repair and chromatin assembly	Wang *et al* (2024)
Kif2c	Centromere attachment of the mitotic spindle	McHugh *et al* (2019)
Top2a	Topoisomerase-coding gene, chromosome condensation in mitosis, transcriptional regulation, forms heterodimers with Top2b, in neuronal development mostly expressed in proliferative cells, but not mature neurons	Nielsen *et al* (2020), Nevin *et al* (2011), Harkin *et al* (2016)
Top2b	Topoisomerase-coding gene, DNA replication, transcriptional regulation, forms heterodimers with Top2a, control of neurite targeting, neocortex lamination, control of cell adhesion, present in postmitotic neurons	Nielsen *et al* (2020), Uusküla-Reimand *et al* (2016), Nevin *et al* (2011), Harkin *et al* (2016)
Casp3	Effector caspase in apoptosis, late player of programmed cell death, mediation of activity-dependent apoptosis of cortical neurons in early postnatal development	Cavalcante *et al* (2019)
Apaf1	Acts directly on Casp3	Cavalcante *et al* (2019)
Bak1	Pro-apoptotic regulator of the intrinsic pathway upstream of Apaf1, roles in control of neural progenitor cells and CNS development	Cavalcante *et al* (2019), Lindsten *et al* (2003)
Bax	Pro-apoptotic regulator of the intrinsic pathway upstream of Apaf1, roles in control of neural progenitor cells and CNS development	Cavalcante *et al* (2019), Lindsten *et al* (2003)
Egfr	Present in various cell types in neural development, switch of neurogenesis to gliogenesis, interaction partner of Mtss1	Zhang *et al* (2023), Dawson *et al* (2012b)

As an overview, Figure 12 shows averaged gene expression of some of the investigated markers of neural progenitor cells, neurons, glia, apoptosis and proliferation over the course of all investigated time points, focusing on temporal changes less than on differences between the genotypes. Gene expression at the individual time points that includes statistical evaluation is reviewed in detail starting from section 4.2.2. As to be seen, the first panel shows expression of progenitor cell markers. Pax6 and Sox2, are both expected in RGCs but not neurogenic IPCs. Furthermore, Sox2 is expressed in glial precursors until quiescence. In adult mice, it is found in astrocytes which currently proliferate, in adult neural stem cells and ependymal cells. Expression of both Pax6 and Sox2 decreases between E18 and P0 mice, with pronounced differences between WT and KO mice at E18. Sox2 expression then rises between P0 and adulthood, while Pax6 expression continues to fall. Expression of Tbr2, marking for (neurogenic) IPCs also decreases with age, albeit at changing rates. Again, differences between WT and KO mice are most pronounced in early developmental stages, and disappear in adulthood. Neuronal markers considered in Figure 12 are Dcx (expressed in migrating neurons Rbfox3/NeuN (expressed in mature neurons) and Tbr1 (expressed in developing but postmitotic projection neurons, especially of layer V to VI. Expression of Dcx and Tbr1 decreases over time, while expression of Rbfox3 increases. Differences between the genotypes are greatest at E18 for Dcx, P0 for Tbr1, and P7 for Rbfox3.

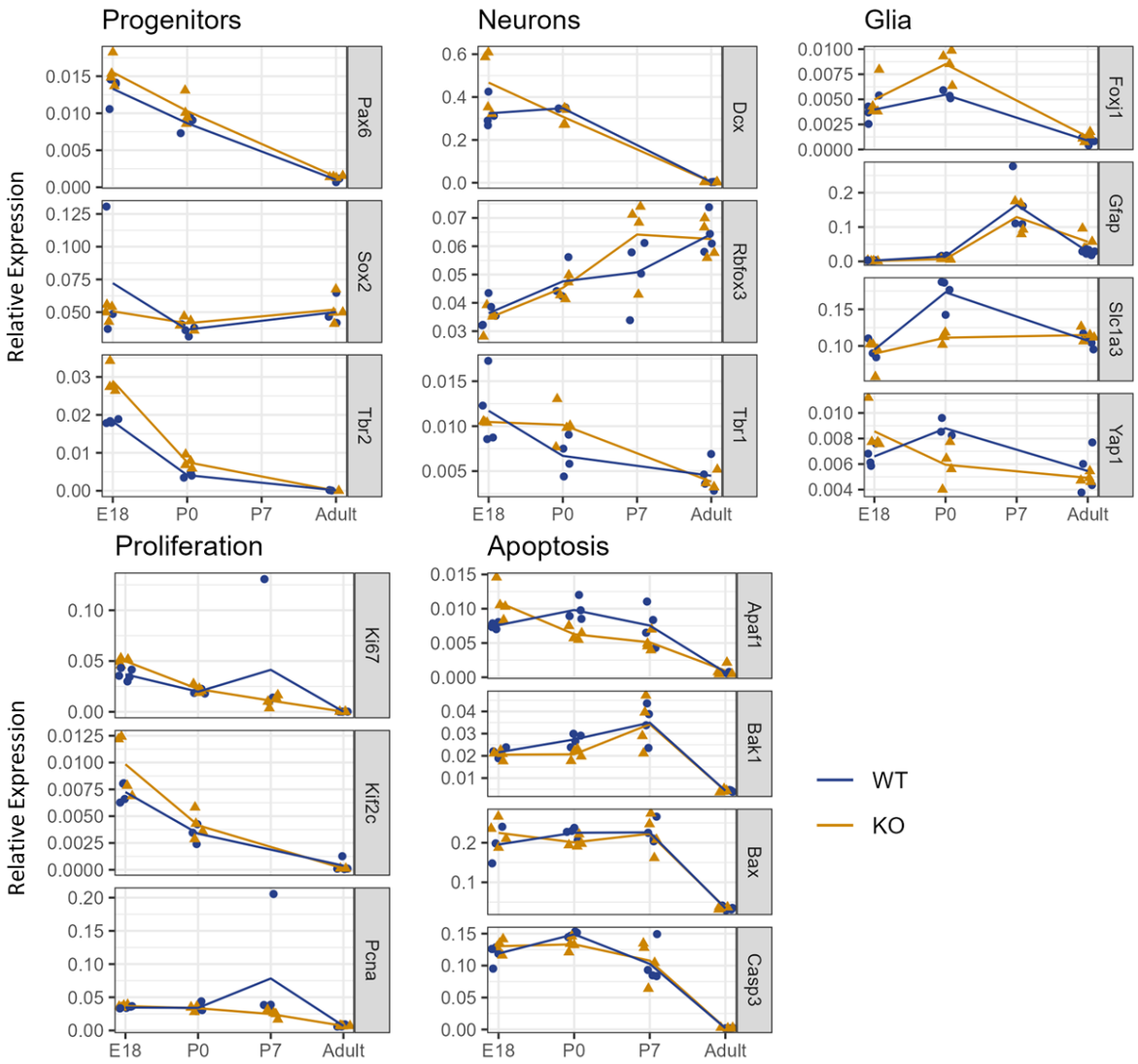

Figure 12: Gene Expression over Development, Arranged by Target Function

Expression of selected genes in WT and Mtss1 KO mice between E18 and adulthood as determined by RT-qPCR. Each expression is given in relation to the Gapdh expression in the same sample. Target genes are arranged by function: Progenitor cell marker, neuronal marker, glial marker, proliferation marker or apoptosis marker. n = 0 or 2-5 mice/genotype and age.

Concerning glial markers considered in Figure 12, Foxj1 (a marker of E1 ependymal cells and their precursors) rises in expression until P0, where highest expression and greatest differences between the genotypes are observed, before falling again. Gfap expression (expected in white matter astrocytes, reactive astrocytes and ependymal B1 cells) progresses similarly, with expression reaching its peak at P7, however.

Slc1a3/Glast (a marker of astrocytes and RGCs) also follows a pattern of increasing expression until P0 before a sharp decrease in expression in WT mice, with the expression KO mice staying relatively constant. The expression of Yap1, which is expressed in ependymal cells and astrocytes in WT mice is reminiscent of that of Slc1a3, however again, the course of expression is very different in KO mice, with an overall decrease of Yap1 mRNA, especially between E18 and P0.

Expression of proliferation-associated genes steadily decreases between E18 and adulthood, However, at P7, one likely outlier exhibits a peak in expression of Ki67 (a gene involved in both DNA replication and transcription) and Pcna (which plays roles in replication, cell-cycle control, DNA repair and chromatin assembly. Ki67 in general displays lower expression in E18 WT mice than in their KO counterparts. Expression of Kif2c, which regulates centromere attachment of the mitotic spindle, is also higher in KO mice at E18.

Apoptosis markers considered in Figure 12 are Casp3, Apaf1, Bak1 and Bax. Casp3 is an effector caspase of apoptosis, and thus a late player in the process of programmed cell death. Its roles include mediation of activity-dependent apoptosis of cortical neurons in early postnatal development. Apaf1 acts directly on Casp3. Bak1 and Bax are pro-apoptotic regulators of the intrinsic pathway, and thus act further upstream. Their roles in control of neural progenitor cells and CNS development have also been documented. Expression of all of these markers starts high at E18 and stays relatively constant until P0. However, a lower mean expression in all considered apoptosis markers can be observed in KO mice at P0. Until P7, these differences diminish, before expression of all apoptosis markers strongly decreases between P7 and adulthood.

4.2.2 Expression of mRNAs Specific for Neural Progenitor Cells and Glia in Perinatal Mice

Figure 13 documents E18- and P0- expression of selected genes used as markers for different pools of progenitor cells in neural development: Pax6 and Sox2, Foxj1, Tbr2, Yap1 and Gfap. Pax6 and Sox2 are both expected in RGCs. Their expression is slightly higher in Mtss1-deficient mice, with the exception of a likely outlier at E18, showing very high Sox2 expression in a WT mouse. Individually, none of the observed differences are statistically significant, however.

RGCs can differentiate into various different populations of cells, including E1 cells, IPCs and astrocytes. Interestingly, Foxj1, which is associated with developing and mature E1 ependymal cells shows no significantly differing expression at E18 and P0, although arguably, a tendency towards increased expression in KO mice at P0 is visible. Mtss1 KO mice also express significantly more Tbr2, which is a marker of neurogenic IPCs, at E18. At P0, differences in Tbr2-expression are not statistically significant, but as for Foxj1, values measured for KO and WT mice do not overlap. Expression of Gfap (expressed in white matter astrocytes, reactive astrocytes and ependymal B1 cells, but also expressed by RGCs, does not differ much between the genotypes at E18. At P0, Mtss1 KO mice express only half as much Gfap as their WT counterparts, a statistically significant difference. Expression of Yap1, which is also expressed in RGCs as well as ependymal cells and astrocytes, differs neither at E18 nor P0, although it may be noted that failure to detect statistically significant differences may be due to low availability of data. Reminiscent of Gfap expression, Slc1a3/Glast (a marker of astrocytes and RGCs) shows low expression at E18 for both genotypes, but a steep increase in Slc1a3-mRNA concentration between E18 and P0 happens only in WT mice, leading to statistically significant differences.

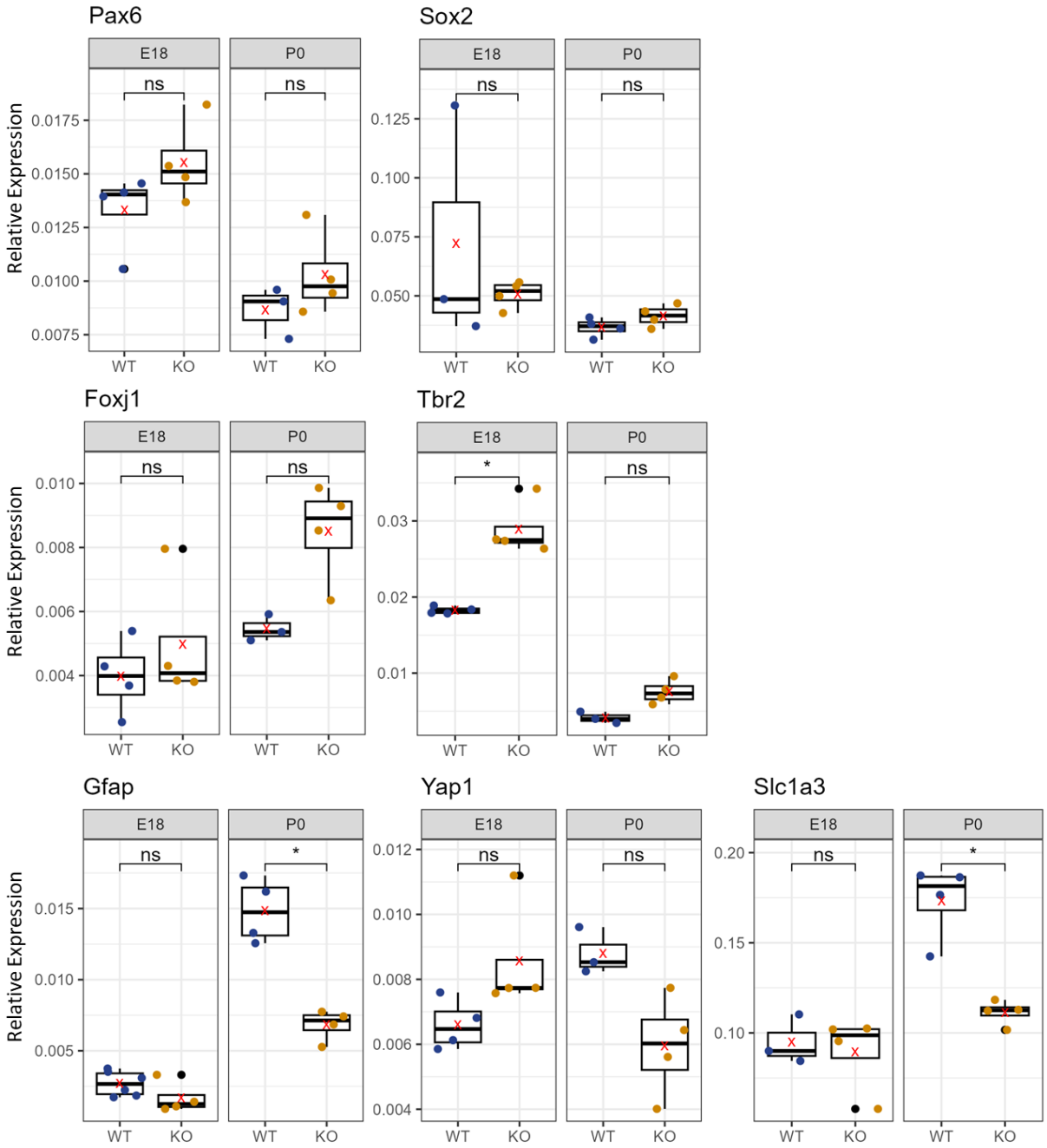

Figure 13: RNA Expression of Progenitor Cell and Glia Markers in Perinatal Development

*Expression of RGC markers Pax6, Sox2, E1-cell marker Foxj1, IPC marker Tbr2, combined RGC and glia markers Gfap, Yap1 and Slc1a3 as determined by RT-qPCR. Gfap and Slc1a3 show significantly lower expression in Mtss1 KO mice at P0. Significantly more Tbr2 is expressed in KO mice at E18. n = 3-5 mice/genotype and age. Each expression is given in relation to the Gapdh expression in the same sample. Red X marks the average value. Statistical significance determined by Wilcoxon-Mann-Whitney-Test: ns: p>0.05 ; *: p≤0.05 ; **: p≤0.01 ; ***: p≤0.001.*

Figure 14 shows the expression of markers with relevance to neuronal development (Dcx, Rbfox3 and TBR1). None of measured differences are statistically significant. However, expression of Dcx, which is associated with immature neurons, displays high variance in Mtss1 deficient mice at E18 than is seen in their WT counterparts.

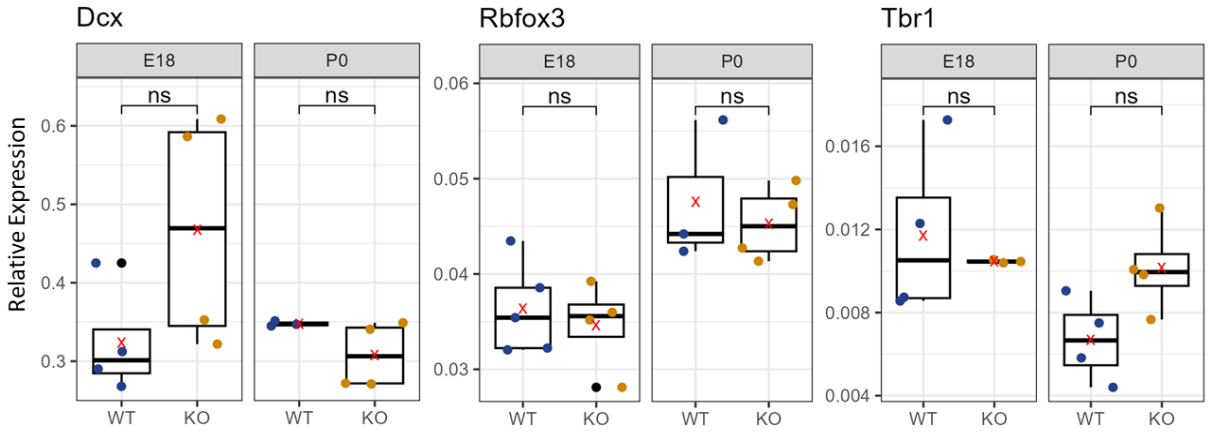

Figure 14: RNA Expression of Genes in Neuronal Differentiation in Perinatal Development

*Expression of Dcx, Rbfox3 and Tbr1 as determined by RT-qPCR. Expression does not differ significantly. n = 3-4 mice/genotype and age. Each expression is given in relation to the Gapdh expression in the same sample. Red X marks the average value. Statistical significance determined by Wilcoxon-Mann-Whitney-Test: ns: p>0.05 ; *: p≤0.05 ; **: p≤0.01 ; ***: p≤0.001.*

4.2.3 Expression of mRNAs Marking Proliferation- and Apoptosis in Perinatal Mice

For Mtss1 KO mice, Figure 15 displays expression of markers of proliferation and DNA replication, Ki67, Pcna, Kif2c, Top2a and Top2b on RNA level.

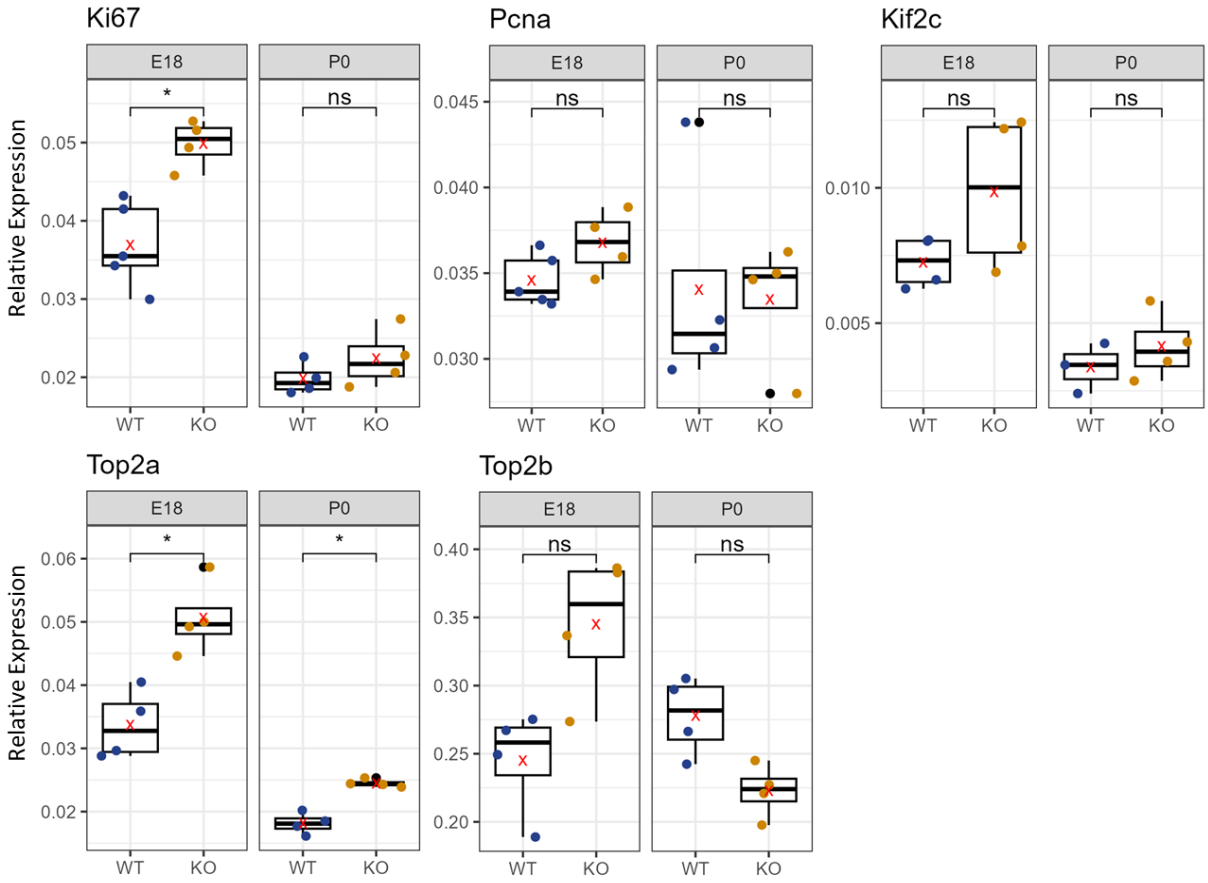

Figure 15: RNA Expression of Proliferation Markers in Perinatal Development

*Expression of proliferation markers (Ki67, Pcna, Kif2c Top2a, Top2b, Kif2c) as determined by RT-qPCR. Significantly more Ki67-, and Top2a-mRNA is expressed in Mtss1 KO mice at E18. For Top2a, expression is significantly higher in KO mice at P0 also. n = 3-5 mice/genotype and age. Each expression is given in relation to the Gapdh expression in the same sample. Red X marks the average value. Statistical significance determined Wilcoxon-Mann-Whitney-Test: ns: p>0.05 ; *: p≤0.05 ; **: p≤0.01 ; ***: p≤0.001.*

Except Top2a and Top2b, the roles of markers used here have been described in section 4.2.1. Topoisomerase-coding genes Top2a and Top2b play various roles, including chromosome condensation in mitosis for Top2a, DNA replication in the case of Top2a, as well as transcriptional regulation for both Top2a and Top2b. In neuronal development, Top2a plays a greater role in proliferation, while Top2b is more focused on transcriptional control, contributing to neurite targeting and laminar organisation of cell bodies in postmitotic neurons. They have also been shown to

form heterodimers with each other. At E18, Ki67 and Top2a are more strongly expressed in Mtss1 KO mice. A similar tendency in Top2b, Pcna and Kif2c might be suggested, but not statistically significant. At P0, only expression of Top2a shows significant differences between the genotypes, while the expression of Ki67, Pcna and Kif2c is similar in both genotypes. For Top2b, a trend for lower expression in Mtss1 KO mice is arguably present at P0.

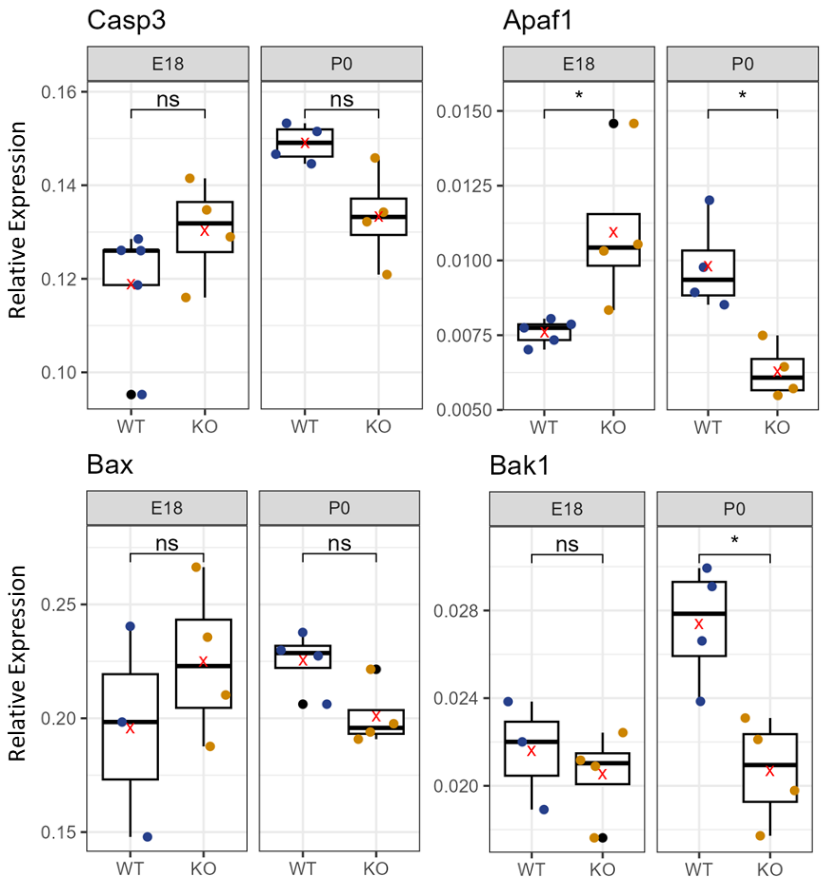

Figure 16: RNA Expression of Apoptosis Markers in Perinatal Development

*Expression of apoptosis markers (Casp3, Apaf1, Bak1, Bax) at E18 and P0 as determined by RT-qPCR. At E18, Apaf1 expression is significantly higher in KO mice. Expression of Apaf1 and Bak1 is significantly reduced in Mtss1 KO mice at P0. n = 3-5 mice/genotype and age. Each expression is given in relation to the Gapdh expression in the same sample. Red X marks the average value. Statistical significance determined by Wilcoxon-Mann-Whitney-Test: ns: p>0.05 ; *: p≤0.05 ; **: p≤0.01 ; ***: p≤0.001.*

Figure 16 documents expression of apoptosis players Casp3, Apaf1, Bax and Bak1. At E18, no significant differences were measured for any of the investigated apoptosis markers except Apaf1, the expression of which is stronger in KO mice. At P0, mRNAs of Apaf1 and Bak1 are present at significantly lower concentrations in Mtss1 KO mice.

4.2.4 mRNA-Expression in P7 Mice

Figure 17 shows the expression of Rbfox3 (marking for mature neurons) and Gfap (marking for reactive- and white matter astrocytes as well as B1 cells). Differences in expression are not statistically significant for either.

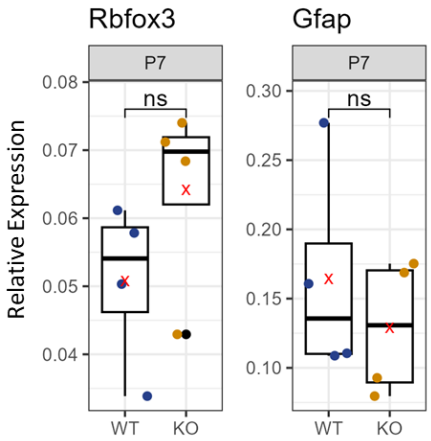

Figure 17: Gene Expression of Glia- and Neuron-Specific Markers in P7 Mice

*Expression of neuronal marker Rbfox3 and glia-associated gene Gfap in P7 mice as determined by RT-qPCR. No statistically significant differences in expression are found between WT and Mtss1 KO mice for either of the targeted mRNAs, however, Rbfox3 shows visibly higher expression on average. n = 3-4 mice/genotype. The expression is given in relation to Gapdh expression in the same sample. Red X marks the average value. Statistical significance determined by Wilcoxon-Mann-Whitney-Test: ns: p>0.05 ; *: p≤0.05 ; **: p≤0.01 ; ***: p≤0.001.*

Figure 18 shows the expression of proliferation marker Ki67 and apoptosis markers Casp3, Apaf1, Bak1 and Bax at P7. Expression of none of the considered genes differs significantly between the genotypes.

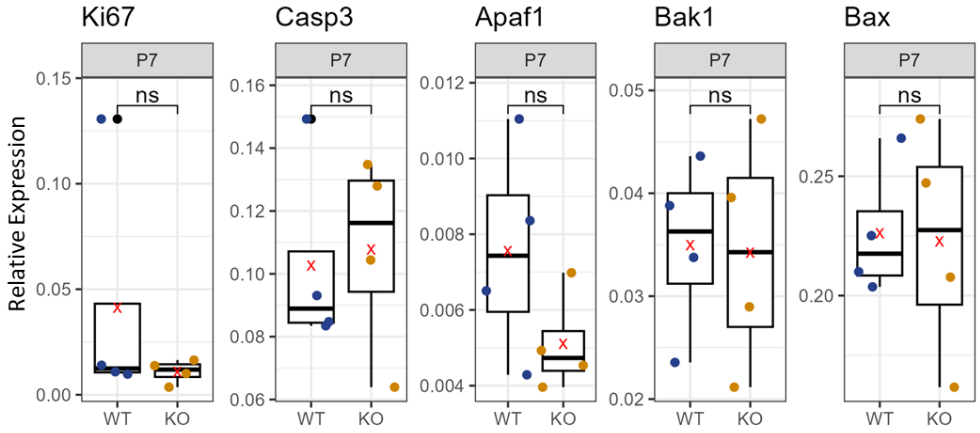

Figure 18: Gene Expression of Apoptosis- Proliferation-Specific Markers in P7 Mice

*Expression of proliferation marker Ki67 as well as apoptosis markers Casp3, Bak1 and Bax in P7 mice as determined by RT-qPCR. No statistically significant differences in expression are found between WT and Mtss1 KO mice for any of the targeted mRNAs. n = 3-4 mice/genotype. The expression is given in relation to Gapdh expression in the same sample. Red X marks the average value. Statistical significance determined by Wilcoxon-Mann-Whitney-Test: ns: p>0.05 ; *: p≤0.05 ; **: p≤0.01 ; ***: p≤0.001.*

4.2.5 Expression of mRNAs Specific for Neural Progenitor Cells, Neurons and Glia in Adult Mice

Figure 19 shows the relative levels of expression of RGC markers Sox2 and Pax6, of Dcx (expressed in migrating neurons), Rbfox3/NeuN (expressed in mature neurons) and Tbr1 (expressed in developing but postmitotic projection neurons, especially of layer V to VI. Figure 19 also displays expression of glia-associated genes Gfap (expressed in white matter astrocytes, reactive astrocytes and ependymal B1 cells), Yap1, which is expressed in ependymal cells and astrocytes, S100b (expressed in grey matter astrocytes and differentiating oligodendrocytes as well as E1 cells,

Slc1a3/Glast (a marker of astrocytes and RGCs) and Foxj1 (a marker of E1 ependymal cells and their precursors).

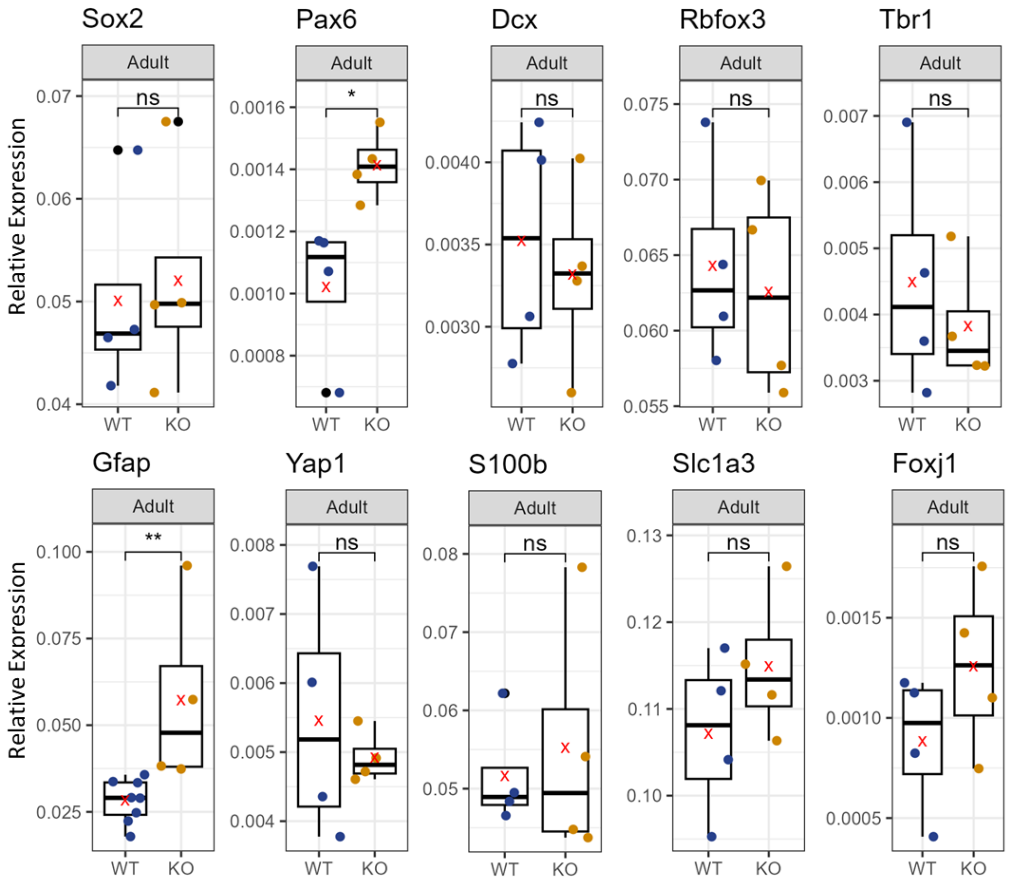

Figure 19: Gene Expression of Progenitor-, Glia- and Neuron-Specific Markers in Adult Mice

*Expression of RGC-associated genes SOX and Pax6, neuronal markers Dcx, Rbfox3 and Tbr1, glia-associated genes Gfap, Yap1, S100b, Slc1a3 and Foxj1 in adult mice as determined by RT-qPCR. Adult Mtss1-deficient mice express significantly more Pax6 and Gfap mRNA than WT mice. No statistically significant differences in expression are found between WT and Mtss1 KO mice for any other of the targeted mRNAs. n = 4 mice/genotype. The expression is given in relation to Gapdh expression in the same sample. Red X marks the average value. Statistical significance determined by Wilcoxon-Mann-Whitney-Test: ns: p>0.05 ; *: p≤0.05 ; **: p≤0.01 ; ***: p≤0.001.*

Adult Mtss1 KO mice express visibly more Pax6, which in the adult, does not mark RGCs, but is instead expressed in adult neural stem cells and a subset of neurons. The expression of Sox2 is similar in both genotypes. No statistically significant differences between WT and Mtss1 KO mice are present for any glia- or neuron-

associated marker, except Gfap. Here, expression in KO mice is found to be almost twofold that of WT mice.

4.2.6 Expression of mRNAs Marking Apoptosis and Proliferation in Adult Mice

Figure 20 shows expression of genes associated with apoptosis (Casp3, Apaf1, Bak1, Bax) and proliferation (Ki67, Kif2c, Pcna). No statistically significant difference is found between the genotypes for any of the mRNAs indicating proliferation and apoptosis.

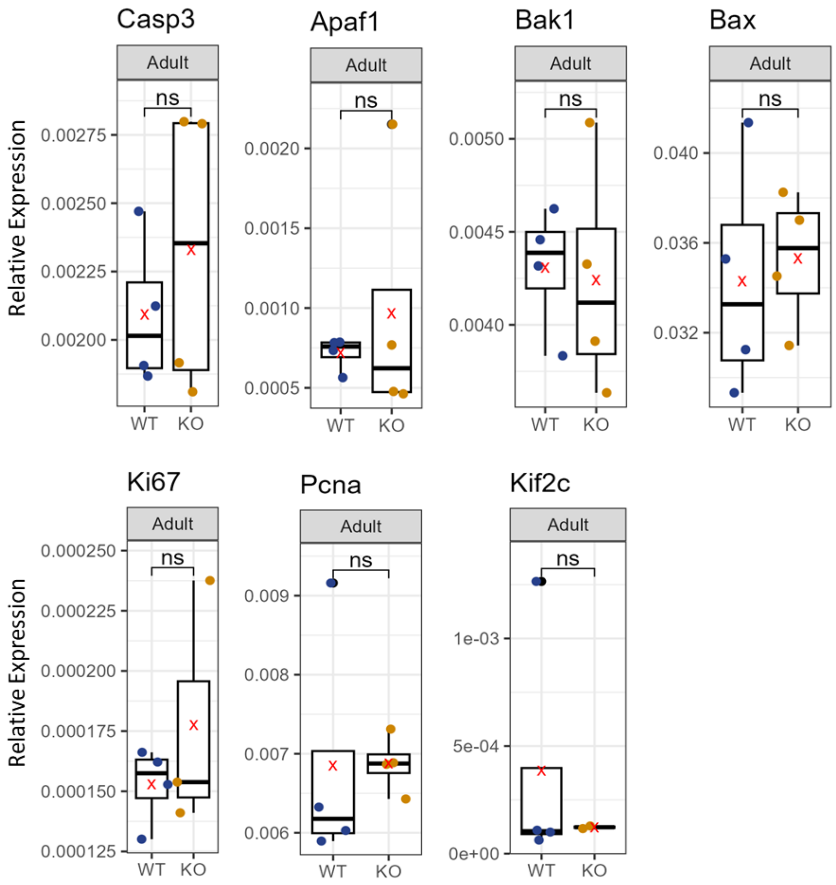

Figure 20: RNA Expression of Proliferation and Apoptosis Markers in Adult Mice

*Expression of apoptosis markers (Casp3, Apaf1, Bak1, Bax) and proliferation markers (Ki67, Pcna, Kif2c) in adult mice as determined by RT-qPCR. n = 2-4 mice/genotype. Each expression is given in relation to the Gapdh expression in the same sample. No significant differences are found for apoptosis- or proliferation markers in adult mice. Red X marks the average value. Statistical significance determined by Wilcoxon-Mann-Whitney-Test: ns: p>0.05 ; *: p≤0.05 ; **: p≤0.01 ; ***: p≤0.001.*

4.2.7 Egfr Expression

As later explained in section 5.1.5 of the discussion, the outcomes of these experiments raised the question if Egfr-Mtss1-interaction is relevant to the topic of neural development. Egfr is a gene that is present in various cell types in neural development, plays an important role in the switch of neurogenesis to gliogenesis and is a known interaction partner of Mtss1. The expression of Egfr greatly varies in E18 Mtss1 KO mice, but does not differ significantly from the expression in WT mice. At P0, KO mice have significantly lower expression of Egfr. In adult mice, Egfr expression does not differ significantly between the genotypes.

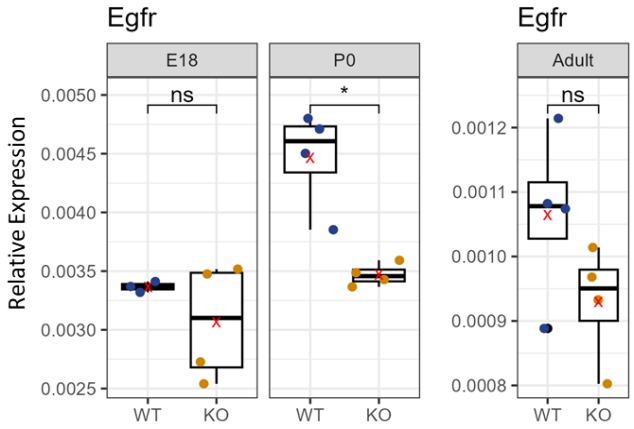

Figure 21: RNA Expression of Egfr

*Expression of Mtss1-interaction partner Egfr at E18, P0 and in adult mice as determined by RT-qPCR. n = 3-4 mice/genotype. Each expression is given in relation to the Gapdh expression in the same sample. At P0, KO mice express significantly less Egfr. The expression of Egfr does not differ between the genotypes at E18 or in adult mice. Red X marks the average value. Statistical significance determined by Wilcoxon-Mann-Whitney-Test: ns: p>0.05 ; *: p≤0.05 ; **: p≤0.01 ; ***: p≤0.001.*

4.3 Altered Cell Distribution in VZ and SVZ of Newborn Mtss1 KO Mice

RT-qPCR findings presented in chapter 4.2 suggest increased expression of proliferation markers in posterior telencephalon of Mtss1 deficient mice at E18 and P0. They also suggest increased expression of intermediate progenitor marker Tbr2. This prompts several questions:

1. Are these changes limited to mRNA expression, or do they go along with protein level expression?
2. Which anatomical regions of the brain exhibit these differences?
3. Within these regions, are the differences to be attributed to expression levels per cell or to altered cell numbers?

To address these questions, the numbers of localisations of cells expressing selected markers were analysed by immunofluorescence staining of frontal sections of P0 mice.

4.3.1 Increased Numbers of Proliferating Cells in Ventricle Roof VZ/SVZ at P0

As described in section 3.6.5, brains were stained for mitotic marker Ki67, and evaluated. Numbers of immunopositive cells were related both to the length of the ventricular surface visible in the respective section, and to the section area. This approach was used to account for the variable depth of the VZ and SVZ, even in closely neighbouring areas. The outcomes are show in Figure 22. As indicated, the VZ and SVZ at the roof of the lateral ventricle of Mtss1 KO mice contain significantly more $Ki67^{+}$ cells per length of ventricular surface as well as per area of evaluated germinal region, than is the case in WT mice. Data obtained from lateral germinal regions are highly variable, and formal testing does not yield statistically significant differences between the genotypes.

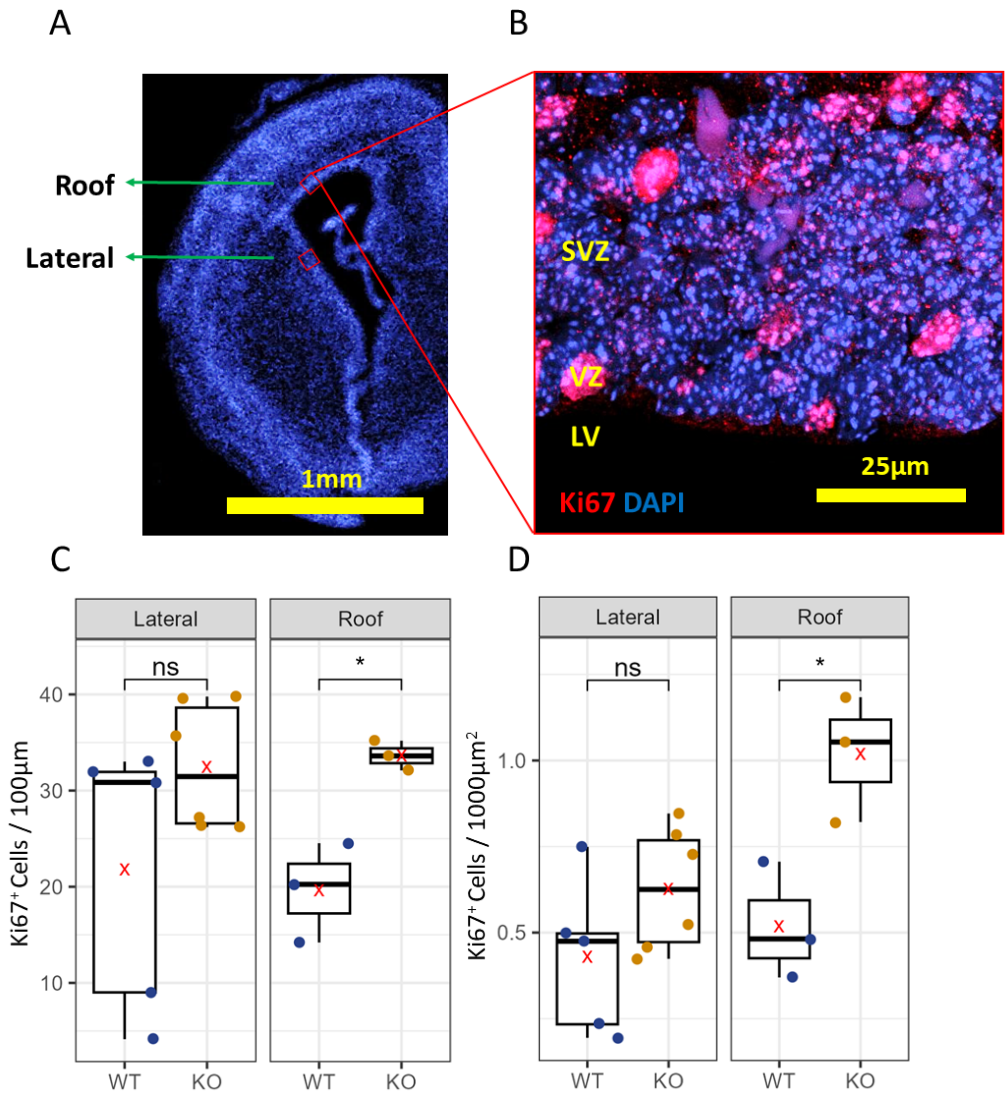

Figure 22: Relative Number of Ki67+ Cells in VZ and SVZ

A: *Evaluated regions marked in P0 frontal section (inset).* ***B:*** *Example roof region of VZ and SVZ stained with DAPI and anti-Ki67 antibody. Lateral ventricle (LV), VZ and SVZ marked.* ***C:*** *Ki67-Expressing Cells per 100µm width of ventricular surface.* ***D:*** *Ki67-Expressing cells per 1000µm² area of evaluation field in lateral and ventricle roof germinal zones. Cell numbers were determined by manual counting and divided by evaluated area or width, respectively. Thickness of evaluated paraffin sections = 8µm. n = 3 mice/genotype for roof, n = 3-4 mice/genotype and 1-2 Positions for lateral VZ/SVZ. Red X marks the average value. Statistical significance determined by Welch's t-test: ns: p>0.05 ; *: p≤0.05 ; **: p≤0.01 ; ***: p≤0.001.*

4.3.2 Increased Numbers and Widened Distribution of Tbr2$^+$ Cells as well as Shifted Distribution of Sox2$^+$ and Pax6$^+$ Cells in the VZ/SVZ of the Ventricular Roof of P0 Mtss1-deficient Mice

To inquire into Pax6-, Sox2- and Tbr2 expression in ventricular- and subventricular zone, profile plots were generated from immunofluorescence stainings. Briefly, for each field, a rectangular selection spanning from ventricular surface through VZ and SVZ into cerebral cortex was defined manually and staining intensity recorded for each pixel row from one end to the other. Maximum staining intensity was adjusted to the value of 1. Figure 24 includes sample evaluations for this method. Averaging all profile plots per genotype/staining combination yields the summary profile plots displayed in Figure 23. As to be seen, for every measured staining, intensity peaks more proximal to the lateral ventricle (0µm) in P0 WT mice than in P0 KO mice. DAPI, staining every nucleus, shows lower staining intensity close to the lateral ventricle in KO mice, but higher staining intensity from 40µm to 100µm into the tissue. Pax6 and Sox2, markers for apical RGCs, display a similar pattern of staining intensity as DAPI, with intensity in KO mice overtaking that in WT mice from 20µm to 100µm. Tbr2, a marker of neurogenic IPCs, shows a clearly broadened peak of expression in KO mice, but similar staining intensity for WT and KO mice starting at 50µm into the tissue. Figure 24 also shows a combined β-gal staining for Mtss1-promoter activity and DAB-immunohistochemical staining for Tbr2 in a P0 Mouse heterozygous for Mtss1. Although exact localisation to individual cells is difficult to determine with β-gal stainings, the staining clearly shows activity of the Mtss1-promoter in the VZ and SVZ. Notably, it is present in both the more basal regions of the SVZ where Tbr2-expression is strong and the more apical regions, where Tbr2-expression is weaker.

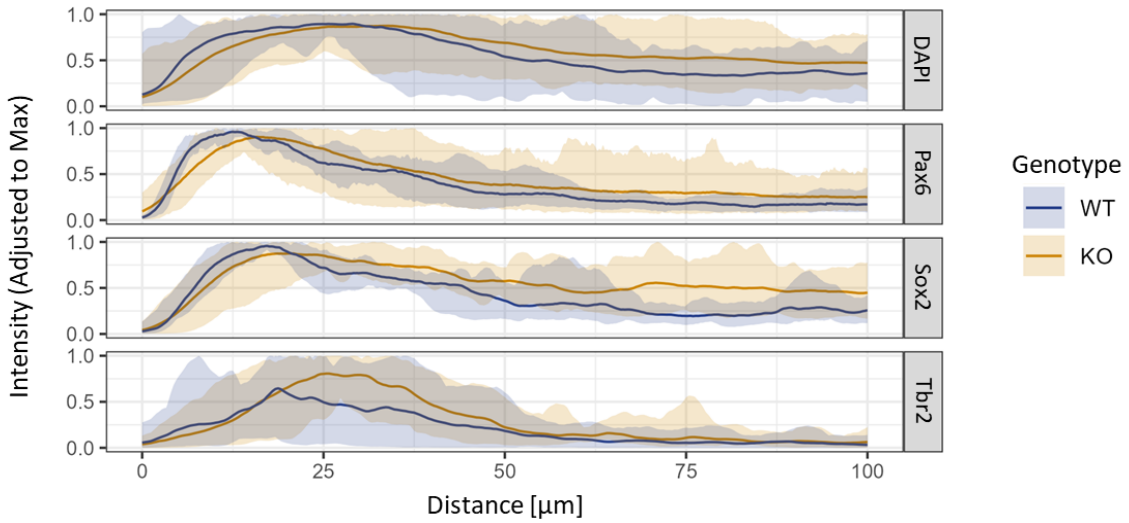

Figure 23: Summary Profile Plots of DAPI, Pax6, Sox2 and Tbr2 in the Ventricle Roof Germinal Zones at P0 by Genotype

Summary profile plots were prepared by calculating average, minimum and maximum staining intensity by genotype and staining (DAPI, Pax6, Sox2, Tbr2) from all individual evaluation fields for each distance increment. See Figure 24 for sample evaluations of individual evaluation fields. Left (0µm): Lateral ventricle. Right: 100µm towards meningeal surface. Thick line: Average intensity. Transparent Ribbon: Range from minimal to maximal measured intensity. Pax6: n = 3-8 mice/genotype, 1-4 fields/mouse. Sox2: n = 2 mice/genotype, 2-6 fields/mouse. Tbr2: n = 3-5 mice/genotype, 1-3 fields/mouse. DAPI: n = 4-8 mice/genotype, 1-7 fields/mouse.

The area under the curve of adjusted intensity versus distance of ventricular lumen to 100µm into the tissue for each individual field is summarised in the left of each panel of Figure 24. AuC of Sox2, Tbr2 and DAPI signal are significantly greater in P0 Mtss1 KO mice. The measured differences in Pax6 signal are not statistically significant.

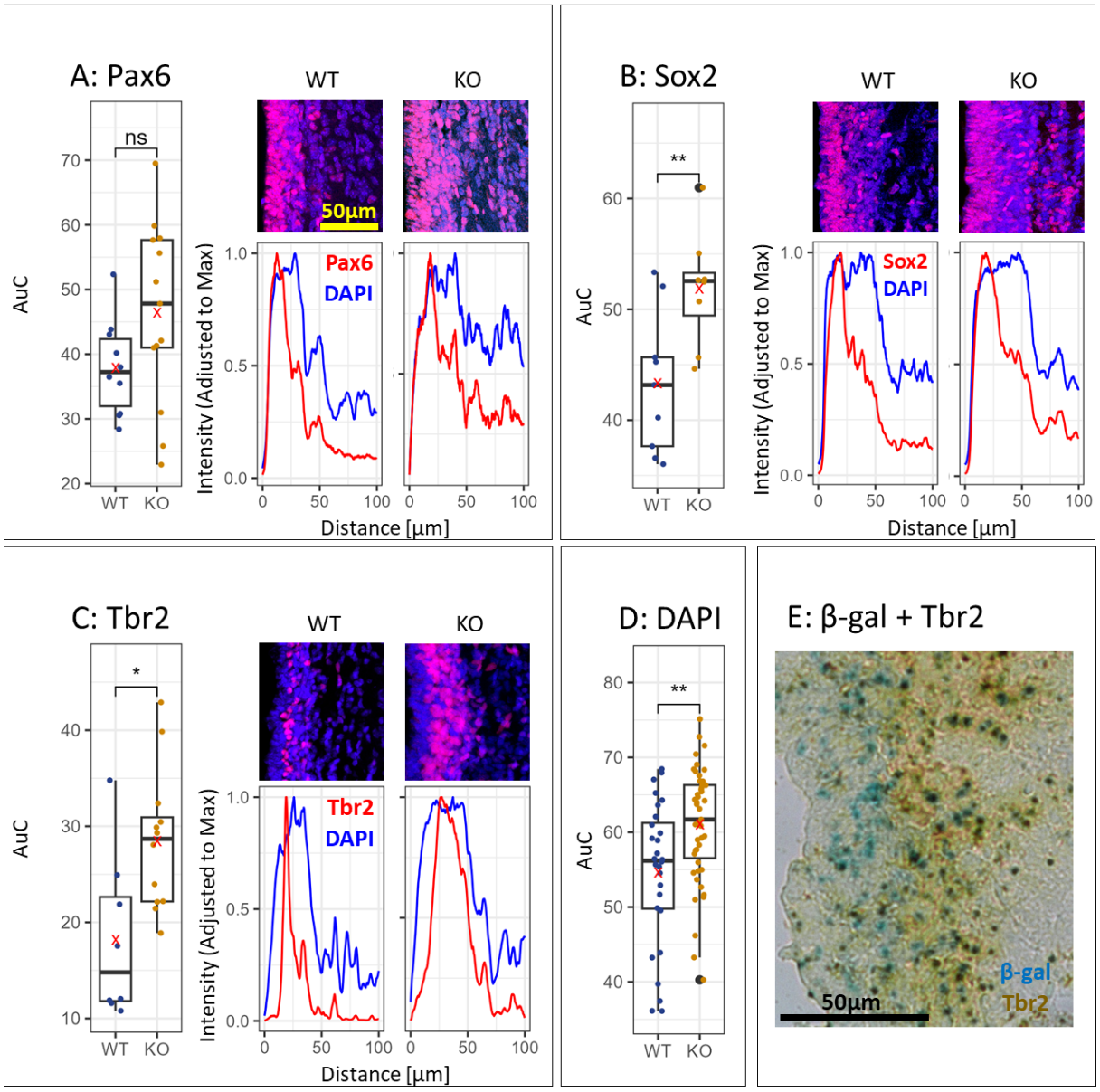

Figure 24: Distribution of Progenitor Cells in the Ventricle Roof Germinal Zones at P0

A: *AuC of profile plot for Pax6 (left) and corresponding sample evaluation (right). Profile plot shows adjusted staining intensity (here Pax6) vs distance. n = 3-8 mice/genotype, 1-4 fields/mouse. Sample evaluation of image to yield AuC: Immunofluorescence stainings of ventricle roof (top) were measured from left to right. The outcome (bottom) was used to calculate area under the curve from ventricular surface (0µm) to 100µm into the tissue for Pax6, Sox2, Tbr2 or DAPI signal, reflecting the respective expression in VZ and SVZ.* ***B:*** *AuC of profile plot for Sox2 and corresponding sample evaluation. n = 2 mice/genotype, 2-6 fields/mouse.* ***C:*** *AuC of profile plot for Tbr2 and corresponding sample evaluation. n = 3-5 mice/genotype, 1-3 fields/mouse.* ***D:*** *AuC of profile plot for DAPI. n = 4-8 mice/genotype, 1-7 fields/mouse. Red X marks the average value. Statistical significance determined by Welch's t-test: ns: p>0.05 ; *: p≤0.05 ; **: p≤0.01 ; ***: p≤0.001.* ***E:*** *Combined β-Gal staining for Mtss1-promoter activity (blue) and DAB immunohistochemical staining for Tbr2 (brown) in a P0 Mouse heterozygous for Mtss1.*

4.4 The Cell Type Composition of Ependyma is Altered in Mtss1 Deficient Mice

The increased expression and occurrence of $Tbr2^+$ cells in sections 4.2.2 and 4.3.2 imply increased neurogenic IPC numbers in development as a result of Mtss1 KO. The possibly altered expression of Foxj1 and Yap1, and definite upregulation of Gfap and Pax6 may also imply an altered development of E1 ependymal cells and B1 adult stem cells, which share a common ancestry. In order to investigate if adult neural progenitor cell numbers are changed, ependymal B1 cells were examined. To determine the numbers of B1 cells in adult mice, lateral ventricle wholemount preparations were stained. To delineate cell borders, ZO1 was used, while Centriolin was used to mark cilia. B1 cells are characterised by the presence of only two cilia and their small area of contact to the ventricular lumen, as to be seen in Figure 25 B, and could be counted manually. Per animal, two fields of 295µm x 295µm were considered. Figure 25 A indicates that the mean number of B1 cells does not differ significantly between WT and KO mice. However, it appears that the variability of B1 cell numbers is smaller in KO mice than in WT mice, possibly indicating decreased regional variability in KO mice.

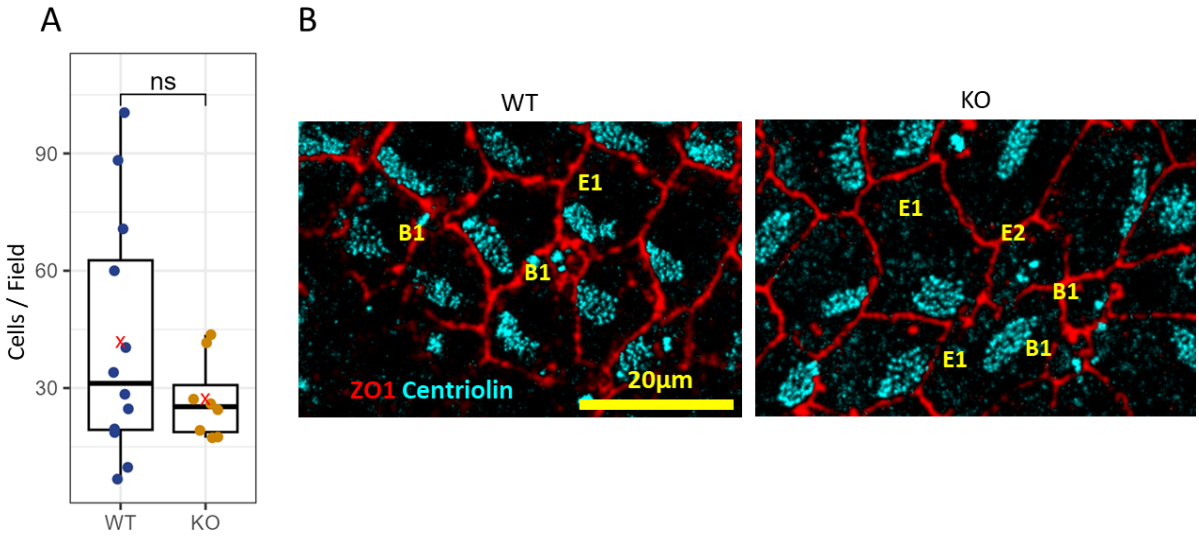

Figure 25: Number of B1 Cells per Field

A: *Manually counted B1 cells per field (295µm x 295µm).* ***B:*** *Example determination of ependymal cell types in a ventricle wholemount immunofluorescence staining for ZO1 and Centriolin. n = 4-7 mice/genotype, 2 fields / mouse. Red X marks the average value. Statistical significance determined Wilcoxon-Mann-Whitney-Test: ns: p>0.05 ; *: p≤0.05 ; **: p≤0.01 ; ***: p≤0.001.*

4.5 The Polarity of E1 Cells in Adult Mtss1 KO Mice is Marginally Altered

4.5.1 Rotational Polarity of E1 Cells in Adult Mice

Given the association of Mtss1 with basal bodies observed in cultured cells (Bershteyn *et al,* 2010), a role of Mtss1 for the function of E1 cell cilia was suspected. Furthermore, because Mtss1 is known to stabilise cell-cell contacts and is involved in cytoskeleton- and membrane dynamics (Matskova *et al,* 2024), a role of Mtss1 in PCP was also conceivable. Cilium orientation and position are hallmarks of ependymal E1 cell morphology and controlled by the PCP pathways. Immunofluorescence stainings of lateral ventricle wholemounts were used to

evaluate the rotational and translational polarity of the ependyma. To determine rotational polarity of ependymal cells, basal body and basal foot elements Centriolin and γ-Tubulin were stained and their positions recorded as indicated in Figure 26 A. The overall distribution of angles adjusted to the mean angle within each image is displayed in Figure 26 B. The angles between a reference direction and these points were used to calculate the angular variance. A high angular variance indicates disruption of rotational polarity. Per animal, 50 fields were considered: 25 in anterior parts of the ventricle wholemount, 25 in the posterior part. First, angular variance within each field (regional angular variance) was calculated. The outcomes were averaged per sample area, and are displayed in Figure 26 C. Secondly, the mean angle within each field was calculated, and the angular variance between these mean angles was determined (interregional angular variance, displayed in Figure 26 D). As illustrated, angular variance of the measured angles between γ-Tubulin and Centriolin are not significantly different between genotypes. Another measure of angular statistics, the angular deviation, was calculated in the same manner as angular deviation, but differences are also insignificant ($p = 0.49$ for regional angular deviation, $p = 0.85$ for interregional angular deviation, as determined by Wilcoxon-Mann-Whitney test.)

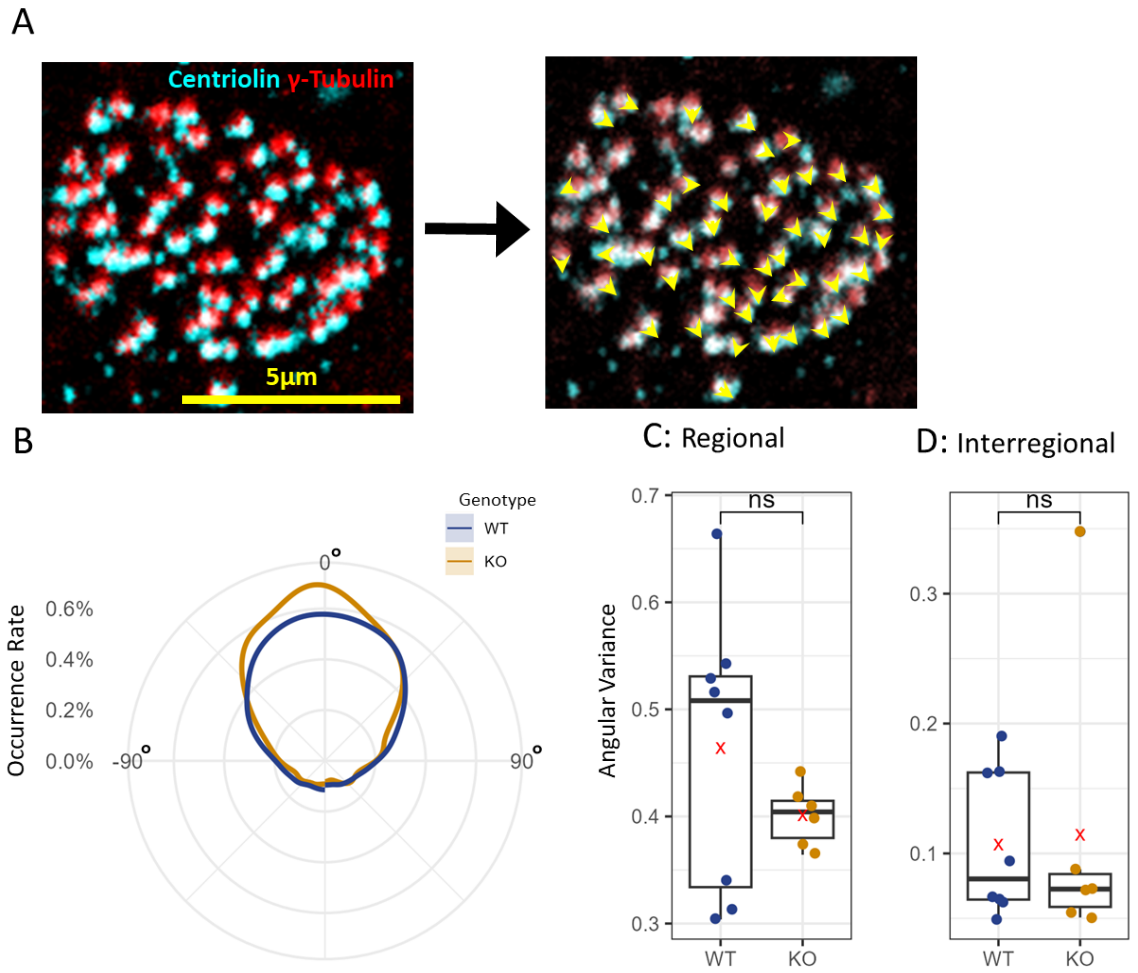

Figure 26: Rotational Polarity of Individual Cilia on E1 Ependymal Cells

A: *Example evaluation of basal body angles in types in a ventricle wholemount immunofluorescence staining for γ-Tubulin and Centriolin. Angles between γ-Tubulin and Centriolin signals marked.* ***B:*** *Density plot of all measured angles, adjusted to the mean angle of each image (0°).* ***C:*** *Mean angular variance of basal body directions within evaluation fields.* ***D:*** *Angular variance of mean basal body directions between evaluation fields. n = 6583 - 12513 cilia, 3-4 mice/genotype, 2 sample areas/mouse. Red X marks the average value. Statistical significance determined by Wilcoxon-Mann-Whitney test: ns: p>0.05 ; *: p≤0.05 ; **: p≤0.01 ; ***: p≤0.001.*

4.5.2 Translational Polarity of Ependymal E1 Cells in in Adult Mice

To investigate translational polarity of E1 cells, the positions of the cell centre and the centre of the basal body patch were recorded as outlined in Figure 27 A. Per animal, 50 fields were considered: 25 in anterior parts of the ventricle wholemount, 25 in the posterior part. The average distance between cell centre and basal body patch was calculated separately for the anterior and posterior parts of the ventricle wholemounts, and are displayed in Figure 27 B. The angles between the same points were also measured, and adjusted to the mean angle within each image. Their occurrence rate is shown in Figure 27 C. The same angles were used to calculate the angular variance. First, angular variance within each field (regional angular variance) was calculated. The outcomes were averaged per sample area, and are displayed in Figure 27 D. Secondly, the mean angle within each field was calculated, and the angular variance between these mean angles was determined (interregional angular variance, displayed in Figure 27 E). See Figure 30 in the appendix for an example map of angular data from one image. Differences between WT and KO mice regarding distance between these points are insignificant. Angular variances are also not significantly different between genotypes. Angular deviation was calculated in the same manner as angular deviation, and differences are also insignificant ($p = 0.059$ for regional- $p = 0.7$ for interregional angular deviation, as determined by Wilcoxon-Mann-Whitney test).

However, extreme cases of mismatching translational polarity of neighbouring cells are significantly more common in KO mice: Percentage of neighbouring cells strongly mismatched translational polarity was determined as explained in Figure 8 of the methods chapter. The outcome of this is displayed in Figure 28.

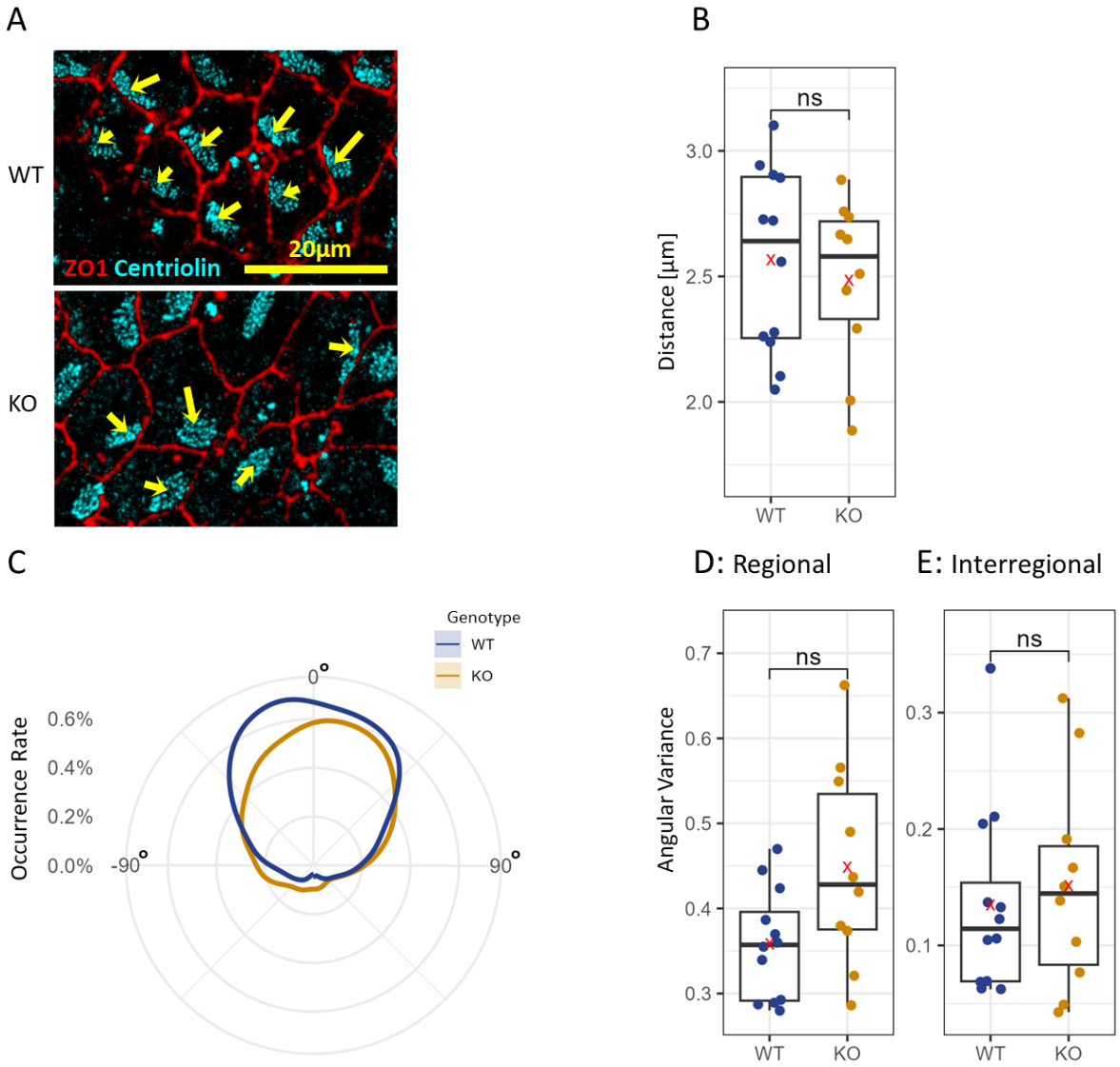

Figure 27: Translational Polarity of E1 Ependymal Cells

A: *Example evaluation of distance and angles between cell centres and basal body patches types in a ventricle wholemount immunofluorescence staining for ZO1 and Centriolin.* ***B:*** *Mean distance between cell centre and centre of basal body patch.* ***C:*** *Density plot of all measured angles, adjusted to the mean angle of each image (0°).* ***D:*** *Mean angular variance of angles between the cell centre and centre of basal body patch within evaluation fields.* ***E:*** *Angular variance of mean angles between the cell centre and centre of basal body patch between evaluation fields. n = 4934 – 5758 cells, 5-6 mice/genotype, 2 sample areas/mouse. Red X marks the average value. Statistical significance determined by Wilcoxon-Mann-Whitney test: ns: p>0.05 ; *: p≤0.05 ; **: p≤0.01 ; ***: p≤0.001.*

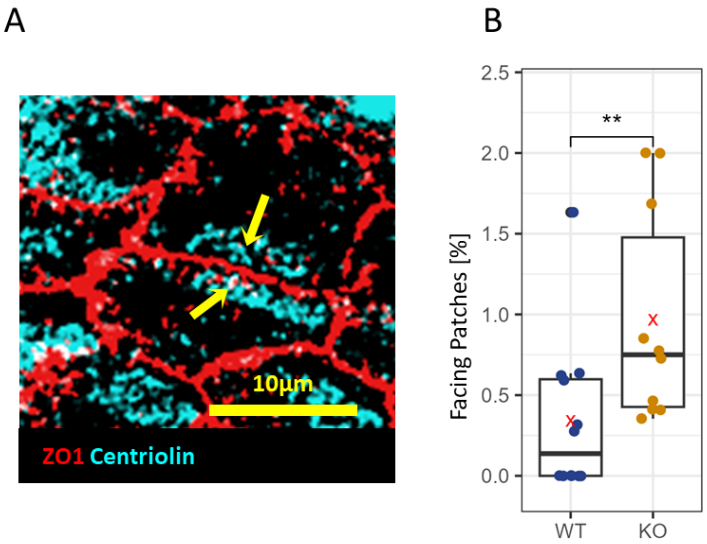

Figure 28: Count of Basal Body Patches Facing Each Other

A: *Example of two cells defined at facing each other with regard to translational polarity.* ***B:*** *Percentage of neighbouring cells facing each other with regard to translational polarity = 4934 – 5758 cells, 5-6 mice/genotype, 2 sample areas/mouse. Red X marks the average value. Statistical significance determined by Wilcoxon-Mann-Whitney test: ns: p>0.05 ; *: p≤0.05 ; **: p≤0.01 ; ***: p≤0.001.*

5 Discussion

While Mtss1 has long been investigated in the context of cancer development, its role in the healthy individual is beginning to be unravelled now. However, fundamental questions remain in how the cellular roles of Mtss1 translate to the tissue and organ levels, especially in the heart, bone marrow, and CNS. This project sought to gain information on whether cells and processes in the germinal zones of the developing telencephalon are influenced by Mtss1 deficiency, and if that influence might be responsible for the Mtss1 KO-associated phenotype of the brain. As stated in the introduction, the questions that were to be answered are whether Mtss1 impacts proliferation in the telencephalon, which cell types and developmental time points this pertains to, and whether the underlying mechanism is a disturbance of PCP.

5.1 Interpretation

5.1.1 The Composition of the Telencephalon in Adult Mtss1 KO Mice is Altered

The data presented here confirm that the distance between ependyma and meninges of adult Mtss1-deficient mice is shorter than that of WT mice, indicating a reduced overall volume of grey matter and / or white matter and adult VZ/SVZ in the posterior telencephalon. Going along with the reduced tissue volume are decreased numbers of neurons, and of cells overall, as determined by Nissl staining and by measuring DNA concentration in biopsy lysates.

According to RT-qPCR analyses of caudal parts of the telencephalon, the expression of genes associated with neuronal and some glial cells is mostly unaltered by Mtss1 KO in adult mice. However, Pax6 expression is enhanced in Mtss1 KO mice. Owing

to their expression of Pax6 (Duan *et al,* 2013), this could be explained by higher proportions of adult neural stem cells being present. While counts of B1 neural stem cells per area of ependyma are normal in Mtss1 KO mice, the explanation might still hold true: The thinner cerebral cortex and larger ventricular volume of KO mice might overall lead to an overrepresentation of ependymal material in the gathered qPCR samples. Alternatively, as Pax6 is also expressed in a subset of mature neurons (Duan *et al,* 2013), enhanced Pax6 expression might result from shifts of neuronal populations. Finally, the increased expression of Pax6 might also raise the suspicion whether immature cortical cells are retained in adult Mtss1 KO mice. Further experiments, possibly employing immunofluorescence stainings or cell sorting might clarify which cells are responsible for the increased Pax6 expression in adult KO mice.

Mtss1 KO mice also show a much higher expression of Gfap. As Gfap is expressed in B1 ependymal cells, this may also point towards an overrepresentation of ependymal material in brain samples of adult KO mice owing to their increased ventricular volume, as does the small trend of enhanced expression of Foxj1 (expressed in E1 ependymal cells).

However, also consistent with enhanced Gfap expression is a trend towards higher expression of glial markers in general (Slc1a3, S100b and Foxj1). While differential expression of these genes cannot be proven without analysis of many more animals, the available data are also not a proof of absence of differential expression. The high variability of the expression data of Slc1a3, S100b and Gfap may allow the interpretation that Mtss1 KO mice have a larger complement of glial cells than WT mice in their posterior telencephalon. More specifically, since Gfap is strongly expressed by reactive astrocytes, the data could also indicate astrogliosis (Sibilia *et*

al, 1998). However, the expression of genes associated with apoptosis and proliferation is not changed by Mtss1 KO in adult mice. As reactive astrocytes tend to proliferate, this does not lend support to the speculation of ongoing astrogliosis being the reason for increased Gfap expression (Sibilia *et al,* 1998). It might however be consistent with the interpretation of glial scars having been formed in the past. Lastly, as white matter astrocytes express more Gfap than grey matter astrocytes, enhanced Gfap expression in Mtss1 KO mice might instead specifically indicate a larger proportion of white matter astrocytes to be present in KO mice than in their WT counterparts. This interpretation implies that cortical grey matter and its underlying white matter are differently affected by Mtss1 deficiency. The present observation that in Mtss1 KO mice, fewer cells identified by Nissl staining are found, would be consistent with either interpretation, as neurons are expected to be stained well, and astrocytes poorly by Nissl staining (Kádár *et al,* 2009). Moreover, the previously mentioned reduced distance from ependyma to meninges also coincides with an increase of apparent tissue stiffness of the investigated areas of the telencephalon of Mtss1-KO mouse. Differences in stiffness could be interpreted as being indicative of shifted proportions of grey and white matter due to known differences in their respective mechanical properties. According to Christ *et al* (2010) and Weickenmeier *et al (*2016), cerebral white matter is stiffer than cerebral grey matter and cerebellar white matter, while cerebellar grey matter is stiffer than cerebellar white matter. On the other hand, standardised major axis estimation of my data suggests, that the measured differences in stiffness could be attributed to differences in distance, regardless of genotype. Measuring mechanical properties with other methods might give more insight.

Regardless, with little or no changes of the rates of proliferation and apoptosis present in the posterior telencephalon of adult Mtss1-deficient mice, changes to cell type composition are likely to originate earlier in development.

5.1.2 Proliferation and Apoptosis in the Brains of Perinatal Mtss1 KO Mice is Altered

RT-qPCR analyses of caudal parts of the telencephalon of perinatal and late embryonic mice indicate changes of proliferation and apoptosis as a consequence of Mtss1-deficiency: In comparison to WT mice, at E18, proliferation markers Ki67 and Top2a are upregulated significantly on mRNA level in the brain samples of Mtss1 KO mice. With exception of the expression of Top2a, these changes did not persist until after birth. Pcna and Top2b did not show significant differences in expression. However, Pcna has previously been shown to have a relatively long half-live within tissue and to be a less specific marker of proliferation than Ki67 (Bologna-Molina *et al,* 2013). Similar may be said about Top2b, as it plays important roles in postmitotic neurons (Nevin *et al,* 2011). Further data on proliferation were obtained by immunofluorescence stainings of P0 brains, which allows comparison of proliferative activity in discrete regions of the forebrain. The expression of Ki67 is found in significantly more cells of the ventricular roof VZ and SVZ of perinatal Mtss1 deficient mice. The roof of the lateral ventricle, in contrast to its lateral walls, represents germinal zones producing predominantly projection neurons and astrocytes that will later take up function in the same region (Molyneaux *et al,* 2007), (Stouffer *et al,* 2016), (Kandel, Schwartz, Jessell, Siegelbaum, Hudspeth, 2013), (Magavi *et al,* 2012). These observations suggest increased proliferation rates in the zones

producing these cells. This interpretation is consistent with profile plots of DAPI signal (and thus overall cell density) in ventricular roof SVZ and VZ at P0, which show a significant, albeit slight increase in cell numbers in the germinal zones in Mtss1 KO mice as compared to WT mice. Instead, the higher numbers of $Ki67^+$ cells observed in Mtss1 KO mice might also be indicative of a slowing down of the cell cycle (especially during mitosis). Indeed, Pilaz *et al* (2016), studying a phenotype of prolonged prometaphase in RGCs, observed such an increase in numbers of $Ki67^+$ cells, alongside profound changes in cell fate and eventual reduction of the neuronal pool. Of course, if RGCs or IPCs were mitotically delayed, not more, but fewer cells would be produced per time, and possibly overall, which would be consistent with the findings of reduced cell numbers made in the cerebral cortex of adult Mtss1 KO mice.
At E18, mRNA-expression of apoptosis marker Apaf1 is enhanced in caudal telencephalon of Mtss1 KO mice, as tested by RT-qPCR. In contrast, at P0, expression of apoptosis markers Apaf1 and Bak1 is significantly weaker in KO mice, and all other tested apoptosis markers show a similar, albeit insignificant trend.
While it seems clear that proliferation and apoptosis in the germinal zones or neural development are affected by Mtss1 KO, further experiments are needed to determine how exactly. Bromodeoxyuridine (BrdU) labelling could serve to test actual rate of proliferation as well as investigate the long-term fate of cells regarding apoptotic frequency over long stretches of time.

5.1.3 Altered Cell Type Populations in the Posterior Telencephalon of P0 Mtss1 KO Mice

Assuming altered proliferation at E18 and P0 and decreased apoptosis at P0, the question arose, whether numbers of any specific cell population are changed in

developing Mtss1 KO mice. RT-qPCR of E18, P0, P7 and adult caudal telencephalon samples point at several cell populations to be affected in different ways, as summarised in Table 22:

Table 22: Overview of Cell Markers and their Expression in Mtss1 KO, based on mRNA Expression and Profile Plots of Immunofluorescence Stainings

Gene	Role	E18	P0	P7	Adult
Pax6	RGC marker, but in the adult expressed by both VZ-SVZ adult neural progenitor cells and a subset of neurons	-	-	-	↗
Sox2	Marker of RGCs, glial precursors, adult neural stem cells, proliferating astrocytes, ependymal cells	-	↗	-	-
Tbr2	Marker of neurogenic IPCs	↗	↗	-	-
Gfap	Marker of white matter astrocytes, reactive astrocytes and ependymal B1 cells	-	↘	-	↗
Slc1a3	Marker of astrocytes and RGCs	-	↘	-	-
Ki67	DNA replication and transcription	↗	↗	-	-
Top2a	Topoisomerase-coding gene, chromosome condensation in mitosis, transcriptional regulation, forms heterodimers with Top2b, in neuronal development mostly expressed in proliferative cells, but not mature neurons	↗	↗	-	-
Apaf1	Apoptosis marker, acts directly on Casp3	↗	↘	-	-
Bak1	Pro-apoptotic regulator of the intrinsic pathway upstream of Apaf1, roles in control of neural progenitor cells and CNS development	-	↘	-	-
Egfr	Present in various cell types in neural development, switch of neurogenesis to gliogenesis, interaction partner of Mtss1	-	↗	-	-

The reduced expression of Gfap and Slc1a3 at P0, but not at E18, might point to a decreased production of Slc1a3- and Gfap- expressing astrocytes. While it is true that mature astrocytes are only expected to be found from P4 onward, the differentiation into astrocytes is a process that starts at E10 already (Burns *et al,* 2009). As astrocytes are produced directly and indirectly from RGCs, which also express Gfap, the observed signals for these genes might partially originate in cells in the process of differentiating into astrocytes. Indeed, the observed mRNA expression of the more specific RGC marker Pax6 differs far less between the genotypes than

that of Gfap. However, cells differentiating into astrocytes do express Sox2 (Bani-Yaghoub *et al,* 2006). I do not observe reduced expression of Sox2-mRNA, and Sox2-expressing cell numbers in immunofluorescence stainings at P0 are increased, not reduced in Mtss1 KO mice.

To probe this interpretation further, the cell type composition of developing neocortex would need to be examined more closely, for instance by immunofluorescence stainings for Sox2, Yap1 and Gfap at P0, P1, P4 and P7. In addition, since expression of Gfap isoform Gfapδ has been implied in maintaining RGC characteristics as opposed to differentiation into astrocytes (Li *et al,* 2021b), extending these stainings to include specific Gfap isoforms would be another promising step.

Enhanced expression of Tbr2 at E18 (and possibly P0) suggests neurogenic IPCs to be affected by Mtss1 KO. $Tbr2^+$ IPCs are responsible for the generation of many glutamatergic, but not GABAergic neurons (Hevner, 2019). To differentiate an increase in IPC numbers from Tbr2 upregulation per cell, immunofluorescence stainings of frontal sections of brains from P0 mice were performed. These do support the interpretation of an increase of $Tbr2^+$ IPC numbers before and around birth. Interestingly, numbers of Sox2-expressing cells, which are expected to be RGCs and glial precursor cells, are increased in immunofluorescence stainings of P0 Mtss1 KO mice as well. Numbers of Pax6-expressing cells (RGCs only) are normal. $Sox2^+$ gliogenic precursor cells might thus be affected by Mtss1 KO in a similar way as $Tbr2^+$ neurogenic precursor cells are. However, this outcome is not consistent with results yielded by RT-qPCR, which showed neither increased Sox2 nor Pax6 expression, and needs clarification. For this reason, I will concentrate on Tbr2-expressing cells in the following.

As Tbr2-expressing IPCs are derived from RGCs, but are also able to self-amplify, several interpretations of the mentioned findings in KO mice are possible:

a) Fewer IPCs differentiate into mature neurons
b) IPCs differentiate into mature neurons later
c) RGCs produce more IPCs
d) IPCs self-amplify more
e) Fewer IPCs undergo programmed cell death
f) A combination of the above

At P0, expression of Tbr1, Dcx and Rbfox3 are not significantly altered. Arguably, a slight trend of increased Dcx and Tbr1-expression is present at P0, and of Rbfox3-expression at P7 in KO mice. Indeed, $Tbr1^+$ neurons have been shown to originate from $Tbr2^+$ IPCs (Englund *et al,* 2005), while Dcx- and Tbr1-expressing cells ultimately switch to expression of Rbfox3, a marker of mature neurons in the cerebral cortex (Magavi *et al,* 2012). On the other hand, the significantly lower expression of Gfap and Slc1a3/Glast in KO mice as compared to WT mice at P0 might be indicative of a smaller glial population in KO mice. Consequently, any small increase in expression of neuronal genes (such as Tbr1 and Dcx) could in fact be not absolute, but only relative, and entirely a consequence of these reduced numbers of glia.
Alternatively, appreciating that the glial cells that express Gfap and Slc1a3 represent more mature cells than Tbr2- and Sox2-expressing cells, one could argue that high numbers of $Tbr2^+$ and $Sox2^+$ cells and low numbers of $Gfap^+$ and $Slc1a3^+$ cells speaks for a more general developmental delay. Investigating gene expression at more time points than E18, P0, P7 and adulthood could unveil such developmental delay. Also, immunofluorescence stainings or RT-qPCR with increased sample size could elucidate whether a sequentially increased expression of Tbr2, then Tbr1, and

finally Rbfox3 is present in Mtss1 KO mice, and thus serve to interpret the likelihood of explanations a) and b).

Immunofluorescence stainings to mark possible colocalisation of proliferation markers with Tbr2 or Pax6 were explored to address explanations c) and d), that is whether either population, RGCs or IPCs are alone responsible for the increased number of cells expressing proliferation markers in perinatal KO mice, or whether both are. However, these stainings proved to be challenging to evaluate due to high cell density of $Tbr2^+$ and $Pax6^+$ cells, and ultimately not informative. Lineage tracing or cell sorting experiments might be helpful to understand which of the mechanisms proposed above are at work in Mtss1 KO mice. Considering explanation e), cell death is indeed a fate of many IPC daughter cells in healthy mice (Hevner, 2019). However, no indication of decreased apoptosis rate was found by RT-qPCR in E18 Mtss1 KO mice.

5.1.4 How Could Mtss1 Control Cortical Cell Numbers?

Regardless of what happens in perinatal development, in adult Mtss1 KO mice, distance from ependyma to meninges and cortical cell numbers are reduced. Bearing in mind the previously discussed findings, different possibilities how Mtss1 might influence these variables shall be addressed in the following.

1. A Direct Role in Mechanisms Needed for Removal of Surplus Cells

Programmed cell death and phagocytosis of surplus cells, including neurons, $Tbr2^+$ IPCs, and $Pax6^+$ RGCs, are normal mechanisms in neural development (Kandel, Schwartz, Jessell, Siegelbaum, Hudspeth, 2013), (Cunningham *et al,* 2013). While the data presented here do not point toward increased apoptosis in Mtss1 KO mouse

brains, this does not rule out the possibility of apoptosis playing a role in the observed phenotype. Firstly, a larger apoptotic event might take place between P0 and P7 or between P7 and adulthood. This could be invisible to the analysis at hand. It is also conceivable that the mechanism of cell loss is not detectable by observing the target genes used to mark for apoptosis in this study, as many different pathways of programmed cell death exist. Widening the list of target genes tested would be promising. It is also possible that a minor, hardly detectable increase in apoptosis frequency over a very long stretch of time affects total cell numbers in measurable amounts. This could affect mature neurons, but also undifferentiated progenitor cells, such as $Tbr2^{+}$ neurogenic IPCs.

Considering the involvement of Mtss1, no direct involvement of Mtss1 in apoptotic pathways has been described to my knowledge so far. Yet, another I-BAR domain protein, Baiap2l2, is known to regulate apoptosis (Xu *et al,* 2019). As apoptotic signals can be transduced via the actin cytoskeleton (Desouza *et al,* 2012), one could speculate whether Mtss1 does influence apoptosis by this pathway. However, a much better explored mechanism by which Mtss1 might participate in various signalling pathways, including those promoting or inhibiting apoptosis, is its ability to modulate receptor internalisation. In fact, Mtss1 overexpression in cell culture has been shown to promote Cxcr4 internalisation, ubiquitination, sorting into multivesicular bodies, and consequently degradation (Matskova *et al,* 2024). Cxcr4 has been described in many contexts, including pro- and antiapoptotic processes (Kremer *et al,* 2013), (Yaday *et al,* 2016), but also neuronal migration (Hevner, 2019), (Vilz *et al,* 2005). The latter has previously been discussed as a possible explanation of cerebellar granule cell ectopies in MTSS1 KO (Sistig *et al,* 2017). Cunningham *et al* (2013) and Vaid & Huttner (2020) previously suggested that especially in late foetal

development, significant numbers of RGCs, $Tbr2^+$ neurogenic IPCs, and possibly glial progenitor cells, are phagocytosed. Notably, the majority of phagocytosed cells seem to display no signs of apoptosis. It is therefore an option, that an earlier generation of increased IPC numbers caused by increased proliferation, altered differentiation, or faulty migration, is later counteracted by phagocytosis. Indeed, Mtss1 is also expressed by microglia (Sjöstedt *et al,* 2020), allowing the speculation that Mtss1 influences this process by acting on the phagocytosing, not the phagocytosed cells. However, to my knowledge, no roles of Mtss1 in phagocytosis have been described so far. While another I-BAR protein, IBARa, does indeed participate in phagocytosis, it is a protein found in social amoeba *Dictyostelium discoideum* (Linkner *et al,* 2014), and thus only remotely related to mammalian Mtss1.

2. A Role in Neurite or Synapse Formation or Function, Leading to later Cell Removal

Activity-dependent apoptosis, resulting from very little neuronal contact, and excitotoxicity, which can result from too much neuronal contact or an insufficient neurotransmitter clearance, can be caused by disturbances of synapse formation or function. The involvement of Mtss1 in dendrite and synapse formation is well-documented (Saarikangas *et al,* 2015), (Sistig *et al,* 2017), (Kawabata Galbraith *et al,* 2018), (Kawabata, 2018), (Parker *et al,* 2023), and other I-BAR domain proteins are relevant in this context as well (Chou *et al,* 2017). Mtss1 deficiency might thus promote excessive or insufficient synaptic integration and eventual cell death in some neurons, explaining the thinning of the cerebral cortex reflected by the reduced distance from ependyma to meninges seen in Mtss1 KO mice. Interestingly, Mtss1 deficiency has been shown to increase activity of Rho-GPTase Cdc42 in bone marrow cells (Zhan *et al,* 2016). Inhibition of Cdc42 is however required for normal

dendritic branching. If control of Cdc42 fails in development, the result is reduced dendritic branching and cortical thickness (Rosário *et al,* 2012). This suggests a prospective molecular mechanism how Mtss1 deficiency could impinge on neuritogenesis and ultimately neurogenesis. It also shows, that reduced neurite formation, in addition to the formation of insufficient numbers of neurons, can explain the reduced distance from ependyma to meninges in Mtss1 KO mice.

3. A Role in Proliferation, Differentiation, or Migration

Obviously, reduced proliferation can be the cause of reduced cortical cell numbers. However, disturbances in differentiation or migration, which may not reduce cell numbers directly, can still influence cortical cell numbers profoundly. As mentioned earlier, malpositioned and undifferentiated cells may be removed by apoptosis or be phagocytosed. It should finally be noted that changes in the population of IPCs can not only influence the pool of cells that originate from IPCs. Indeed, RGCs receive feedback from IPCs, and regulate their proliferative capacities accordingly (Johnson & Ghashghaei, 2020).

I find no indication of increased apoptosis rates in Mtss1 KO mice, and know of no involvement of Mtss1 in phagocytosis. On that account, I overall prefer explanation 3 as it is described in the preceding paragraph as the most likely explanation of Mtss1 in cortical development. Mtss1 has previously been shown to play a role in controlling migration (Glassmann *et al,* 2007), (Dawson *et al,* 2012a) and proliferation (Dawson *et al,* 2012b). In addition, while I find increased numbers of Ki67-expressing, proliferating cells, this might actually be the consequence of reduced proliferation, as outlined earlier. Alternatively, by assuming an interaction of Mtss1 and Egfr taking

effect in the context of cortical development, several of the observed effects of Mtss1 KO on CNS development would be consistent with a combination of the previously stated explanations 2 and 3, where proliferation, differentiation, and synaptic function would all be affected, as discussed in the following section.

5.1.5 Egfr-Mtss1-Interaction Could Explain the Decreased Telencephalic Cell Count in Adult Mtss1 KO Mice

Egfr is a receptor tyrosine kinase from the ErbB-family of proteins. Egfr binds a number of different ligands, and can also be activated or inhibited in a ligand-independent manner by association with cell adhesion molecules. After activation, Egfr is endocytosed, and can either be recycled to the cell surface, or degraded (Kozlova & Sytnyk, 2024), (Wagner *et al,* 2006). In cancer biology, Mtss1 has been demonstrated to modulate EGF signalling by controlling the abundance of Egfr on the cell surface (Khan & Steeg, 2021), (Dawson *et al,* 2012b). In culture of mouse embryonic fibroblasts, EGF uptake was shown to be controlled by Mtss1 as well (Quinones *et al,* 2010). Another I-BAR domain protein, Baiap2l2, also activates Egfr signalling (Xu *et al,* 2019). In addition, although the described interaction of Egfr and Mtss1 takes place on the protein level, RT-qPCRs data obtained in this project show a reduced expression of Egfr on mRNA level in P0 Mtss1 KO mice, and a similar trend in adult Mtss1 KO mice. This could either indicate another level of interaction, or a change in Egfr-expressing cell populations due to KO of Mtss1.

Egfr activation has profound effects, involving several signalling pathways and hundreds of proteins. The exact results of Egfr activation depend on the ligand, on cell type and contacts with other cells, but often include modulation of proliferation and migration (Kozlova & Sytnyk, 2024), (Wagner *et al,* 2006). Fittingly, Egfr is

expressed in regions of high proliferation and migration during neural development, and especially in late embryonic development (Robson *et al,* 2018). Depending on their genetic background and the individual, Egfr KO mice variably express many malformations, including lethal abnormalities of lung and placenta. They also display a dramatic postnatal degeneration of the cerebral cortex and olfactory bulbs, and to a lesser extent of the hippocampus and thalamus. This degeneration is accompanied by hemorrhage (Sibilia *et al,* 1998). Both overexpression of Egfr and Egfr deficiency impair expansion of neural stem cells (Robson *et al,* 2018).

Zhang *et al* (2023) analysed mice with a random deletion of Egfr from a small, randomly selected subset of forebrain precursors (mosaic deletion), which showed a milder phenotype. These mice exhibited regional apoptosis and necrosis in the cerebral cortex around P0, although global numbers of c-Casp3^{+} (apoptotic) cells were normal. Sagittal sections presented by Zhang *et al* (2023) suggest reduced distance from ependyma to meninges in adult mosaic Egfr KO mice also. Postnatal loss of neurons was partially explained as a secondary effect to a lack of astrocytes and altered astrocyte function, resulting in reduced glutamate clearance and excitotoxicity (Robson *et al,* 2018). Indeed, Egfr plays a role in the production of glia (Sun *et al,* 2005), (Romano & Bucci, 2020), and forms a mutual positive feedback with the expression of the already mentioned transcription factor Sox2 (Hu *et al,* 2010), (Romano & Bucci, 2020). Sox2 is a well-established factor in the switch to gliogenesis in its own right (Bani-Yaghoub *et al,* 2006), (Graham *et al,* 2003). Interestingly, Zhang *et al* (2023) showed that while a significant proportion of gliogenesis is Egfr-dependent, Egfr-independent gliogenic precursors partially compensate decreased astrocyte production in absence of Egfr. As the authors

indicated, this happens at the cost of neuronal production, and includes an elevation in numbers of reactive and fibrous astrocytes, which exhibit high Gfap expression.

Consistent with the early decrease of astrocyte production and with later astrogliosis observed in Egfr deficiency, the experiments presented here show decreased expression of glial markers around P0, but highly increased expression of Gfap in some adult Mtss1 KO mice. In this line of reasoning, the high numbers of neurogenic $Tbr2^{+}$ IPCs in Mtss1 KO mice in late embryonic and perinatal development could be interpreted as partial failure to perform the switch from neurogenesis to gliogenesis subsequent to decreased Egfr signalling. Furthermore, adult Mtss1-KO mice do exhibit reduced distance from ependyma to in meninges, although expression of Casp3-mRNA is not globally increased in the brains of Mtss1 KO mice at any considered time point. Finally, haemorrhage has been observed several times in the preparation of Mtss1 KO mice by our research group, but no systematic assessment of this observation has been made yet. All these observations would be consistent with effects of mild Egfr deficiency. It remains to be seen if the observed shifts in neural progenitor cell populations (altered expression and distribution of Tbr2 and Sox2) in Mtss1 are really linked to altered Egfr signalling, but some kind of involvement of the Egfr in the Mtss1-KO phenotype is already indicated by the decreased Egfr expression measured in P0 Mtss1 KO mice of this project.

While the low specificity of available anti Mtss1-antibodies complicates studies on protein-protein interaction, investigating an involvement of Egfr in general seems feasible by performing cell sorting experiments and immunofluorescence stainings. This could elucidate whether Egfr surface expression is changed by Mtss1 expression in neural development, in which cells this happens, and which consequences this has specifically.

5.1.6 The Involvement of Mtss1 in The PCP Pathway is Unclear

Given that Mtss1 has been reported to associate with cilium basal bodies (Bershteyn *et al,* 2010), the existence of adult neural stem cells in the ependyma (Ortiz-Álvarez *et al,* 2019), and yet unpublished data by Barbara Kalthoff showing expression of Mtss1 in ependymal cells, an involvement of the ependyma in the CNS phenotype of Mtss1 deficiency was suspected. Hence, planar polarity of E1 cells and cell numbers of B1 were investigated in adult mice. Here, analysis of immunofluorescence stainings of lateral ventricle wholemounts do not show any difference in numbers of B1 adult stem cells between WT and Mtss1 KO mice per ependymal area, indicating that this population of adult neural stem cells are present in similar numbers regardless of Mtss1 expression. It has to be said however, that other types of adult neural stem cells, which do not contact the ventricular surface, do exist in the adult VZ-SZV (Cebrian-Silla *et al,* 2025). In addition, as has been mentioned before, the enlarged volume of the ventricular system in Mtss1 KO probably bestows the ventricular system with a larger ependymal area also. This means, that if the numbers of B1 cells are the same per area in both WT and KO mice, more B1 cells should exist in KO mice overall.

Regarding planar polarity, translational- (basal body positioning), but not rotational polarity (basal body orientation) of ependymal E1 cells is disturbed under Mtss1 deficiency, as presented here. This could suggest an involvement of Mtss1 in the control or realisation of PCP. However, the differences that were observed are only slight. Unpublished data by Barbara Kalthoff suggest a reduced number of multiciliated cells, and increased surface area in differentiating primary cultures of ependymal cells, when Mtss1 is knocked out. Indeed, they also show CSF flow close

to the ependyma to be disturbed, which could well be related to altered planar polarity (Guirao *et al,* 2010).

A literature research for brain phenotypes that feature disturbed PCP yielded overlaps, but also differences to the effects produced by Mtss1 deficiency. Perhaps the most similar phenotype overall is seen in mice deficient in Celsr1 or Id4. In the case of Celsr1-deficiency, a mild disturbance of rotational polarity, but a stronger disturbance of translational polarity can be observed, both in ependymal cells and inner hair cells of the inner ear (Boutin *et al,* 2014), which were not systematically investigated in the project presented here.

Celsr1-deficient mice exhibit hypoplasia of the cerebral cortex, not unlike the morphology of brains of Mtss1-deficient mice. In these mice, as is the case for Mtss1-KO mice studied here, numbers of IPCs are also affected, although in Celsr1-deficiency they are decreased, rather than increased. On the other hand, unlike in Mtss1 deficiency, the numbers of ependymal pinwheels and B1 cells are increased in Celsr1-deficient mice (Boucherie *et al,* 2018), and these mice display neural tube closure defects (Boutin *et al,* 2014). While knockdown of the Mtss1 homologue XMIM in *Xenopus laevis* produces neural tube closure defects (Liu *et al,* 2011), I do not know of any similar observations in mice, and data on congenital mutations of Mtss1 in humans are limited. Interestingly, the cause for some of the neurodevelopmental effects of Celsr1-deficiency was identified as an insufficient uptake of retinoic acid ultimately brought about by a reduction in complexity of cellular processes, in this case the meningeal processes of RGCs (Boucherie *et al,* 2018). This is reminiscent to the effects of Mtss1-deficiency on some cellular protrusions, like the dendrites of Purkinje cells.

In the case of Id4-deficiency, adult mice present overall decreased size of various telencephalic structures, including the cerebral cortex. They also show increased ventricular volume, and decreased numbers of S100B-expressing glial cells across the brain (Bedford *et al*, 2005). Rotational polarity of ependymal cells has not been evaluated in Id4-deficient mice, as far as I know. However, translational polarity of ependymal cells was shown to be disturbed. In addition, ependymal cell differentiation has been reported to be delayed, and overall cell shape to be shifted towards a flatter appearance. Furthermore, numbers of B1 cells were normal (Rocamonde *et al*, 2021). These features would be consistent with both my own findings and currently unpublished observations of cultured Mtss1-deficient ependymal cells by Barbara Kalthoff. Around E11.5-E13.5, neural progenitor cells of Id4-deficient mice were found to exhibit a prolonged cell cycle and precocious differentiation. The authors also found increased numbers of Tbr2-expressing cells in the VZ. At E15.5 and E18.5, expression of Tbr1 was increased (Yun *et al*, 2004). While my own data on embryonic development of Mtss1 deficient mice is limited to that gained from E18 mice, the effects of Id4-deficiency seem reminiscent to what I found in Mtss1-KO mice in some aspects.

Both the cases of Id4 and Celsr1 show that the phenotype of Mtss1-deficiency has parallels with deficiency in PCP-influencing proteins. Since Egfr is often distributed unevenly during asymmetric divisions of neural progenitor cells (Sun *et al,* 2005), the interpretation of Mtss1 KO disturbing cell polarity would even be compatible with the interpretation of an involvement of Egfr, as presented before. I do however find the assumption of Mtss1 participating in endocytosis pathways of Egfr in neural progenitor cells more compelling, as this mechanism has already been described in other cells (Dawson *et al,* 2012b). To my knowledge, no direct interactions of Mtss1

with either Ceslr1 or Id4 have been found so far. Overall, it is unclear if and how the small observed changes of planar cell polarity relate to other malformations of Mtss1 KO mice.

5.2 Conclusion

Based on the experiments presented here, I can confirm that reduction of distance from ventricle to meninges (“cortical thickness”) under Mtss1 KO is a feature of the phenotype of our model of Mtss1Gt(RRI034)Byg – mice. The obtained results further indicate that the phenotype also includes reduction of cell numbers and relative increase of Gfap expression in the caudal telencephalon. In late embryonic and perinatal development of Mtss1 KO mouse neurogenic germinal zones, I could show numbers of cells in a proliferative state as well as numbers of (immature) neurogenic IPCs to be increased. Numbers of more mature neurons are not significantly changed. At the same time, it appears that numbers of another more mature population of cells, namely Gfap- and Slc1a3-expressing glial cells, are reduced. I propose that a delay or a partial failure of the neurogenic-gliogenic switch due to missing stabilisation of Egfr-signalling by Mtss1 in KO mice may explain these findings best. While this process has yet to be confirmed with other experiments, the outcomes presented here already show effects of Mtss1 on Egfr expression in neural development. It seems probable that the malformations described here have behavioural and functional repercussions for the affected animals. Which of the known morphological features of Mtss1 KO can be linked to what individual aspect of its previously described behavioural phenotype is another compelling question left to future studies.

6 References

Allen Institute for Brain Science (2008) Allen Brain Explorer beta. https://connectivity.brain-map.org/3d-viewer?v=1. 14 March 2025

Arai Y, Taverna E (2017) Neural Progenitor Cell Polarity and Cortical Development. Front Cell Neurosci 11: 384

Aung N, Vargas JD, Yang C, Cabrera CP, Warren HR, Fung K, Tzanis E, Barnes MR, Rotter JI, Taylor KD et al (2019) Genome-Wide Analysis of Left Ventricular Image-Derived Phenotypes Identifies Fourteen Loci Associated With Cardiac Morphogenesis and Heart Failure Development. Circulation 140: 1318–1330

Baldarelli RM, Smith CL, Ringwald M, Richardson JE, Bult CJ (2024) Mouse Genome Informatics: an integrated knowledgebase system for the laboratory mouse. Genetics 227

Baldarelli RM, Smith CL, Ringwald M, Richardson JE, Bult CJ (2025) References associated with Allele Mtss1Gt(RRI034)Byg. https://www.informatics.jax.org/reference/allele/MGI:4128729?typeFilter=Literature. 16 May 2025

Bani-Yaghoub M, Tremblay RG, Lei JX, Zhang D, Zurakowski B, Sandhu JK, Smith B, Ribecco-Lutkiewicz M, Kennedy J, Walker PR et al (2006) Role of Sox2 in the development of the mouse neocortex. Dev Biol 295: 52–66

Basso M, Mahuzier A, Ali SK, Marty A, Faucourt M, Lennon-Duménil A-M, Srivastava A, Khoury Damaa M, Bankolé A, Meunier A et al (2025) Actin-based deformations of the nucleus control mouse multiciliated ependymal cell differentiation. Dev Cell 60: 749-761.e5

Batschelet E (1981) Circular Statistics in Biology. London, England: Academic Press INC.

Bedford L, Walker R, Kondo T, van Crüchten I, King ER, Sablitzky F (2005) Id4 is required for the correct timing of neural differentiation. Dev Biol 280: 386–395

Bershteyn M, Atwood SX, Woo W-M, Li M, Oro AE (2010) MIM and cortactin antagonism regulates ciliogenesis and hedgehog signaling. Dev Cell 19: 270–283

Betts JG, Desaix P, Johnson E, Johnson JE, Koral O, Kruse D, Poe, Brandon, Wise, James, Womble M, Young K (2022) Anatomy and physiology, 2e. Houston, Texas: OpenStax

Bezanilla M, Gladfelter AS, Kovar DR, Lee W-L (2015) Cytoskeletal dynamics: a view from the membrane. J Cell Biol 209: 329–337

Bologna-Molina R, Mosqueda-Taylor A, Molina-Frechero N, Mori-Estevez A-D, Sánchez-Acuña G (2013) Comparison of the value of PCNA and Ki-67 as markers of cell proliferation in ameloblastic tumors. Med Oral Patol Oral Cir Bucal 18: e174-9

Bompard G, Sharp SJ, Freiss G, Machesky LM (2005) Involvement of Rac in actin cytoskeleton rearrangements induced by MIM-B. J Cell Sci 118: 5393–5403

Boucherie C, Boutin C, Jossin Y, Schakman O, Goffinet AM, Ris L, Gailly P, Tissir F (2018) Neural progenitor fate decision defects, cortical hypoplasia and behavioral impairment in Celsr1-deficient mice. Mol Psychiatry 23: 723–734

Boutin C, Labedan P, Dimidschstein J, Richard F, Cremer H, André P, Yang Y, Montcouquiol M, Goffinet AM, Tissir F (2014) A dual role for planar cell polarity genes in ciliated cells. Proc Natl Acad Sci U S A 111: E3129-38

Budday S, Steinmann P, Kuhl E (2015) Physical biology of human brain development. Front Cell Neurosci 9: 257

Burns KA, Murphy B, Danzer SC, Kuan C-Y (2009) Developmental and post-injury cortical gliogenesis: a genetic fate-mapping study with Nestin-CreER mice. Glia 57: 1115–1129

Carvajal-Gonzalez JM, Mulero-Navarro S, Mlodzik M (2016) Centriole positioning in epithelial cells and its intimate relationship with planar cell polarity. Bioessays 38: 1234–1245

Cavalcante GC, Schaan AP, Cabral GF, Santana-da-Silva MN, Pinto P, Vidal AF, Ribeiro-Dos-Santos Â (2019) A Cell's Fate: An Overview of the Molecular Biology and Genetics of Apoptosis. Int J Mol Sci 20

Cebrian-Silla A, Nascimento MA, Mancia W, Gonzalez-Granero S, Romero-Rodriguez R, Obernier K, Steffen DM, Lim DA, Garcia-Verdugo JM, Alvarez-Buylla A (2025) Neural stem cell relay from B1 to B2 cells in the adult mouse ventricular-subventricular zone. Cell Rep 44: 115264

Chen M, Shan L, Gan Y, Tian L, Zhou J, Zhu E, Yuan H, Li X, Wang B (2022) Metastasis suppressor 1 controls osteoblast differentiation and bone homeostasis through regulating Src-Wnt/β-catenin signaling. Cell Mol Life Sci 79: 107

Chou AM, Sem KP, Lam WJ, Ahmed S, Lim CY (2017) Redundant functions of I-BAR family members, IRSp53 and IRTKS, are essential for embryonic development. Sci Rep 7: 40485

Christ AF, Franze K, Gautier H, Moshayedi P, Fawcett J, Franklin RJM, Karadottir RT, Guck J (2010) Mechanical difference between white and gray matter in the rat cerebellum measured by scanning force microscopy. J Biomech 43: 2986–2992

Cunningham CL, Martínez-Cerdeño V, Noctor SC (2013) Microglia regulate the number of neural precursor cells in the developing cerebral cortex. J Neurosci 33: 4216–4233

Dawson JC, Bruche S, Spence HJ, Braga VMM, Machesky LM (2012a) Mtss1 promotes cell-cell junction assembly and stability through the small GTPase Rac1. PLoS One 7: e31141

Dawson JC, Timpson P, Kalna G, Machesky LM (2012b) Mtss1 regulates epidermal growth factor signaling in head and neck squamous carcinoma cells. Oncogene 31: 1781–1793

Desouza M, Gunning PW, Stehn JR (2012) The actin cytoskeleton as a sensor and mediator of apoptosis. Bioarchitecture 2: 75–87

Duan D, Fu Y, Paxinos G, Watson C (2013) Spatiotemporal expression patterns of Pax6 in the brain of embryonic, newborn, and adult mice. Brain Struct Funct 218: 353–372

Duy PQ, Weise SC, Marini C, Li X-J, Liang D, Dahl PJ, Ma S, Spajic A, Dong W, Juusola J et al (2022) Impaired neurogenesis alters brain biomechanics in a neuroprogenitor-based genetic subtype of congenital hydrocephalus. Nat Neurosci 25: 458–473

Eichele G, Bodenschatz E, Ditte Z, Günther A-K, Kapoor S, Wang Y, Westendorf C (2020) Cilia-driven flows in the brain third ventricle. Philos Trans R Soc Lond B Biol Sci 375: 20190154

Elias LAB, Wang DD, Kriegstein AR (2007) Gap junction adhesion is necessary for radial migration in the neocortex. Nature 448: 901–907

Englund C, Fink A, Lau C, Pham D, Daza RAM, Bulfone A, Kowalczyk T, Hevner RF (2005) Pax6, Tbr2, and Tbr1 are expressed sequentially by radial glia, intermediate progenitor cells, and postmitotic neurons in developing neocortex. J Neurosci 25: 247–251

Glassmann A, Molly S, Surchev L, Nazwar TA, Holst M, Hartmann W, Baader SL, Oberdick J, Pietsch T, Schilling K (2007) Developmental expression and differentiation-related neuron-specific splicing of metastasis suppressor 1 (Mtss1) in normal and transformed cerebellar cells. BMC Dev Biol 7: 111

Graham V, Khudyakov J, Ellis P, Pevny L (2003) SOX2 functions to maintain neural progenitor identity. Neuron 39: 749–765

Guirao B, Meunier A, Mortaud S, Aguilar A, Corsi J-M, Strehl L, Hirota Y, Desoeuvre A, Boutin C, Han Y-G et al (2010) Coupling between hydrodynamic forces and planar cell polarity orients mammalian motile cilia. Nat Cell Biol 12: 341–350

Harkin LF, Gerrelli D, Gold Diaz DC, Santos C, Alzu'bi A, Austin CA, Clowry GJ (2016) Distinct expression patterns for type II topoisomerases IIA and IIB in the early foetal human telencephalon. J Anat 228: 452–463

Hayn-Leichsenring G, Liebig C, Miething A, Schulz A, Kumar S, Schwalbe M, Eiberger B, Baader SL (2011) Cellular distribution of metastasis suppressor 1 and the shape of cell bodies are temporarily altered in Engrailed-2 overexpressing cerebellar Purkinje cells. Neuroscience 189: 68–78

Herawati E, Taniguchi D, Kanoh H, Tateishi K, Ishihara S, Tsukita S (2016) Multiciliated cell basal bodies align in stereotypical patterns coordinated by the apical cytoskeleton. J Cell Biol 214: 571–586

Hevner RF (2019) Intermediate progenitors and Tbr2 in cortical development. J Anat 235: 616–625

Hohmann T, Dehghani F (2019) The Cytoskeleton-A Complex Interacting Meshwork. Cells 8

Hu Q, Zhang L, Wen J, Wang S, Li M, Feng R, Yang X, Li L (2010) The EGF receptor-sox2-EGF receptor feedback loop positively regulates the self-renewal of neural precursor cells. Stem Cells 28: 279–286

Huang H, He W, Tang T, Qiu M (2023) Immunological Markers for Central Nervous System Glia. Neurosci Bull 39: 379–392

Huang Y, Lemire G, Briere LC, Liu F, Wessels MW, Wang X, Osmond M, Kanca O, Lu S, High FA et al (2022) The recurrent de novo c.2011CT missense variant in MTSS2 causes syndromic intellectual disability. Am J Hum Genet 109: 1923–1931

Huang Z, Hu J, Pan J, Wang Y, Hu G, Zhou J, Mei L, Xiong W-C (2016) YAP stabilizes SMAD1 and promotes BMP2-induced neocortical astrocytic differentiation. Development 143: 2398–2409

Ihrie RA, Alvarez-Buylla A (2011) Lake-front property: a unique germinal niche by the lateral ventricles of the adult brain. Neuron 70: 674–686

Iliff JJ, Wang M, Liao Y, Plogg BA, Peng W, Gundersen GA, Benveniste H, Vates GE, Deane R, Goldman SA et al (2012) A paravascular pathway facilitates CSF flow through the brain parenchyma and the clearance of interstitial solutes, including amyloid β. Sci Transl Med 4: 147ra111

Jain N, Iyer KV, Kumar A, Shivashankar GV (2013) Cell geometric constraints induce modular gene-expression patterns via redistribution of HDAC3 regulated by actomyosin contractility. Proc Natl Acad Sci U S A 110: 11349–11354

Johnson CA, Ghashghaei HT (2020) Sp2 regulates late neurogenic but not early expansive divisions of neural stem cells underlying population growth in the mouse cortex. Development 147

Kádár A, Wittmann G, Liposits Z, Fekete C (2009) Improved method for combination of immunocytochemistry and Nissl staining. J Neurosci Methods 184: 115–118

Kaiser K, Bryja V (2020) Choroid Plexus: The Orchestrator of Long-Range Signalling Within the CNS. Int J Mol Sci 21

Kandel, Schwartz, Jessell, Siegelbaum, Hudspeth (ed) (2013) Principles of Neural Science: Fifth Edition. pp. 1166-1174, 1188-1196, 1199-1203: McGraw-Hill

Kawabata K (2018) Functional Analysis of MTSS1 Regulation of Purkinje Cell Dendritic Development and Actin Dynamics

Kawabata Galbraith K, Fujishima K, Mizuno H, Lee S-J, Uemura T, Sakimura K, Mishina M, Watanabe N, Kengaku M (2018) MTSS1 Regulation of Actin-Nucleating Formin DAAM1 in Dendritic Filopodia Determines Final Dendritic Configuration of Purkinje Cells. Cell Rep 24: 95-106.e9

Kawauchi T (2015) Cellullar insights into cerebral cortical development: focusing on the locomotion mode of neuronal migration. Front Cell Neurosci 9: 394

Khan I, Steeg PS (2021) Endocytosis: a pivotal pathway for regulating metastasis. Br J Cancer 124: 66–75

Kim N, Li Y, Yu R, Kwon H-S, Song A, Jun M-H, Jeong J-Y, Lee JH, Lim H-H, Kim M-J et al (2024) Repulsive Sema3E-Plexin-D1 signaling coordinates both axonal extension and steering via activating an autoregulatory factor, Mtss1. Elife 13

Kole AJ, Annis RP, Deshmukh M (2013) Mature neurons: equipped for survival. Cell Death Dis 4: e689

Kowalczyk T, Pontious A, Englund C, Daza RAM, Bedogni F, Hodge R, Attardo A, Bell C, Huttner WB, Hevner RF (2009) Intermediate neuronal progenitors (basal progenitors) produce pyramidal-projection neurons for all layers of cerebral cortex. Cereb Cortex 19: 2439–2450

Kozlova I, Sytnyk V (2024) Cell Adhesion Molecules as Modulators of the Epidermal Growth Factor Receptor. Cells 13

Kremer KN, Peterson KL, Schneider PA, Meng XW, Dai H, Hess AD, Smith BD, Rodriguez-Ramirez C, Karp JE, Kaufmann SH et al (2013) CXCR4 chemokine receptor signaling induces apoptosis in acute myeloid leukemia cells via regulation of the Bcl-2 family members Bcl-XL, Noxa, and Bak. J Biol Chem 288: 22899–22914

Lee JL, Streuli CH (2014) Integrins and epithelial cell polarity. J Cell Sci 127: 3217–3225

Lee L (2013) Riding the wave of ependymal cilia: genetic susceptibility to hydrocephalus in primary ciliary dyskinesia. J Neurosci Res 91: 1117–1132

Lee SH, Kerff F, Chereau D, Ferron F, Klug A, Dominguez R (2007) Structural basis for the actin-binding function of missing-in-metastasis. Structure 15: 145–155

Li L, Baxter SS, Gu N, Ji M, Zhan X (2017) Missing-in-metastasis protein downregulates CXCR4 by promoting ubiquitylation and interaction with small Rab GTPases. J Cell Sci 130: 1475–1485

Li X, Liu G, Yang L, Li Z, Zhang Z, Xu Z, Cai Y, Du H, Su Z, Wang Z et al (2021a) Decoding Cortical Glial Cell Development. Neurosci Bull 37: 440–460

Li Y, Zhang L-N, Chong L, Liu Y, Xi F-Y, Zhang H, Duan X-L (2021b) Prenatal ethanol exposure impairs the formation of radial glial fibers and promotes the transformation of GFAPδ-positive radial glial cells into astrocytes. Mol Med Rep 23

Liang XG, Hoang K, Meyerink BL, Kc P, Paraiso K, Wang L, Jones IR, Zhang Y, Katzman S, Finn TS et al (2024) A conserved molecular logic for neurogenesis to gliogenesis switch in the cerebral cortex. Proc Natl Acad Sci U S A 121: e2321711121

Lin J, Liu J, Wang Y, Zhu J, Zhou K, Smith N, Zhan X (2005) Differential regulation of cortactin and N-WASP-mediated actin polymerization by missing in metastasis (MIM) protein. Oncogene 24: 2059–2066

Lindsten T, Golden, Jeffrey A., Zong, Wei-Xing, Minarcik J, Harris MH, Thomposone CB (2003) TheProapoptotic Activities of Bax and Bak Limit the Size of the Neural Stem Cell Pool. J Neurosci 2003

Linkner J, Witte G, Zhao H, Junemann A, Nordholz B, Runge-Wollmann P, Lappalainen P, Faix J (2014) The inverse BAR domain protein IBARa drives membrane remodeling to control osmoregulation, phagocytosis and cytokinesis. J Cell Sci 127: 1279–1292

Liu W, Komiya Y, Mezzacappa C, Khadka DK, Runnels L, Habas R (2011) MIM regulates vertebrate neural tube closure. Development 138: 2035–2047

Luxen D, Gielen GH, Waha A, Isselstein L, Müller T, Koch P, Hammes J, Becker A, Simon M, Wurst P et al (2017) MTSS1 is epigenetically regulated in glioma cells and inhibits glioma cell motility. Transl Oncol 10: 70–79

Magavi S, Friedmann D, Banks G, Stolfi A, Lois C (2012) Coincident generation of pyramidal neurons and protoplasmic astrocytes in neocortical columns. J Neurosci 32: 4762–4772

Mardia KV, Jupp PE (2000) Directional Statistics. Baffins Lane, Chichester, England: John Wiley & Sons Ltd

Matskova L, Zheng S, Kashuba E, Ernberg I, Aspenström P (2024) MTSS1: beyond the integration of actin and membrane dynamics. Cell Mol Life Sci 81: 472

McHugh T, Zou J, Volkov VA, Bertin A, Talapatra SK, Rappsilber J, Dogterom M, Welburn JPI (2019) The depolymerase activity of MCAK shows a graded response to Aurora B kinase phosphorylation through allosteric regulation. J Cell Sci 132

Meijering E, Dzyubachyk O, Smal I (2012) Methods for cell and particle tracking. Methods Enzymol 504: 183–200

Merino F, Pospich S, Raunser S (2020) Towards a structural understanding of the remodeling of the actin cytoskeleton. Semin Cell Dev Biol 102: 51–64

Meyer HV, Dawes TJW, Serrani M, Bai W, Tokarczuk P, Cai J, Marvao A de, Henry A, Lumbers RT, Gierten J et al (2020) Genetic and functional insights into the fractal structure of the heart. Nature 584: 589–594

Minkeviciene R, Hlushchenko I, Virenque A, Lahti L, Khanal P, Rauramaa T, Koistinen A, Leinonen V, Noe FM, Hotulainen P (2019) MIM-Deficient Mice Exhibit Anatomical Changes in Dendritic Spines, Cortex Volume and Brain Ventricles, and Functional Changes in Motor Coordination and Learning. Front Mol Neurosci 12: 276

Mirzadeh Z, Doetsch F, Sawamoto K, Wichterle H, Alvarez-Buylla A (2010) The subventricular zone en-face: wholemount staining and ependymal flow. J Vis Exp

Molyneaux BJ, Arlotta P, Menezes JRL, Macklis JD (2007) Neuronal subtype specification in the cerebral cortex. Nat Rev Neurosci 8: 427–437

Morley MP, Wang X, Hu R, Brandimarto J, Tucker NR, Felix JF, Smith NL, van der Harst P, Ellinor PT, Margulies KB et al (2019) Cardioprotective Effects of MTSS1 Enhancer Variants. Circulation 139: 2073–2076

Nevin LM, Xiao T, Staub W, Baier H (2011) Topoisomerase IIbeta is required for lamina-specific targeting of retinal ganglion cell axons and dendrites. Development 138: 2457–2465

Nielsen CF, Zhang T, Barisic M, Kalitsis P, Hudson DF (2020) Topoisomerase IIα is essential for maintenance of mitotic chromosome structure. Proc Natl Acad Sci U S A 117: 12131–12142

Nikolopoulou E, Galea GL, Rolo A, Greene NDE, Copp AJ (2017) Neural tube closure: cellular, molecular and biomechanical mechanisms. Development 144: 552–566

Ortiz-Álvarez G, Daclin M, Shihavuddin A, Lansade P, Fortoul A, Faucourt M, Clavreul S, Lalioti M-E, Taraviras S, Hippenmeyer S et al (2019) Adult Neural Stem Cells and Multiciliated Ependymal Cells Share a Common Lineage Regulated by the Geminin Family Members. Neuron 102: 159-172.e7

Parker SS, Ly KT, Grant AD, Sweetland J, Wang AM, Parker JD, Roman MR, Saboda K, Roe DJ, Padi M et al (2023) EVL and MIM/MTSS1 regulate actin cytoskeletal remodeling to promote dendritic filopodia in neurons. J Cell Biol 222

Penisson M, Ladewig J, Belvindrah R, Francis F (2019) Genes and Mechanisms Involved in the Generation and Amplification of Basal Radial Glial Cells. Front Cell Neurosci 13: 381

Petrov P, Sarapulov AV, Eöry L, Scielzo C, Scarfò L, Smith J, Burt DW, Mattila PK (2019) Computational analysis of the evolutionarily conserved Missing In Metastasis/Metastasis Suppressor 1 gene predicts novel interactions, regulatory regions and transcriptional control. Sci Rep 9: 4155

Pilaz L-J, McMahon JJ, Miller EE, Lennox AL, Suzuki A, Salmon E, Silver DL (2016) Prolonged Mitosis of Neural Progenitors Alters Cell Fate in the Developing Brain. Neuron 89: 83–99

Podieh F, Overboom MC, Knol JC, Piersma SR, Goeij-de Haas R, Pham TV, Jimenez CR, Hordijk PL (2024) AAMP and MTSS1 Are Novel Negative Regulators of Endothelial Barrier Function Identified in a Proteomics Screen. Cells 13

Posit Team (2023) RStudio: Integrated Development Environment for R: Posit Software, PBC, Boston, MA

Pykäläinen A, Boczkowska M, Zhao H, Saarikangas J, Rebowski G, Jansen M, Hakanen J, Koskela EV, Peränen J, Vihinen H et al (2011) Pinkbar is an epithelial-specific BAR domain protein that generates planar membrane structures. Nat Struct Mol Biol 18: 902–907

Quinones GA, Jin J, Oro AE (2010) I-BAR protein antagonism of endocytosis mediates directional sensing during guided cell migration. J Cell Biol 189: 353–367

R Core Team (2021) R: A language and environment for statistical computing: R Foundation for Statistical Computing, Vienna, Austria

Rakic P (2009) Evolution of the neocortex: a perspective from developmental biology. Nat Rev Neurosci 10: 724–735

Rasmussen MK, Mestre H, Nedergaard M (2022) Fluid transport in the brain. Physiol Rev 102: 1025–1151

Redmond SA, Figueres-Oñate M, Obernier K, Nascimento MA, Parraguez JI, López-Mascaraque L, Fuentealba LC, Alvarez-Buylla A (2019) Development of Ependymal and Postnatal Neural Stem Cells and Their Origin from a Common Embryonic Progenitor. Cell Rep 27: 429-441.e3

Robson JP, Wagner B, Glitzner E, Heppner FL, Steinkellner T, Khan D, Petritsch C, Pollak DD, Sitte HH, Sibilia M (2018) Impaired neural stem cell expansion and hypersensitivity to epileptic seizures in mice lacking the EGFR in the brain. FEBS J 285: 3175–3196

Rocamonde B, Herranz-Pérez V, Garcia-Verdugo JM, Huillard E (2021) ID4 Is Required for Normal Ependymal Cell Development. Front Neurosci 15: 668243

Romano R, Bucci C (2020) Role of EGFR in the Nervous System. Cells 9

Rosário M, Schuster S, Jüttner R, Parthasarathy S, Tarabykin V, Birchmeier W (2012) Neocortical dendritic complexity is controlled during development by NOMA-GAP-dependent inhibition of Cdc42 and activation of cofilin. Genes Dev 26: 1743–1757

Saarikangas J, Kourdougli N, Senju Y, Chazal G, Segerstråle M, Minkeviciene R, Kuurne J, Mattila PK, Garrett L, Hölter SM et al (2015) MIM-Induced Membrane Bending Promotes Dendritic Spine Initiation. Dev Cell 33: 644–659

Saarikangas J, Mattila PK, Varjosalo M, Bovellan M, Hakanen J, Calzada-Wack J, Tost M, Jennen L, Rathkolb B, Hans W et al (2011) Missing-in-metastasis MIM/MTSS1 promotes actin assembly at intercellular junctions and is required for integrity of kidney epithelia. J Cell Sci 124: 1245–1255

Saarikangas J, Zhao H, Pykäläinen A, Laurinmäki P, Mattila PK, Kinnunen PKJ, Butcher SJ, Lappalainen P (2009) Molecular mechanisms of membrane deformation by I-BAR domain proteins. Curr Biol 19: 95–107

Sarapulov AV, Petrov P, Hernández-Pérez S, Šuštar V, Kuokkanen E, Cords L, Samuel RVM, Vainio M, Fritzsche M, Carrasco YR et al (2020) Missing-in-Metastasis/Metastasis Suppressor 1 Regulates B Cell Receptor Signaling, B Cell Metabolic Potential, and T Cell-Independent Immune Responses. Front Immunol 11: 599

Sayers EW, Beck J, Bolton EE, Brister JR, Chan J, Comeau DC, Connor R, DiCuccio M, Farrell CM, Feldgarden M et al (2011) NCBI Gene Entry Plk4 polo like kinase 4 [Mus musculus (house mouse)]. https://www.ncbi.nlm.nih.gov/gene/20873. 10 April 2025

Sayers EW, Beck J, Bolton EE, Brister JR, Chan J, Comeau DC, Connor R, DiCuccio M, Farrell CM, Feldgarden M et al (2015) NCBI Gene Entry Plk1 polo like kinase 1 [Mus musculus (house mouse)]. https://www.ncbi.nlm.nih.gov/gene/18817. 10 April 2025

Sayers EW, Beck J, Bolton EE, Brister JR, Chan J, Comeau DC, Connor R, DiCuccio M, Farrell CM, Feldgarden M et al (2024) Database resources of the National Center for Biotechnology Information. Nucleic Acids Res 52: D33-D43

Sayers EW, Beck J, Bolton EE, Brister JR, Chan J, Comeau DC, Connor R, DiCuccio M, Farrell CM, Feldgarden M et al (2025a) NCBI Gene Entry MTSS I-BAR domain containing 1 [Homo sapiens (human)]. https://www.ncbi.nlm.nih.gov/gene/9788. 20 March 2025

Sayers EW, Beck J, Bolton EE, Brister JR, Chan J, Comeau DC, Connor R, DiCuccio M, Farrell CM, Feldgarden M et al (2025b) NCBI Gene Entry Mtss1 MTSS I-BAR domain containing 1 [Mus musculus (house mouse)]. https://www.ncbi.nlm.nih.gov/gene/211401. 20 March 2025

Sayers EW, Beck J, Bolton EE, Brister JR, Chan J, Comeau DC, Connor R, DiCuccio M, Farrell CM, Feldgarden M et al (2025c) NCBI Gene Entry NIMA (never in mitosis gene a)-related expressed kinase 2 [Mus musculus (house mouse)]. https://www.ncbi.nlm.nih.gov/gene/18005. 10 April 2025

Schindelin J, Arganda-Carreras I, Frise E, Kaynig V, Longair M, Pietzsch T, Preibisch S, Rueden C, Saalfeld S, Schmid B et al (2012) Fiji: an open-source platform for biological-image analysis. Nat Methods 9: 676–682

Schlautmann L (2025) Glucose-induced activation of Tas1R3 disrupts calcium signaling and macrophage functionality. Dissertation

Segalen M, Bellaïche Y (2009) Cell division orientation and planar cell polarity pathways. Semin Cell Dev Biol 20: 972–977

Ségalen M, Johnston CA, Martin CA, Dumortier JG, Prehoda KE, David NB, Doe CQ, Bellaïche Y (2010) The Fz-Dsh planar cell polarity pathway induces oriented cell division via Mud/NuMA in Drosophila and zebrafish. Dev Cell 19: 740–752

Sibilia M, Steinbach JP, Stingl L, Aguzzi A, Wagner EF (1998) A strain-independent postnatal neurodegeneration in mice lacking the EGF receptor. The EMBO Journal 1998: 719–731

Sistig T, Lang F, Wrobel S, Baader SL, Schilling K, Eiberger B (2017) Mtss1 promotes maturation and maintenance of cerebellar neurons via splice variant-specific effects. Brain Struct Funct 222: 2787–2805

Sjöstedt E, Zhong W, Fagerberg L, Karlsson M, Mitsios N, Adori C, Oksvold P, Edfors F, Limiszewska A, Hikmet F et al (2020) An atlas of the protein-coding genes in the human, pig, and mouse brain. Science 367, see https://www.proteinatlas.org/ENSG00000170873-MTSS1/single+cell

Spassky N, Merkle FT, Flames N, Tramontin AD, García-Verdugo JM, Alvarez-Buylla A (2005) Adult ependymal cells are postmitotic and are derived from radial glial cells during embryogenesis. J Neurosci 25: 10–18

Stamatiou K, Huguet F, Serapinas LV, Spanos C, Rappsilber J, Vagnarelli P (2024) Ki-67 is necessary during DNA replication for fork protection and genome stability. Genome Biol 25: 105

Stepien BK, Vaid S, Huttner WB (2021) Length of the Neurogenic Period-A Key Determinant for the Generation of Upper-Layer Neurons During Neocortex Development and Evolution. Front Cell Dev Biol 9: 676911

Stouffer MA, Golden JA, Francis F (2016) Neuronal migration disorders: Focus on the cytoskeleton and epilepsy. Neurobiol Dis 92: 18–45

Sun Y, Goderie SK, Temple S (2005) Asymmetric distribution of EGFR receptor during mitosis generates diverse CNS progenitor cells. Neuron 45: 873–886

Svitkina T (2018) The Actin Cytoskeleton and Actin-Based Motility. Cold Spring Harb Perspect Biol 10

Terry BK, Kim S (2022) The role of Hippo-YAP/TAZ signaling in brain development. Dev Dyn 251: 1644–1665

Tissir F, Goffinet AM (2013) Shaping the nervous system: role of the core planar cell polarity genes. Nat Rev Neurosci 14: 525–535

Tsai H-H, Niu J, Munji R, Davalos D, Chang J, Zhang H, Tien A-C, Kuo CJ, Chan JR, Daneman R et al (2016) Oligodendrocyte precursors migrate along vasculature in the developing nervous system. Science 351: 379–384

Uusküla-Reimand L, Hou H, Samavarchi-Tehrani P, Rudan MV, Liang M, Medina-Rivera A, Mohammed H, Schmidt D, Schwalie P, Young EJ et al (2016) Topoisomerase II beta interacts with cohesin and CTCF at topological domain borders. Genome Biol 17: 182

Vaid S, Huttner WB (2020) Transcriptional Regulators and Human-Specific/Primate-Specific Genes in Neocortical Neurogenesis. Int J Mol Sci 21

van der Spuy M, Wang JX, Kociszewska D, White MD (2023) The cellular dynamics of neural tube formation. Biochem Soc Trans 51: 343–352

Vilz TO, Moepps B, Engele J, Molly S, Littman DR, Schilling K (2005) The SDF-1/CXCR4 pathway and the development of the cerebellar system. Eur J Neurosci 22: 1831–1839

Wagner B, Natarajan A, Grünaug S, Kroismayr R, Wagner EF, Sibilia M (2006) Neuronal survival depends on EGFR signaling in cortical but not midbrain astrocytes. The EMBO Journal 2006: 752–762

Wang F, He Q, Yao NY, O'Donnell ME, Li H (2024) The human ATAD5 has evolved unique structural elements to function exclusively as a PCNA unloader. Nat Struct Mol Biol 31: 1680–1691

Wang Y, Nathans J (2007) Tissue/planar cell polarity in vertebrates: new insights and new questions. Development 134: 647–658

Wang Y, Zhou K, Zeng X, Lin J, Zhan X (2007) Tyrosine phosphorylation of missing in metastasis protein is implicated in platelet-derived growth factor-mediated cell shape changes. J Biol Chem 282: 7624–7631

Warton DI, Duursma RA, Falster DS, Taskinen S (2012) smatr 3– an R package for estimation and inference about allometric lines. Methods Ecol Evol 3: 257–259

Weickenmeier J, Rooij R de, Budday S, Steinmann P, Ovaert TC, Kuhl E (2016) Brain stiffness increases with myelin content. Acta Biomater 42: 265–272

Xia S, Li X, Johnson T, Seidel C, Wallace DP, Li R (2010) Polycystin-dependent fluid flow sensing targets histone deacetylase 5 to prevent the development of renal cysts. Development 137: 1075–1084

Xu L, Du H, Zhang Q, Wang C, Yan L, Tian G, Fu X (2019) BAI1-associated protein 2-like 2 is a potential biomarker in lung cancer. Oncol Rep 41: 1304–1312

Yaday VN, Zamler D, Baker GJ, Kadiyala P, Erdreich-Epstein, Anat, DeCarvalho, Ana C, Mikkelsen, Tom, Castro MG, Lowenstein PR (2016) CXCR4 increases in-vivo glioma perivascular invasion, and reduces radiation induced apoptosis: A genetic knockdown study. Oncotarget 2016

Yamagishi A, Masuda M, Ohki T, Onishi H, Mochizuki N (2004) A novel actin bundling/filopodium-forming domain conserved in insulin receptor tyrosine kinase substrate p53 and missing in metastasis protein. J Biol Chem 279: 14929–14936

Yamaguchi Y, Miura M (2013) How to form and close the brain: insight into the mechanism of cranial neural tube closure in mammals. Cell Mol Life Sci 70: 3171–3186

Yun K, Mantani A, Garel S, Rubenstein J, Israel MA (2004) Id4 regulates neural progenitor proliferation and differentiation in vivo. Development 131: 5441–5448

Zeleniak AE, Huang W, Fishel ML, Hill R (2018) PTEN-Dependent Stabilization of MTSS1 Inhibits Metastatic Phenotype in Pancreatic Ductal Adenocarcinoma. Neoplasia 20: 12–24

Zhan T, Cao C, Li L, Gu N, Civin CI, Zhan X (2016) MIM regulates the trafficking of bone marrow cells via modulating surface expression of CXCR4. Leukemia 30: 1327–1334

Zhang L, Li H, Zeng S, Chen L, Fang Z, Huang Q (2015) Long-term tracing of the BrdU label-retaining cells in adult rat brain. Neurosci Lett 591: 30–34

Zhang S, Qi Q (2015) MTSS1 suppresses cell migration and invasion by targeting CTTN in glioblastoma. J Neurooncol 121: 425–431

Zhang X, Mennicke CV, Xiao G, Beattie R, Haider MA, Hippenmeyer S, Ghashghaei HT (2020) Clonal Analysis of Gliogenesis in the Cerebral Cortex Reveals Stochastic Expansion of Glia and Cell Autonomous Responses to Egfr Dosage. Cells 9

Zhang X, Xiao G, Johnson C, Cai Y, Horowitz ZK, Mennicke C, Coffey R, Haider M, Threadgill D, Eliscu R et al (2023) Bulk and mosaic deletions of Egfr reveal regionally defined gliogenesis in the developing mouse forebrain. iScience 26: 106242

Zhao H, Pykäläinen A, Lappalainen P (2011) I-BAR domain proteins: linking actin and plasma membrane dynamics. Current Opinion in Cell Biology 23: 14–21

Zhong J, Shaik S, Wan L, Tron AE, Wang Z, Sun L, Inuzuka H, Wei Wenyi (2013) SCFβ-TRCP targets MTSS1 for ubiquitination-mediated destruction to regulate cancer cell proliferation and migration. Oncotarget: pp. 2339–2353

7 List of Figures

Figure 1: Cranial Neurulation....6

Figure 2: Brain Vesicles In Development....7

Figure 3: Differentiation of Neural Progenitors to Mature Neocortical Projection Neurons....10

Figure 4: Effects of PCP-Related Mutations....19

Figure 5: Protrusion-Related Mechanisms of Mtss1....24

F*igure 6: Protein Domains of Mtss1 and Their Functions*....26

Figure 7: Dissection Procedure to Yield Lateral Ventricle Wholemounts and Samples for qPCRs....42

Figure 8: Example Classification of Two Cells Facing Each Other....48

Figure 9: Evaluating Morphology of Caudal Telencephalon....50

Figure 10: Distance from Ependyma to Meninges and Measured Force upon Indentation of Caudal Telencephalon of Adult Mice....55

Figure 11: Number of Cells and DNA Content of Caudal Telencephalon Samples of Adult Mice....56

Figure 12: Gene Expression over Development, Arranged by Target Function....60

Figure 13: RNA Expression of Progenitor Cell and Glia Markers in Perinatal Development....63

Figure 14: RNA Expression of Genes in Neuronal Differentiation in Perinatal Development....64

Figure 15: RNA Expression of Proliferation Markers in Perinatal Development....65

Figure 16: RNA Expression of Apoptosis Markers in Perinatal Development....66

Figure 17: Gene Expression of Glia- and Neuron-Specific Markers in P7 Mice....67

Figure 18: Gene Expression of Apoptosis- Proliferation-Specific Markers in P7 Mice....68

List of Figures

Figure 19: Gene Expression of Progenitor-, Glia- and Neuron-Specific Markers in Adult Mice.....69

Figure 20: RNA Expression of Proliferation and Apoptosis Markers in Adult Mice.....70

Figure 21: RNA Expression of Egfr.....71

Figure 22: Relative Number of Ki67+ Cells in VZ and SVZ.....73

Figure 23: Summary Profile Plots of DAPI, Pax6, Sox2 and Tbr2 in the Ventricle Roof Germinal Zones at P0 by Genotype.....75

Figure 24: Distribution of Progenitor Cells in the Ventricle Roof Germinal Zones at P0.....76

Figure 25: Number of B1 Cells per Field.....78

Figure 26: Rotational Polarity of Individual Cilia on E1 Ependymal Cells.....80

Figure 27: Translational Polarity of E1 Ependymal Cells.....82

Figure 28: Count of Basal Body Patches Facing Each Other.....83

Figure 29: Example Indentation.....117

Figure 30: Example Map of Angular Data to Evaluate Translational Polarity.....118

8 List of Tables

Table 1: Table of General Materials Used....29
Table 2: Antibodies Used....32
Table 3: Primers Used for RT-qPCR with Respective Catalogoue Number at Thermo Fisher Scientific 33
Table 4: Contents of Digestion Solution for DNA Isolation per Sample....34
Table 5: Contents of PCR Reaction Mix per Sample....35
Table 6: PCR Program used in Genotyping of Mtss1 Mice....35
Table 7: Primer Sequences used in Genotyping of Mtss1 Mice....35
Table 8: Contents Tris-Borate-EDTA Buffer for Gel Electrophoresis....36
Table 9: Components of Reverse Transcription Reaction Mix....37
Table 10: Program used for Reverse Transcription....37
Table 11: Components of RT-qPCR Reaction Mix....38
Table 12: PCR Program used in RT-qPCR....38
Table 13: Components of Fixation Solution....40
Table 14: Components of BRB80 Buffer....43
Table 15: Components of Tris-EDTA Buffer for Immunofluorescence....43
Table 16: Components of Citrate Buffer for Immunofluorescence....44
Table 17: Components of β-gal Base Solution....45
Table 18: Components of β-gal Wash Solution....45
Table 19: Components of β-gal Staining Solution....45
Table 20: R Packages Employed for Data Evaluation....53
Table 21: Marker Genes Measured in RT-qPCRs and their Roles....58
Table 22: Overview of Cell Markers and their Expression in Mtss1 KO, based on mRNA Expression and Profile Plots of Immunofluorescence Stainings....89

9 Appendix

9.1 Example Indentation Graph

Figure 29 shows an example measurement recorded during indentation experiments that are described in sections 3.7.1 and 4.1.1.

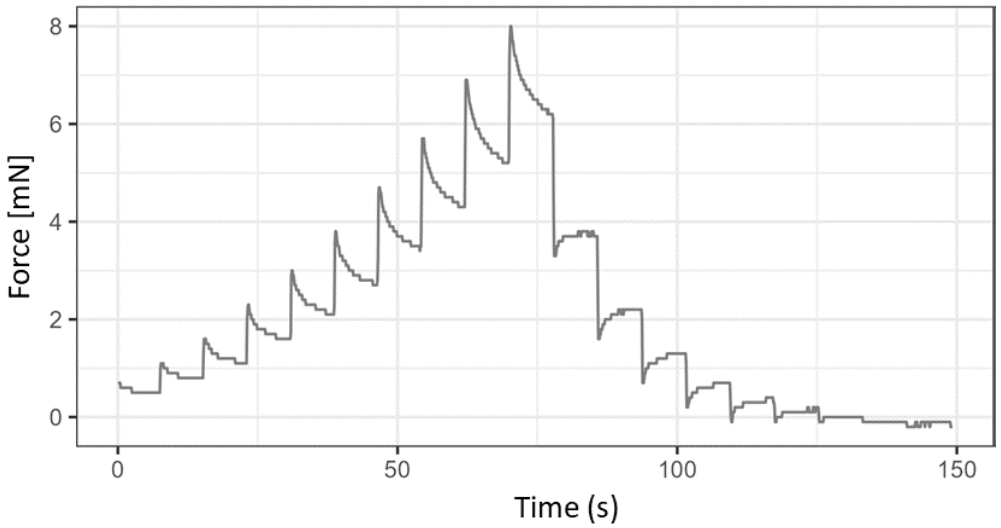

Figure 29: Example Indentation

Measured force is plotted against time. The probe was lowered at a velocity of 0.2mm/s, indenting the tissue. The continuous force acting on the probe was measured at an interval of 0.1s. Indenting the tissue consisted of 10 steps of 30µm. This plot starts at the maximum value measured after the first indentation (30µm). The force measured at maximum indentation (300µm) is 8mN.

9.2 Example Set of Angular Data for Evaluation of Translational Polarity

Figure 30 shows an example map of angles measured for one image as part of the evaluation of translational polarity as described in sections *3.6.3 and 4.5.2.*

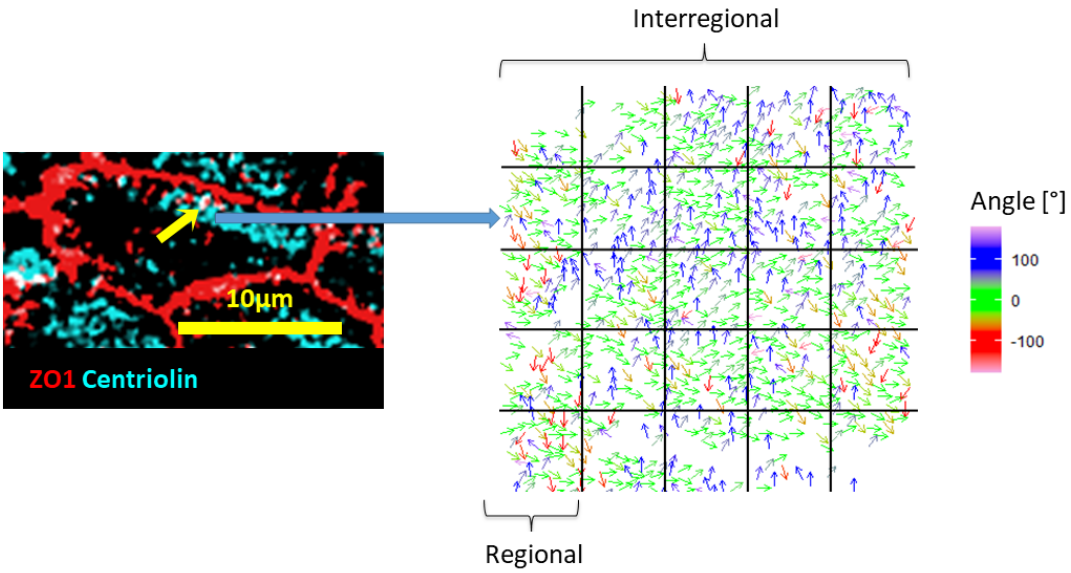

Figure 30: Example Map of Angular Data to Evaluate Translational Polarity

Images of size 439µm x 439µm were subdivided into 25 even fields. Coordinates of cell centre and basal body patch were collected per cell, and the angle of the line between the points relative to a reference recorded. The mean angle of all cells in one image was later defined as 0°. Angular variance was determined as outlined in sections 3.6.3 and 4.5.2. Regional angular variance was the variance between all angles of one of 25 fields. Interregional variance was the variance between the mean angles of each of the 25 fields.

9.3 R-Scripts

R Scripts used in this project are made available digitally.